

**INFRARED LASER SPECTROSCOPY OF MOLECULES IN HELIUM  
NANODROPLETS**

**Thesis submitted for the degree of  
Doctor of Philosophy  
at the University of Leicester**

**by**

**Media Ismael Sulaiman MSc  
Department of Chemistry  
University of Leicester**

**2017**

# Infrared Laser Spectroscopy of Molecules in Helium Nanodroplets

*Media Ismael Sulaiman*

## Abstract

This project is centred upon the probing of the structures of molecular clusters in helium nanodroplets (HeDs) via infrared laser spectroscopy. Absorption of IR radiation by clusters inside HeDs causes helium to evaporate from the droplet, resulting in a lower ionisation cross section for the droplet and a consequent depletion of ion signals due to the absorbing clusters in mass spectra. This mass selectivity was used to assist with the assignment of specific IR bands to specific sizes of clusters. With this approach the first attempt to record IR spectra of the cyclic isomers of the water heptamer and octamer is reported. This work has been supported by *ab initio* calculations and evidence is presented for successful observation of these cyclic clusters. In addition, IR spectra of larger water clusters  $(\text{H}_2\text{O})_n$ , where  $11 \leq n \leq 21$ , were recorded. We found that the large water clusters are derived from 3-coordinated and 2-coordinated water monomers.

IR spectra of methanol clusters have been recorded for the first time in the OH stretching region. We find that clusters such  $(\text{CH}_3\text{OH})_4$  and  $(\text{CH}_3\text{OH})_5$  are consistent with fully cyclic structures held together by hydrogen bonds. This conclusion is very different from earlier work in HeDs, which reported non-cyclic structure for the tetramer and pentamer. When water molecules were combined with methanol in HeDs IR spectra of clusters such as  $(\text{CH}_3\text{OH})_2\text{H}_2\text{O}$  and  $(\text{CH}_3\text{OH})_3\text{H}_2\text{O}$  clusters were observed for the first time. As with pure water and pure methanol clusters, the structures of these mixed clusters are consistent with cyclic structures.

Finally, a short study of the IR spectroscopy of the  $\text{I}_2(\text{H}_2\text{O})$  cluster is reported as part of a larger study which attempted to generate I atoms by thermal dissociation of  $\text{I}_2$  molecules prior to pickup by HeDs.

## **Acknowledgements**

First and foremost I would like to express my gratitude to my supervisor Prof. Andrew Ellis, who provided me with the opportunity to pursue my interest in laser spectroscopy, and for all of the guidance and advice that he has given in my project and the writing up of this thesis. I greatly appreciate his time and patience. The laser spectroscopy group has also played a very important role through useful discussions and assistance with the experimental apparatus. I am particularly grateful for Dr Shengfu Yang, Dr Gautam Sarma, Dr Ahmed Sadoon, Dr Stephanie Allpress, Dr Julia Davies and Andrew Shirley for their help and support. I am also thankful to all remaining members of the Physical Chemistry group.

I express gratitude to all the technical staff in the University of Leicester Chemistry Department, in particular, Carl Schieferstein and Praful Chauhan for their role in the construction and maintenance of some components of the experiment.

I wish to express my gratitude to my parents, brothers and sisters, to whom I want to dedicate this thesis. Their unwavering support and encouragement is so important to me. I am thankful to my beloved husband Zardasht for his kindness and continued support for everything. We have been together all the way through our PhD journey with hope for a bright future. I would especially like to express my love and thanks to my beloved daughters Dina and Diya for being good girls and always cheering me up. I

Finally, I would like to thank the Ministry of Higher Education and Scientific Research in the Kurdistan Region-Iraq for giving me the scholarship for this research project. Thanks also go to the Department of Physics, School of Science Education, University of Sulaimani, for agreeing that I can study for a PhD.

# Table of Contents

<b>Abstract</b> .....	<b>i</b>
<b>Acknowledgements</b> .....	<b>ii</b>
<b>Table of Contents</b> .....	<b>iii</b>
<b>List of Tables</b> .....	<b>vi</b>
<b>List of Figures</b> .....	<b>vii</b>
<b>Chapter 1: Introduction</b> .....	<b>1</b>
1.1 Properties of helium.....	1
1.2 Properties of superfluid helium.....	2
1.3 He droplet formation.....	6
1.4 Helium droplet size.....	7
1.5 Dopant pick up.....	9
1.6 The location of the dopants.....	11
1.7 Ionization processes in helium Droplets.....	12
1.8 Spectroscopy in helium droplets.....	13
1.9 The structure of this thesis.....	14
<b>Chapter 2: Experimental Apparatus</b> .....	<b>15</b>
2.1 Overall system summary.....	15
2.2 Main experimental equipment.....	19
2.2.1 Quadrupole Mass Spectrometer.....	19
2.2.2 Laser System for Depletion Spectroscopy.....	21
2.2.2.1 Nd: YAG laser.....	21
2.2.2.2 Optical parametric oscillator/amplifier (OPO/A).....	22
2.2.3 Depletion spectroscopy.....	25
<b>Chapter 3: Infrared spectroscopy of pure water clusters in HeDs</b> .....	<b>27</b>
3.1 Introduction.....	27
3.2 Experimental.....	30
3.3 Computational details.....	30

3.4 Results and Discussion.....	31
3.4.1 <i>Ab initio</i> calculations of cyclic water clusters.....	31
3.4.2 Mass Spectrum.....	36
3.4.3 IR Spectroscopy of small water clusters (H <sub>2</sub> O) <sub>n</sub> (n = 2-6).....	37
3.4.4 Infrared Spectroscopy of Water Clusters (H <sub>2</sub> O) <sub>n</sub> (n = 7-9).....	38
3.5 Conclusions.....	47
<b>Chapter 4: Larger water clusters (H<sub>2</sub>O)<sub>n</sub> (n = 10 – 21).....</b>	<b>48</b>
4.1 Introduction.....	48
4.2 Experimental details.....	50
4.3 Results and discussion.....	51
4.3.1 Infra-red spectroscopy of (H <sub>2</sub> O) <sub>n</sub> (n = 10 – 21).....	51
4.3.2 Hydrogen-bonded OH region.....	53
4.3.3 Free OH region.....	54
4.4 Comparison between IR spectra of large water clusters, liquid water and ice.....	57
4.5 Conclusions .....	61
<b>Chapter 5: Infrared Spectroscopy of Pure Methanol.....</b>	<b>62</b>
5.1 Introduction.....	62
5.2 Experimental.....	64
5.3 Computational details.....	66
5.4 Results and discussion.....	67
5.5 Conclusions.....	73
<b>Chapter 6: mixture of methanol and water.....</b>	<b>74</b>
6.1 Introduction.....	74
6.2 Experimental details.....	76
6.3 Computational Details.....	77
6.4 Results and discussion.....	77
6.5 Conclusion .....	81
<b>Chapter 7: IR spectroscopy of Iodine-Water complexes in helium nanodroplets.....</b>	<b>82</b>
7.1 Introduction.....	82
7.2 Experimental details .....	83

7.3 Computational details.....	87
7.4 Results and discussion.....	88
7.4.1 Thermal dissociation of I <sub>2</sub> .....	88
7.4.2 I <sub>2</sub> + H <sub>2</sub> O complexes.....	93
7.4.2.1 Mass spectra .....	93
7.4.2.2 Infrared spectra of water/iodine.....	96
7.5 Conclusions.....	99
<b>Chapter 8:.....</b>	<b>101</b>
8.1	Thesis
Summary.....	101
8.2 Future Work .....	102
<b>Bibliography .....</b>	<b>105</b>

## List of Tables

<b>Table 1.1</b>	Range of changing the phase of the He fluid from He I to He II with temperature [15].....	5
<b>Table 3.1</b>	Experimental and calculated vibrational data for water clusters in the OH stretching region.....	29

## List of Figures

<b>Figure 1.1</b>	$^4\text{He}$ phase diagram reprinted from reference [9].....	2
<b>Figure 1.2</b>	Behaviour of fractional density of the two components of the He fluid [16]. Reprinted from reference [16]. $n_o$ and $n_n$ are the superfluid and the normal fluid number density, respectively, and $n$ is the total of $n_o$ and $n_n$ .....	5
<b>Figure 1.3</b>	Helium droplet size as a function of temperature from experimental measurements. The figure is taken from reference [9]. The squares and circles data were extracted from a combination of titration [9] and the stars are from deflection [26,30] techniques.....	9
<b>Figure 1.4</b>	Poisson distributions showing the probability of picking up $k$ dopant particles as a function of the partial pressure of the dopants.....	10
<b>Figure 2.1</b>	Diagram showing the main parts of the experimental system; low temperature nozzle, a skimmer, pick up cells, a quadrupole mass spectrometer and the laser source [12].....	15
<b>Figure 2.2</b>	Schematic diagram of the nozzle shows its position [69].....	16
<b>Figure 2.3</b>	Schematic of the nozzle and the first skimmer [69].....	17
<b>Figure 2.4</b>	Schematic of the pickup cell with dimensions [69].....	18
<b>Figure 2.5</b>	Quadrupole mass spectrometer region of helium droplet apparatus [69].....	19
<b>Figure 2.6</b>	Mass spectrum of the background of the vacuum system with the nozzle at 16 K, a helium stagnation pressure of 33 bar and QMS ionization energy of 90V.....	21
<b>Figure 2.7</b>	Configuration of the OPO/A laser system. M1, M2, M3 are turning mirrors. SHG = second harmonic generation. WP = wave plate. X1 and X2 are a totally reflecting mirrors and an output coupler, respectively.....	23
<b>Figure 2.8</b>	Ion signal as a function of time when the IR radiation is resonant with a dopant transition. The red peak shows a decline in the ion intensity because of shrinkage in the helium droplet size on IR absorption, which reduces the HeD ionization cross section. The width of the depletion is roughly equal to the droplet transit time from the pickup cell to the QMS.....	26
<b>Figure 3.1</b>	Cyclic water structures ( $(\text{H}_2\text{O})_{3-8}$ ) calculated by MP2 calculation.....	32

<b>Figure 3.2</b>	Calculated (MP2/aug-cc-pVDZ) water heptamer structures. (a) Prism, (b) chair, (c) bicyclic structure and (d) fully cyclic isomers. Also shown are IR spectra predicted from a harmonic oscillator model.....	33
<b>Figure 3.3</b>	Calculated IR spectra (harmonic approximation) of the cyclic water clusters $(\text{H}_2\text{O})_n$ ( $n= 3-8$ ) using the MP2 level of theory, and scaling factor was not used in this calculations.....	34
<b>Figure 3.4</b>	Calculation of the IR spectra of cyclic water clusters using an anharmonic model.....	35
<b>Figure 3.5</b>	Mass spectrum for water clusters in HeDs recorded at a nozzle temperature of 16 K and helium pressure of 33 bar.....	37
<b>Figure 3.6</b>	IR spectrum recorded by monitoring ion depletion at $m/z$ 19.....	38
<b>Figure 3.7</b>	IR spectra of water clusters recorded in mass channels of 91, 109, 127 and 145 $m/z$ from the bottom to the top. The dashed lines show positions of the bonded OH stretch maxima for each $m/z$ , except the same colour is used for $m/z$ 91 and 127 because their maxima are at almost identical positions. The sharp peak at 3717 $\text{cm}^{-1}$ (present in all the spectra above) is the free OH stretching band from various water clusters.....	40
<b>Figure 3.8</b>	Experimental spectrum of water clusters with $n \geq 7$ (previously shown as second bottom spectrum in Fig 3.7). The red lines are predictions from ab initio calculations for the fully cyclic heptamer isomer, however the theoretical frequencies of the current figure are scaled using scaling factors of 0.955 for the free OH stretch and 0.972 for the OH hydrogen-bonded stretches. The observed spectra (and all other observed spectra in the current work) are not normalized to any variation of the laser intensity since the pulse energy only varied from 8 mJ to 12 mJ in all experiments of the current work.....	42
<b>Figure 3.9</b>	IR spectrum recorded at $m/z = 127$ ( $(\text{H}_2\text{O})_7\text{H}^+$ ) (same as showed in second spectrum from the top). The nozzle temperature was 16 K, the helium pressure was 33 bar and the water vapour pressure in the pickup cell was $5.15 \times 10^{-6}$ mbar. Also shown is the MP2/ aug-cc-pVDZ harmonic prediction (in red), which is showed also in Figure 3.3 but before adding scal factor. The calculated vibrational frequencies were scaled using scaling factors of 0.955 for the free OH stretch and 0.972 for the OH hydrogen-bonded stretches .....	44
<b>Figure 3.10</b>	Theoretical (blue) and experimental IR spectra of the cubic water octamer in the gas phase (red colour). Reprinted from reference [102].....	45
<b>Figure 3.11</b>	Comparison of the experimental and theoretical (MP2/aug-cc-pVDZ; scaled harmonic approximation) positions of the bonded OH stretching bands of cyclic water clusters from $(\text{H}_2\text{O})_3$ to $(\text{H}_2\text{O})_8$ .....	46

<b>Figure 4.1</b>	Mass spectrum obtained from water clusters in helium droplets in the range $m/z$ 8 – 400.....	51
<b>Figure 4.2</b>	IR spectrum of large water clusters $(H_2O)_n$ . This was recorded by monitoring $(H_2O)_N H^+$ ions, and hence must come from neutral $(H_2O)_n$ clusters with $n \geq N + 1$ . The blue line is a guide to the eye and shows the estimated maximum of the strongest bonded OH feature.....	52
<b>Figure 4.3</b>	Calculated structures of $(H_2O)_8$ cluster taken from reference [142]. (a) Ring structure, all water molecules are involved in DDA binding. (b) ‘Cubic’ octamer in which water molecules with dangling OH bands are involved in AAD binding (molecules 1, 3, 5 and 7) while the others have DDA binding.....	55
<b>Figure 4.4</b>	Free OH stretching region, <b>a</b> is recorded by detecting $H^+(H_2O)_9$ ions. This spectrum was obtained at a water pressure higher than that used to record the spectrum in Figure 4.2. - <b>b</b> Free OH spectra of larger water clusters the free-OH stretch at $3719\text{ cm}^{-1}$ is the dominant feature in IR spectra up to (at least) $n = 17$ , showing that clusters up to $n = 17$ also have many unbound OH bonds.....	57
<b>Figure 4.5</b>	Size-selective IR spectra of $(H_2O)_n$ ( $n = 85 - 475$ ), reprinted from reference [127].....	58
<b>Figure 4.6</b>	(a) Infrared spectra of large water clusters (this work). (b) Infrared spectra of liquid water at 298K, supercooled water at 240 K and water ice at 235 K (reprinted from reference [128]).....	60
<b>Figure 5.1</b>	Mass spectrum of methanol clusters in a range from $m/z = 8$ to 170.....	65
<b>Figure 5.2</b>	Experimental IR spectra of methanol clusters recorded using depletion spectroscopy. The lowest trace ((a), black colour) was recorded by detecting ions at $m/z$ 33. The blue spectrum (b) was recorded by detecting at $m/z$ 97. The red spectrum (c) was also obtained for $m/z$ 97 but at a higher methanol pressure than spectrum (b).....	69
<b>Figure 5.3</b>	Optimised cyclic structures of $(CH_3OH)_3$ , $(CH_3OH)_4$ and $(CH_3OH)_4$ at MP2/aug-pVDZ.....	70
<b>Figure 5.4</b>	Optimum structures of methanol clusters, cluster 3+1 predicted at MP2/aug-cc-pVDZ while structure 3+2 performed at DFT-B3LYP/ aug-cc-pVD.....	70
<b>Figure 5.5</b>	Observed infrared spectrum for $m/z = 33$ (pure methanol), higher trace. The lower trace show the OH stretching bands predicted from ab initio calculations for different methanol structures.....	71

<b>Figure 5.6</b>	Higher trace is the experimental spectrum at $m/z$ of 97 which includes peaks of tetramer and pentamer methanol. The lower trace is the predicted OH stretching of 5+0 and 3+2 pentamer methanol structures.....	72
<b>Figure 6.1</b>	Methanol-water dimer structures. In MW methanol is a proton donor and in the WM water is the proton donor [189].....	75
<b>Figure 6.2</b>	Mass spectrum in the range from 4 to 170 of a mixture methanol and water at vapour methanol/H <sub>2</sub> O of 31: 1. The mass spectrum shows clear signals of methanol clusters attached to single water molecule.....	76
<b>Figure 6.3</b>	Optimum structures of (CH <sub>3</sub> OH) <sub>2</sub> H <sub>2</sub> O and (CH <sub>3</sub> OH) <sub>3</sub> H <sub>2</sub> O are calculated via double harmonic calculations at MP2/aug-cc-pVDZ.....	77
<b>Figure 6.4</b>	IR spectra of different mixture of water/methanol in the range 3455 – 3750 cm <sup>-1</sup> .....	78
<b>Figure 6.5</b>	IR spectra of mixture methanol and water in range 3100 - 3850 cm <sup>-1</sup> for two different mass channels at $m/z$ of 33 and 51. Lower trace includes theoretical calculations for cyclic (CH <sub>3</sub> OH) <sub>2</sub> H <sub>2</sub> O (red lines) and (CH <sub>3</sub> OH) <sub>3</sub> H <sub>2</sub> O (blue lines) clusters. Experimental spectra are shown in upper traces. Red arrows refer to attached methanol clusters and monomer water that described in the text.....	80
<b>Figure 7.1</b>	Overall setup of the old helium droplet system [69] used for initial pyrolysis experiments.....	85
<b>Figure 7.2</b>	(a) Simplified illustration of the iodine pyrolysis source. (b) Photograph of the actual arrangement.....	86
<b>Figure 7.3</b>	Mass spectrum obtained for pickup of I <sub>2</sub> in helium droplets at room temperature (black line) and at a temperature of 1190 K (red line). The blue line refers to the helium atoms attached to I <sup>+</sup> while the other iodine ions are not attached to the He atoms.....	90
<b>Figure 7.4</b>	Plot of the I <sup>+</sup> /I <sub>2</sub> <sup>+</sup> signal ratio as a function of temperature.....	91
<b>Figure 7.5</b>	I <sub>2</sub> <sup>+</sup> signal versus temperature.....	92
<b>Figure 7.6</b>	I <sup>+</sup> signal as a function of temperature.....	93
<b>Figure 7.7</b>	Mass spectrum from iodine clusters in helium droplets formed at a helium stagnation pressure and temperature of 32 bar and 15 K, respectively.....	94
<b>Figure 7.8</b>	Mass spectrum of HeDs doped with both water and iodine molecules.....	95
<b>Figure 7.9</b>	Mass spectrum recorded for higher dopant pressures than the spectrum shown in Figure 7.8. ....	96

**Figure 7.10** Depletion IR spectra recorded at  $m/z$  19 ( $\text{H}_2\text{OH}^+$ ) (black curve) when the HeDs were doped with only pure water, and IR spectrum at  $m/z$  272 ( $(\text{H}_2\text{O})\text{I}_2^+$ ) (blue curve) when HeDs are doped with both water molecules and iodine. In the stick diagram at the bottom are scaled harmonic predictions for the water monomer (black line), the water dimer (red line), structure 1 of  $\text{I}_2(\text{H}_2\text{O})$  (blue line), structure 2 of  $\text{I}_2(\text{H}_2\text{O})$  (purple line) and  $(\text{H}_2\text{O})_2\text{I}_2$  (green line).....98

**Figure 7.11**  $(\text{H}_2\text{O})\text{I}_2$  isomers. (a) In structure 1 both water and iodine molecules are planar while (b) in structure 2 both  $\text{H}_2\text{O}$  and  $\text{I}_2$  are non-planar.....99

# Chapter 1

## *Introduction*

### 1.1 Properties of helium

Helium was first discovered spectroscopically in 1868 in the sun during a solar eclipse. It was later observed on earth by Pierre Janssen and Joseph Lockyer [1]. Helium has two isotopes,  $^3\text{He}$  and  $^4\text{He}$ , with  $^4\text{He}$  having by far the higher abundance (99.9998%). Helium will only liquefy at very low temperatures on account of the very weak binding between helium atoms. This is a consequence of the closed  $1s^2$  electronic configuration and its small atomic radius, where the latter delivers a small polarizability. In fact, at atmospheric pressure helium does not solidify, even at a temperature of absolute zero. This occurs because of the combination of the weak He-He binding with the small atomic mass, where the latter delivers a zero point energy comparable to the He-He binding energy [2-7].

The low temperature needed for liquefied  $^4\text{He}$  and the light masses of the atoms combine to generate relatively long *de Broglie* wavelengths for the individual atoms. The thermal *de Broglie* wavelength is given by [8]:

$$\lambda_{db} = \sqrt{\frac{2\pi \hbar^2}{m T k_B}} \quad (1-1)$$

Here  $m$  is the atomic mass,  $\hbar$  is *Planck's* constant divided by  $2\pi$ ,  $T$  is the absolute temperature, and  $k_B$  is the Boltzmann constant. At a temperature of 4 K for  $^4\text{He}$ ,  $\lambda_{db}$  will be about 0.7 nm. This exceeds the average spacing (0.27 nm) between He-He atoms in the liquid. Consequently, the low temperature of liquid  $^4\text{He}$  delocalizes the locations of helium atoms and changes its characteristics, creating a so-called *quantum liquid*.

The phase diagram of  $^4\text{He}$  is shown in Figure 1.1. A remarkable feature is the absence of a triple point [9]. At stagnation pressures below 25 bar,  $^4\text{He}$  changes from a normal viscous liquid (He I) to a superfluid (He II) at temperatures below 2.18 K. This temperature is called the *Lambda* point [3,10]. The boiling point of  $^4\text{He}$  is 4.21 K at atmospheric pressure and its critical point is at 5.2 K.

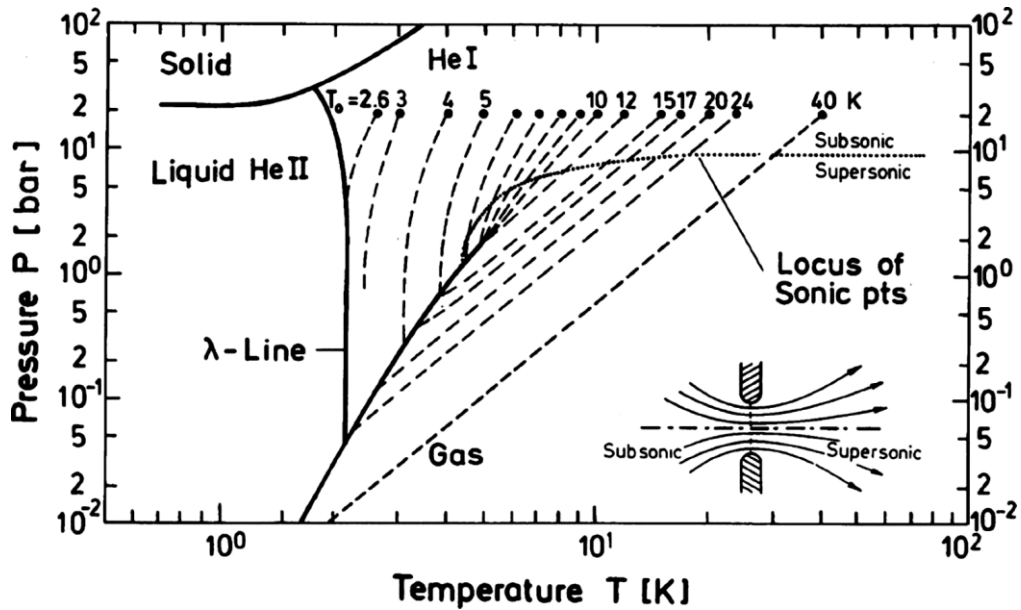


Figure 1.1.  $^4\text{He}$  phase diagram reprinted from reference [9].

The second He isotope,  $^3\text{He}$ , is a fermion on account of its half integer nuclear spin. A lower temperature (0.003 K) than  $^4\text{He}$  is required for  $^3\text{He}$  to become a superfluid because of the need for pairing of two fermions to generate a quasi-boson.

## 1.2 Properties of superfluid helium

Liquid helium was first observed as nanodroplets in the form of a fog in 1908 by Heike Kamerlingh Onnes [11]. The droplet was formed by cooling helium to 1.5 K and expanded via free expansion. During the end of 1920s and the early 1930s, unexpected properties of liquid helium were observed. The bubble-free boiling of helium below

the lambda temperature was first observed in 1932 [12] and confirmed in subsequent experiments by Keesom and Keesom [13]. They found that the thermal conductivity was abnormally large in He II and therefore the extremely high thermal conductivity of the superfluid phase prevents bubble formation in localised hot-spots [13]. This means that evaporation takes place uniformly at the surface of the liquid without any bubble formation [13]. Keesom and Keesom were the first to show that there are two phases of liquid helium and identified the lambda point at 2.2 K [13].

However, it was not until 1938 when two separate investigations showed that helium II is a superfluid. One of the studies, by Allen and Misener [14], showed that helium exhibited non-classical behaviour at temperatures lower than  $T_\lambda$ . The second study was by Kapitza [15], who coined the term *superfluidity*. Both studies explained the large conductivity of He II found in the work by Keesom and Keesom [13]. The high conductivity was explained as a sharp decline in the viscosity of liquid helium below 2.2 K. Moreover, solidification of helium was observed in 1939 by Keesom and Taconis at low temperature (2 K) and a large external pressure ( $> 25$  bar) [4].

$^4\text{He}$  atoms are classified as bosons as a result of their zero nuclear spin (two protons and two neutrons). A collection of helium atoms therefore satisfies Bose-Einstein statistics. In Bose-Einstein statistics the distribution probability for indistinguishable (non-interacting) particles occupying any single state with energy  $\epsilon$  at equilibrium is given by [8]:

$$f(\epsilon) = \frac{1}{e^{\beta(\epsilon-\mu)} - 1} \quad (1-2)$$

Here  $\beta = 1/k_B T$ ,  $T$  is the absolute system temperature and  $\mu$  is the chemical potential of the system. One consequence of being a bosonic fluid is that all of the helium atoms can occupy the same (lowest) quantum state at very low temperatures [13], which is in marked contrast to a collection of fermions (particles with half-integer spins).

An ideal gas satisfying Bose-Einstein statistics undergoes a transition at the critical temperature ( $T_c$ ) to a Bose-Einstein condensate (BEC) [8]. In 1938 London suggested BEC formation as a way to explain the superfluidity of  $^4\text{He}$  [11]. London considered  $^4\text{He}$  as a boson gas collapsed into the lowest macroscopic quantum state and used this to explain how this fluid might have zero viscosity [10]. At a temperature above  $T_c$  the helium behaves as a normal fluid, but below  $T_c$  it begins to behave as a BEC. London concluded that the Bose-Einstein condensate temperature is given by [10]:

$$T_c = \frac{h^2}{2\pi k_B m} \left( \frac{n}{2.612V} \right)^{2/3} \quad (1-3)$$

In the above equation  $n$  is the particle number density occupying volume  $V$ , and  $n$  can be found by combining the helium atomic mass ( $m$ ) with the density of the liquid. London obtained a value for  $T_c$  of 3.31 K, which is encouragingly close to the  $T_\lambda$  value of 2.2 K given the approximations and assumptions involved in deriving equation (1-3).

In an attempt to provide a description of the superfluid behaviour of He II, Tisza proposed the two-fluid theory of liquid helium in 1947 [16]. In this theory superfluid helium is viewed as a mixture of two fluids with different densities and velocities. One of the fluids is the normal fluid, with standard liquid properties. The other component is the superfluid fraction. The ratio of the amount of normal fluid to the total fluid,  $n_n/n$ , decreases until all of the liquid become superfluid (100%) at a temperature of absolute zero, as indicated in Table 1-1 and Figure 1.2. The superfluid component has no viscosity and no entropy: it is the normal component that carries these quantities and which transfers heat.

**Table 1.1** Range of changing the phase of the He fluid from He I to He II with temperature [16].

$n_n/n$	Temperature	He fluid
= 1	$T \geq T_c$	He I
= 0	$T = 0$	He II
< 1	$0 < T < T_c$	He II

In 1949, Andronikashvili experimentally established evidence for the two fluid model, which yielded the data shown in Figure 1.2 [17]. In this experiment, the normal fluid fraction was measured by recording the velocity of rotating compact disks suspended in helium [17]. The rotational frequency showed a rapid increase below  $T_\lambda$ , matching the known decrease in viscosity as the superfluid phase forms. The Andronikashvili experiment is consistent with the two-fluid model and provides a means of determining the normal/superfluid ratio.

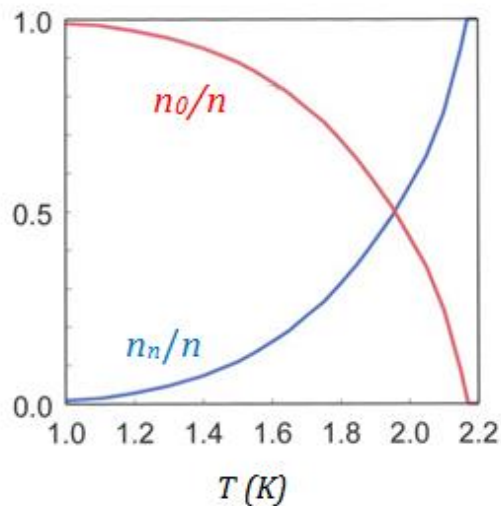


**Figure 1.2.** Behaviour of fractional density of the two components of the He fluid [16]. Reprinted from reference [16].  $n_o$  and  $n_n$  are the superfluid and the normal fluid number density, respectively, and  $n$  is the total of  $n_o$  and  $n_n$ .

A more detailed model of superfluid helium was provided by Landau, initially in 1941 [18] and with some improvements in 1947 [19]. Landau considered superfluid helium in terms of its internal excitation states, specifically phonons (sound quanta) and rotons (elementary vortex motion). Landau concluded that in order to excite He II, there is a critical minimum velocity that needs to be exceeded by the liquid. His theoretical results showed that velocity of rotons was 59 m/s while for phonons it is equal to the speed of sound. It is therefore excitation of rotons that dictates the critical velocity and Landau arrived at a value of 59 m s<sup>-1</sup>. The excitations of the fluid give rise to the viscosity so objects moving through the fluid at velocities below the Landau critical velocity should experience no drag. Experimental work of Alum *et al.* in 1977 [20] confirmed the critical velocity of Landau [18]. Note that in the two-fluid model the normal fluid fraction can be explained as that fraction of the fluid that has helium undergoing collective excitations.

### 1.3 He droplet formation

Helium nanodroplets are, as the name implies, nanoscale droplets of liquid helium. As detailed below, they have a steady-state temperature of 0.37 K and so fall into the regime where superfluid properties are expected to be important.

The basic idea behind the operation of most helium droplet sources is the supersonic gas expansion. In this technique, cooled and pressurised helium gas is expanded through a small pinhole into a high vacuum region [21]. As the gas expands cooling takes place and can lead to partial condensation. In the case of helium, because of the very weak He-He binding energy, pre-cooling of the gas to low temperature prior to expansion is essential to form helium clusters and droplets.

In the first successful attempt to make helium clusters by Becker *et al.* in 1961, helium at 0.98 mbar was expanded through a 0.15 mm diameter nozzle cooled to 4.2 K [22]. They detected helium clusters via measuring condensed helium on a collimator screen cooled with liquid nitrogen and they used time-of-flight methodology to determine the cluster velocities. A very narrow signal velocity distribution was

observed, providing evidence of the successful generation of clusters, although the cluster sizes were not determined [23].

The modern era of work on helium nanodroplets can be traced back to approximately 1990, when Toennies' group showed that it is possible to add atoms (Ne, Ar, Kr) to helium nanodroplets [23, 24]. Subsequently it was shown that molecules could be added (such as H<sub>2</sub>, O<sub>2</sub>, H<sub>2</sub>O, CH<sub>4</sub>, and SF<sub>6</sub>) and eventually this led to spectroscopic studies of atoms and molecules inside HeDs, as will be detailed later in section (1.8).

The ready availability of affordable closed-cycle cryostats means that it is relatively straightforward to produce helium nanodroplets. The actual mechanism for forming the droplets depends on the conditions used for the expansion. The possible regimes were first studied in detail by Buchenau *et al.* [25] and were divided into sub-critical and supercritical regimes. In the sub-critical region, the helium expansion takes place through a nozzle at temperatures higher than 11 K, which means that expansion occurs from the gas to the liquid side of the phase diagram (Figure 1.1). Thus in this expansion, regime the HeDs are produced from condensation of helium gas near the nozzle exit. However, if the isentropic expansion starts from the liquid side < 11 K (supercritical region), then liquid helium exits the nozzle and produces droplets by fragmentation [25].

## 1.4 Helium droplet size

The size of HeDs is important in many applications. Fortunately, by varying the expansion conditions the opportunity arises to provide some degree of control over the droplet size. Conditions can be set where the mean number of helium atoms in a HeD ranges from <1000 to >10<sup>10</sup> [24]. In most applications, and certainly those described later in this thesis, droplets with only a few thousand of helium atoms are desirable.

If we assume spherical droplets and that the density of the droplet that is the same as that of bulk liquid helium, then the droplet radius ( $R$ ), in nm, is related to the number of helium atoms,  $N_{\text{He}}$ , by [9]:

$$R \approx 0.22 (N_{He})^{1/3} \quad (1-4)$$

Lewerenz *et al.* [26] executed experiments to determine helium droplet size by a deflection method based on the scattering of SF<sub>6</sub> by a beam of helium droplets. In these experiments the expansion conditions were sub-critical ( $T \geq 14$  K) and therefore helium droplets were produced by condensation of pressurised helium gas. The results were consistent with a droplet size distribution that obeys a log-normal distribution [26,27]. Möller *et al.* [28] developed a scaling law which allows one to estimate the size of HeDs from the expansion conditions and the nozzle diameter,  $d$ :

$$N = 2.834 \times 10^5 (p_o^2 d^{1.7} / T_o^{5.07}) \quad (1-5)$$

where,  $p_o$ ,  $d$  and  $T_o$  are stagnation pressure, nozzle diameter and stagnation temperature. However results obtained by Vilesov *et al.*, using a titration technique [8], were not in agreement with equation (1-5). In the Vilesov experiments, the helium droplet beam collides with argon gas. The collision caused the evaporation of helium atoms from the droplet and thereby increased the pressure of the helium in the chamber [9]. This pressure rise was used to determine the average size of the HeDs. The titration technique showed that at a stagnation pressure of 20 bar and temperature of 5.5 K the helium droplet size will be  $10^9$  atoms [9] while equation (1-5) gives  $3 \times 10^5$  atoms for the same conditions. This is clearly a large discrepancy.

Overall, the helium droplet size distribution follows a log-normal distribution at nozzle temperatures  $\geq 11$  K (subcritical region), while it shows an exponentially decaying size distribution at temperatures lower than 11 K (supercritical expansion) [28]. The mean sizes of helium droplets as a function of nozzle temperature are summarised in Figure 1.3 [9].

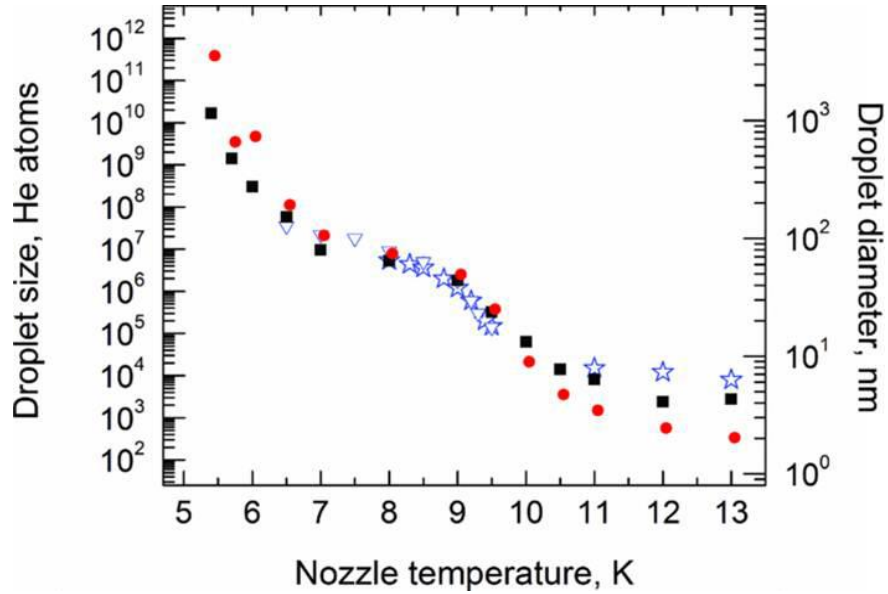


**Figure 1.3.** Helium droplet size as a function of temperature from experimental measurements. The figure is taken from reference [9]. The squares and circles data were extracted from a combination of titration [9] and the stars are from deflection [26,30] techniques.

### 1.5 Dopant pick up

HeDs can capture dopants via collisions with the gaseous form of the dopant (atomic or molecular) [21,23,24,31,32]. For a given HeD size, the probability of picking up  $k$  dopant particles ( $p_k$ ) is dictated by Poisson statistics and is given by [31,33].

$$p_k = \frac{(\sigma\rho l)^k}{k!} \exp(-\sigma\rho l) \quad (1-6)$$

$\sigma$  is the helium droplet cross sectional area and is equal to  $15.5(N)^{2/3} \text{ \AA}^2$ , assuming a uniform helium density ( $\text{cm}^{-3}$ ) equivalent to that of bulk liquid helium. In equation (1-6)  $\rho$  is the pickup gas density ( $\text{cm}^{-3}$ ),  $l$  is the length of the pickup cell and  $k$  is number of particles that are picked up by a droplet [31,33]. The dependence of the pickup probability as a function of dopant partial pressure is shown in Figure 1.4. Equation (1-6) only applies if it is assumed that the droplet cross section is unchanged by the addition of more than one dopant atom/molecule.

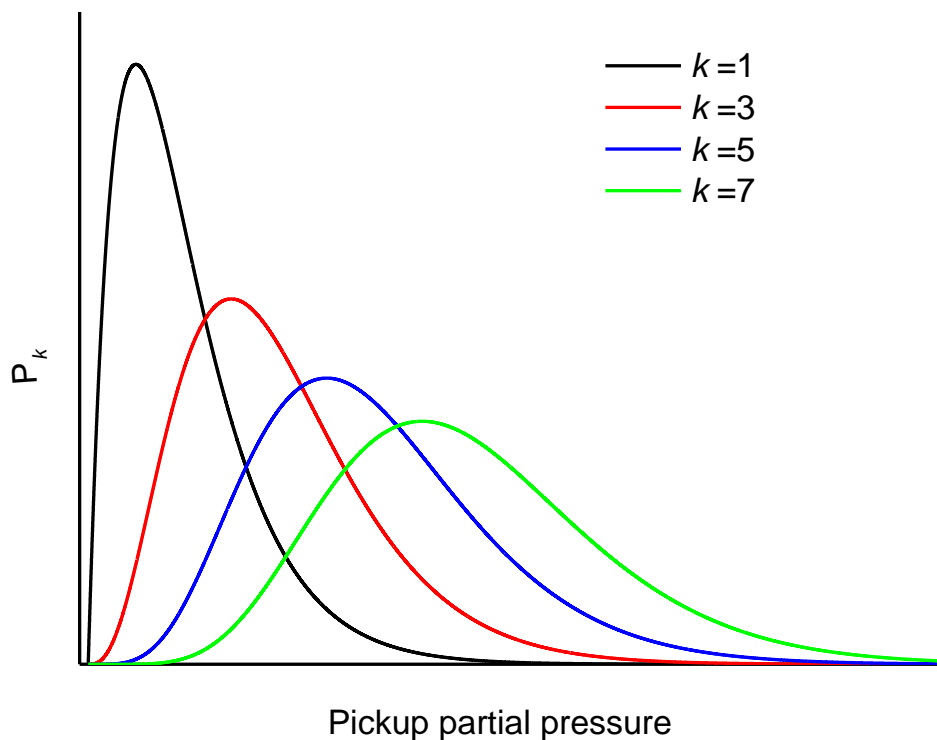


**Figure 1.4.** Poisson distributions showing the probability of picking up  $k$  dopant particles as a function of the partial pressure of the dopants.

When dopants are added to HeDs, atoms/molecules can sequentially attach to a droplet and migrate towards the centre. This mechanism allows the formation of clusters when dopants aggregate at the centre of the droplet. Additionally the clusters

are formed and stabilised under the very low temperature and rapid cooling conditions provided by the helium droplet. Thus in addition to the equilibrium cluster geometry at the minimum of the PE surface, there is also the possibility that some clusters become trapped in non-equilibrium structures in local minima. The energy released from the clustering process will lead to the evaporation of helium atoms. Given the known binding energy of a helium atom to a large helium cluster, which is 0.6 meV, the expectation is that the transfer of 1 eV energy into the droplet will cause the evaporation of 1600 He atoms [21].

A vapour pressure of about  $10^{-6} - 10^{-5}$  mbar is appropriate to capture single dopant particle for small droplets [21], while a lower vapour pressure is suitable for larger helium droplets. Different methods are used to get a suitable dopant vapour pressure. For example, gaseous dopants [34] or those derived from the vapour above volatile liquids are easily added to HeDs. More involatile species will require heating and specially designed ovens may be needed in such cases, as used in some experiments by the Leicester helium nanodroplet group [35-37]. Another option is to use laser ablation to deposit the dopant into the gas phase [38-40].

## 1.6 The location of the dopants

Determining the location of the dopants either on or in the helium droplet was one of the key issues to settle in early HeDs experiments [41]. Theoretical predictions of SF<sub>6</sub> showed that the dopants energetically centred inside the droplets [42,43]. This theory was proved experimentally by Hartmann *et al.* [43]. Their experiment recorded the rotationally-resolved IR spectrum of SF<sub>6</sub> and the findings were consistent with the location of SF<sub>6</sub> in a highly homogeneous environment near to the centre of the droplet [44]. Ancilotto *et al.* derived a formula to predict location of the dopant in a helium droplet by determining the dimensionless parameter  $\lambda$  [45]:

$$\lambda = \frac{\rho \epsilon r_{min}}{2^{1/6} \delta} \quad (1-7)$$

Here,  $\rho$  and  $\delta$  are the density and surface tension of a helium droplet,  $\epsilon$  is the Lennard-Jones binding between the dopant and a helium atom, and  $r_{min}$  is the minimum distance between the dopant and a helium atom [45]. If  $\lambda$  is larger than 1.9 then the dopant should submerge inside the droplet while if  $\lambda < 1.9$  then the energetics favour a dopant located on the droplet surface [45]. An assumption is comparison of the minimum energy of interaction helium atoms with the dopants on the surface and the energy required to create hole to the centre of the helium droplet [31]. If the former is higher than the later, dopants will prefer to enter inside the helium droplet [31]. However, it became clear that all alkali metal atoms reside on the surface of HeDs [31,46,47,48]. This was observed due to the similarity in shifts of band positions between their electronic spectrum in the gas phase and those in HeDs [39,45]. This was explained as the low binding energy between atoms of these materials and helium atoms,  $\sim 10 \text{ cm}^{-1}$  [49]. Stark and Kresin [50] suggested that the strong short range Pauli repulsion between helium and alkalis, which is caused by the diffuse valence *s* orbitals of the latter, overcomes the dispersion force (attractive) of alkali and helium atoms and favours a surface location [51].

The Ancilotto parameters for both  $\text{SF}_6$  and HCN are  $>20$ , values which were proved experimentally [52]. Moreover, it was predicted that most of the alkaline earth metal atoms flat on the surface of HeDs, with values close to the threshold value of 1.9. However, Mg atoms were predicted to have an Ancilotto parameter higher than 1.9 [31] and experiments showed location of Mg within HeDs [53].

## 1.7 Ionization Processes in Helium Droplets

The simplest way to detect the formation of helium droplets and the dopants is to ionize them by electron ionization [54-58]. To do this, the incident electron energy needs to exceed a repulsive barrier for electron penetration into the droplet that ranges from 0.6 to 1.1 eV, depending on the helium droplet size [59]. The ionization process can be viewed as an inelastic collision between an electron and a helium atom, and so will have a threshold energy close to that of a single He atom (24.59 eV [60,61]). Ions of the dopant in a helium droplet are produced either by charge transfer

or by Penning ionization [62]. Penning ionization involves the electronic excitation of a helium atom by collision with an electron. The resulting electronically excited helium atom is mainly limited to a surface location and so is of less interest as a source of ions for work with doped helium droplets. In charge transfer, a helium atom is ionized via electron impact to create  $\text{He}^+$  [62]. The positive charge is mobile and can hop onto an adjacent helium [63]. Ultimately, the charge will either reach the dopant, whereupon it will transfer irreversibly, or it will localise on the helium, generating the  $\text{He}_2^+$  dimer [62]. In the latter case the  $\text{He}_2^+$  can act as a nucleation centre for forming  $\text{He}_n^+$  cluster ions. The available evidence suggests that the charge can hop from helium atom to helium atom  $\sim 10$  times before it will localise to create  $\text{He}_2^+$  [63,64] which happens within in 60 – 80 fs [64,65]. Thus, in large helium droplets the probability of charge transfer to the dopant is far lower than in a small droplet.

Both  $\text{He}_n^+$  cluster ions and dopant ions may be ejected into the gas phase and can be detected in a mass spectrometer after ionization. Currently it is not clear how these ions escape from the droplet. One possibility is that the droplet simply fragments following the energy release from charge transfer and the dopant ion is simply able to escape into the gas phase.

## 1.8 Spectroscopy in helium droplets

The first spectroscopic study of a molecule in a HeDs was reported in the early 1990s [66]. This experiment, by Goyal *et al.*, recorded the IR spectrum of  $\text{SF}_6$  [41,67]. While it is challenge to approach 0 K by seeded supersonic beams techniques, the steady state temperature of helium droplet was discovered through spectroscopy experiments of rotational spectrum of  $\text{SF}_6$  [68,21]. It was observed that excitation of helium droplets with a  $\text{CO}_2$  laser leads to evaporation of helium atoms, which was observed via a decline in intensity of helium signal via bolometric detector, and decreasing the helium temperature to a stable temperature of 0.37K [21,44]. The dopants within helium droplets cool directly to the same temperature [21,44]. Here, the superfluidity of HeDs provides mobility to the dopants to move freely and to grow clusters [21].

In a spectroscopic experiment of HeDs, dopants are excited by an external radiation source. This absorbed energy will eventually dissipate into the droplet and will bring about evaporation of some of the helium atoms. As result the absorption process can be registered by a reduction in the helium droplet size as a function of applied external wavelength. The simplest way of measuring this reduction in helium droplet size is via mass spectrometry and specifically by a reduced ionization cross section. This approach to recording optical spectra is known as depletion spectroscopy.

The depletion technique has been used particularly successfully for recording vibrational spectra of molecules in helium nanodroplets. The reason for this is that rovibrational quenching by the surrounding helium is a relatively fast process relative to the time required for the droplets to travel from the point of excitation to the point where subsequent detection takes place [66]. During the time of transition to the detector, the helium droplet can evaporate hundreds of atoms as it approaches its steady state temperature of 0.38 K [66]. The very low temperature and high thermal conductivity of the HeDs causes rapid quenching of most dopants.

Since the earliest experiments of Goyal *et al.*, depletion spectroscopy has been used to study a wide range of molecules and molecular complex of Van der Waals clusters in HeDs [41,67].

## **1.9 The structure of this thesis**

In the current chapter, the production and properties of HeDs and doped HeDs have been described. The low temperature, high thermal conductivity and the superfluidity of HeDs make them unique environment in which to study molecules and clusters.

In Chapter 2, the experimental setup used for the spectroscopic work in subsequent chapters is described. In Chapter 3, work is described in which there is evidence for the first observation of the cyclic water heptamer and the cyclic water octamer in HeDs. This is followed in Chapter 4 by an IR spectroscopic study of even larger water clusters. In Chapter 5, the structures of methanol clusters in HeDs is reported. In Chapter 6, IR spectra of the mixed  $(\text{CH}_3\text{OH})_2\text{H}_2\text{O}$  and  $(\text{CH}_3\text{OH})_3\text{H}_2\text{O}$  clusters are described. Finally, in Chapter 7, a study of mixed iodine/water clusters is presented

## Chapter 2

### *Experimental Apparatus*

#### 2.1 Overall system summary

The overall experimental setup employed in this work consists of three vacuum chambers (Figure 2.1) which are constructed from stainless steel. The first chamber contains a helium gas supply, a cold head for cryocooling, and a nozzle that generates the helium droplets (HeDs). The middle chamber includes pickup cells where dopants are added to the HeDs. Finally, the last chamber (detection chamber) contains a quadrupole mass spectrometer. The detection chamber is also where the laser beam for doing spectroscopy enters the vacuum system. There are two gate valves in the vacuum system that allows the vacuum chambers to be individually vented if required.

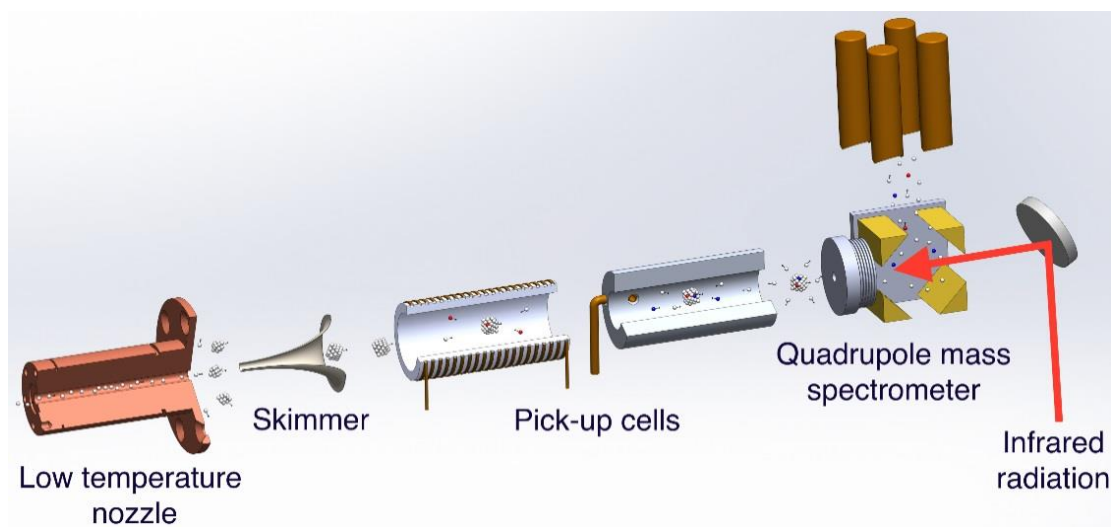


**Figure 2.1.** Diagram showing the main parts of the experimental system; low temperature nozzle, a skimmer, pick up cells , a quadrupole mass spectrometer and the laser source[69]. .

The first chamber contains the helium droplet source. To generate HeDs the nozzle must be cooled to a low temperature. This is achieved with a closed-cycle cryostat (F-50, *Sumitomo Heavy Industries*), which cools the high purity pressurised

helium gas (99.999%, BOC). The temperature of the head cool can be varied across the range 300 K down to 2 K. This degree of control is possible through the combination of a heater on the cold head and a temperature controller unit (LakeShore 336). The fluctuation of the temperature is  $\pm 0.2$  K. The cooled helium expands through a pinhole nozzle (Pt:Ir (95:5) produced by *Günther Frey GmbH & Co. KG*) with 0.1 mm thickness and with an aperture diameter of 5  $\mu\text{m}$ . The nozzle is positioned between two copper parts and sealed to both by indium washers (Figure 2.2). One side is connected to a cylinder with a channel of 1mm diameter through it, through which the helium gas flows, while the second side is connected to a copper faceplate with a conical shape 90° diverging outwards to the helium chamber with aperture diameter of 0.5 mm. This conical region provides the exit region of the nozzle.

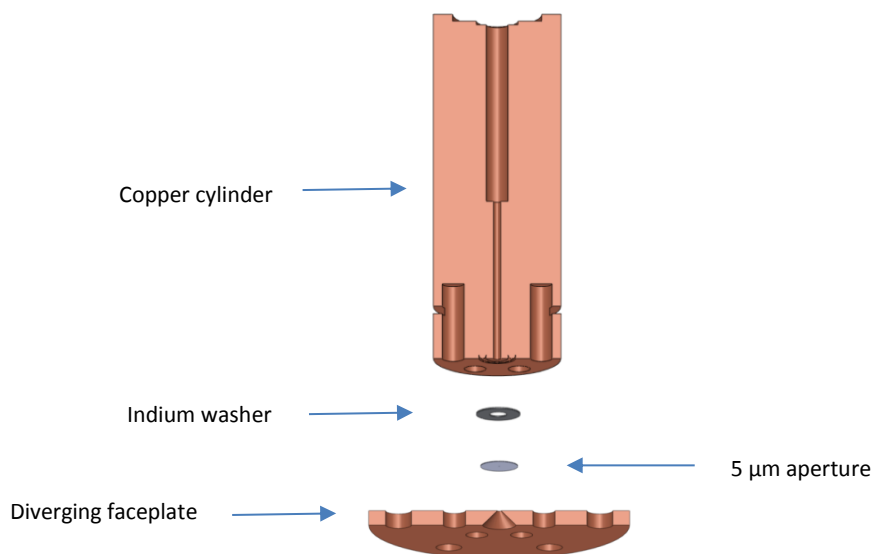


**Figure 2.2.** Schematic diagram of the nozzle shows its position [69].

There is an X-Y-Z translation stage for the cryostat that makes it possible to accurately align the nozzle with the skimmer. The source chamber (first chamber) has a pressure of  $4 \times 10^{-5}$  mbar when the nozzle is at 16 K and the helium stagnation pressure is 32 bar. The vacuum is provided by two large turbomolecular pumps

(*Oerlikon-Leybold -TURBOVAC MAG W 2800*), each with a pumping speed of 2650 litres/second. These pumps are backed by a single roots pump (*RUVAC-Oerlikon-Leybold*) with a pumping speed of  $304 \text{ m}^3 \text{ h}^{-1}$ . The roots pump is in turn backed by a scroll pump (*Edwards XDS 46i*) with a pumping speed of  $40 \text{ m}^3 \text{ h}^{-1}$ .

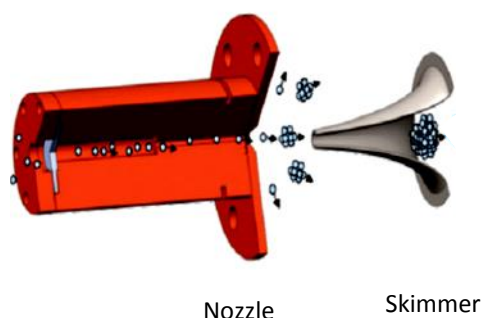


**Figure 2.3.** Schematic of the nozzle and the first skimmer [69].

A collimated stream of helium droplets is obtained via the use of a nickel skimmer (Figure 2.3), which selects the central portion of the droplet expansion. The skimmer has a 0.5 mm aperture diameter and is located at a distance of about 1.5 cm downstream from the nozzle aperture. The HeDs enter the second vacuum chamber after passing through the skimmer.

The second chamber contains the pickup cells, which are cylindrical stainless steel cylinders of 6 cm length, 4 cm outer diameter and 0.6 cm aperture diameter (see Figure 2.4). There is another channel (diameter 0.3 cm) that meets the central channel at an angle near the centre of the pickup cell. This channel is used to add the dopants' vapour from the outside of the vacuum system. Gas/vapour entering this angled channel is provided by way of a copper tube that connects to a needle valve outside the vacuum system. A liquid nitrogen cooled trap is used in this chamber to decrease the pressure of the pickup chamber by cooling down the system temperature since it condenses the species molecules such as water molecules in the background of the system .

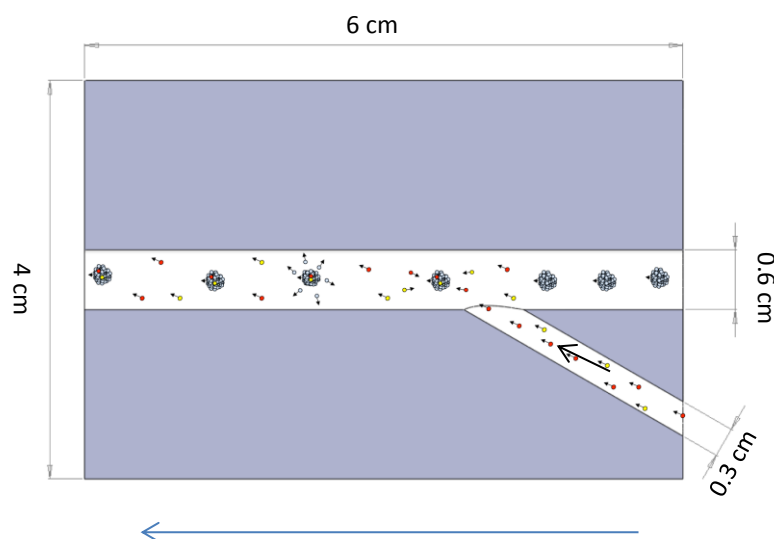


**Figure 2.4.** Schematic of the pickup cell with dimensions [69].

The needle valve adjusts the flow of incoming gas/vapour into the pickup cell. When the needle valve is closed and no helium is flowing, the pickup chamber pressure is typically  $2 \times 10^{-7}$  mbar. The pumping in this chamber is provided via a turbomolecular pump (*Oerlikon Leybold- MAC W 600 P*) with a pumping speed of 570 liters/second, which is backed by a rotary pump (*Pfeiffer Vacuum*) with a pumping speed of  $24 \text{ m}^3 \text{ h}^{-1}$ . The pressure increases to  $4 \times 10^{-7}$  mbar once helium droplets are added.

The detection chamber contains a quadrupole mass spectrometer. In this chamber, the laser beam enters the detection system through a sapphire window. The detection chamber is pumped by a turbo pump (*Oerlikon Leybold- MAC W 400 P*) with a pumping speed of  $280 \text{ l s}^{-1}$  and is backed via a scroll pump (*Edward- NXDS15i Scroll Pump*) with a pumping speed of  $15 \text{ m}^3 \text{ h}^{-1}$ . This chamber has a base pressure of  $\sim 10^9$  mbar, which rises to  $\sim 10^8$  mbar when helium droplets pass through it.

## 2.2 Main experimental equipment

### 2.2.1 Quadrupole Mass Spectrometer

A quadrupole mass spectrometer (QMS) (MAX-1000) is used to detect HeDs and the dopants within HeDs (see Figure 2.5). The QMS uses an electron bombardment source with a typical electron kinetic energy of 90 eV to ionize the HeDs. The expected ionization mechanism is that a helium atom in the droplet is first ionized. The resulting  $\text{He}^+$  can then transfer its charge by hole hopping [62], as was discussed in Chapter 1. After the ionization process any positively charged ions enter the quadrupole system for mass selection and then onwards to an ion detector (not shown in Figure 2.5).

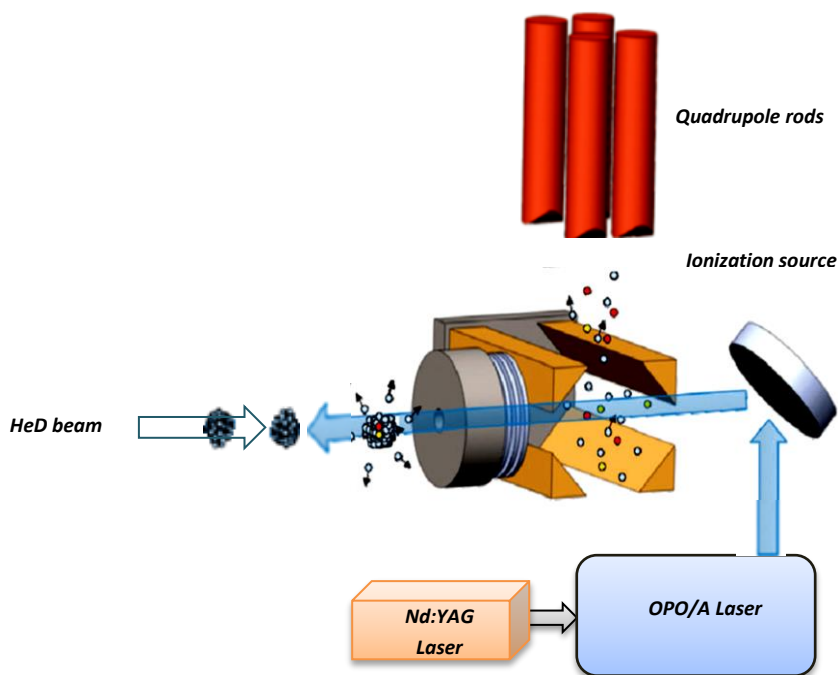


**Figure 2.5.** Quadrupole mass spectrometer region of helium droplet apparatus [69].

The quadrupole rods act as a mass filter. Ions that pass through the system reach an ion detector, which amplifies the signal to produce a cascade of electrons. The QMS can detect ions in the  $m/z$  range 2 - 4000. There is a SIM (single ion mass) scan function within the propriety software that is used for recording spectroscopic

data via detection of a specific ion. In addition, this process has an important role in alignment of the nozzle with the skimmer since it shows any change in the intensity of detecting  $\text{He}_n^+$  ions ( $n=2$ ). Moreover, the SIM scan provides information to set optimum conditions for creating HeDs via nozzle temperature, the helium pressure and amount of pick up dopants by detecting the ion signal of the dopant.

The size of the droplets is controlled by the helium stagnation temperature and pressure. The optimum size is different in each experiment and depends on what is the aim to be achieved in a particular experiment. For IR spectroscopic studies the typical aim is a mean droplet size between 5,000 and 10,000 helium atoms.

The mass spectrum provides information about the composition of species within the helium droplets. The mass spectrum in the range of  $m/z = 2$  to  $m/z = 100$  for pure helium droplets is shown in Figure 2.6. The spectrum shows a large amount of helium dimer ions ( $\text{He}_2^+$ ) in comparison with other non-helium containing species. The biggest contaminant comes from cationic water at  $m/z = 18$ , along with  $\text{OH}^+$  at  $m/z = 17$ . There is small amount of  $\text{O}^+ = 16$ ,  $\text{N}_2^+$  at  $m/z = 28$  and  $\text{CO}_2^+$  at  $m/z = 44$ , which indicates that any leaks in the vacuum system are very small. These signals also could be from helium cluster ions, however, if  $\text{N}_2$  and  $\text{CO}_2$  are present then they are very low level because the peak intensities do not rise significantly above the level of the surrounding helium cluster ions. The water comes primarily from residual water, which is presumably released slowly from cracks and crevices in the vacuum system. Much of the water vapour originates from the final (QMS) chamber, as shown by isolating this chamber with the gate valve.

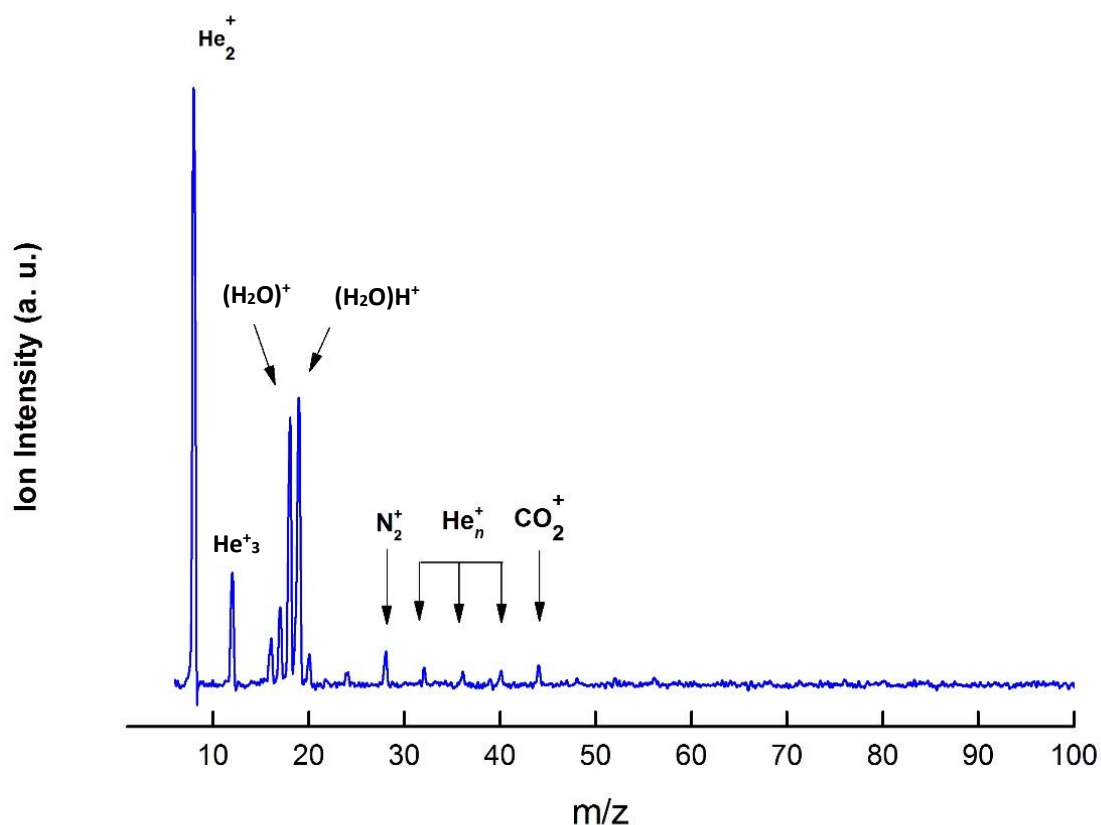


**Figure 2.6.** Mass spectrum of the background of the vacuum system with the nozzle at 16 K, a helium stagnation pressure of 33 bar and QMS ionization energy of 90 eV.

### ***2.2.2 Laser System for Depletion Spectroscopy***

The infrared radiation used for the spectroscopic work is generated from an optical parametric oscillator/amplifier (OPO/A) laser (Laser Vision), which is pumped by a Nd:YAG laser (Continuum Surelite II -10). This delivers tuneable radiation over 2500-4000 nm. Excitation of dopants via the laser radiation is detected by depletion spectroscopy, as will be detailed later in section 2.2.3.

#### **2.2.2.1 Nd: YAG laser**

In a Nd:YAG laser, the amplifying laser medium consists of  $\text{Nd}^{3+}$  ions inside a yttrium aluminium garnet (YAG) host. Population inversion comes from a flash lamp and a high intensity pulsed output is obtained via a Q-switch. The output at 1064 nm delivers

pulses at a repetition rate of 10 Hz with horizontal polarization in the particular experiments performed in this work.

#### **2.2.2.2 Optical parametric oscillator/amplifier (OPO/A)**

The optical parametric oscillator/amplifier (OPO/A, LaserVision) provides a widely tunable source of IR radiation (710 – 885 nm, 1.35 – 5.0  $\mu\text{m}$ ) with high output intensity. The optical configuration used for the present work (Figure. 2.7), provides a continuous tuning range in the mid-IR from 2.2 to 5.0  $\mu\text{m}$ . The OPO/A is pumped by the 600 mJ, 1064 nm output from a Nd:YAG laser operating at 10 Hz, resulting in an OPO/A pulse energy of approximately 12 mJ from 2.2 to 3.5  $\mu\text{m}$ , which gradually decreases to <0.5 mJ at 5.0  $\mu\text{m}$ .

There are two main stages in the OPO/A system. The first stage is an OPO, which contains a potassium titanyl phosphate (KTP) crystal and is used to generate a near-IR beam with a continuously tunable wavelength range from 1.35 to 2.2  $\mu\text{m}$ . The second stage is an OPA, which contains four potassium titanyl arsenate (KTA) crystals and converts the near-IR output from the OPO into a mid-IR beam.

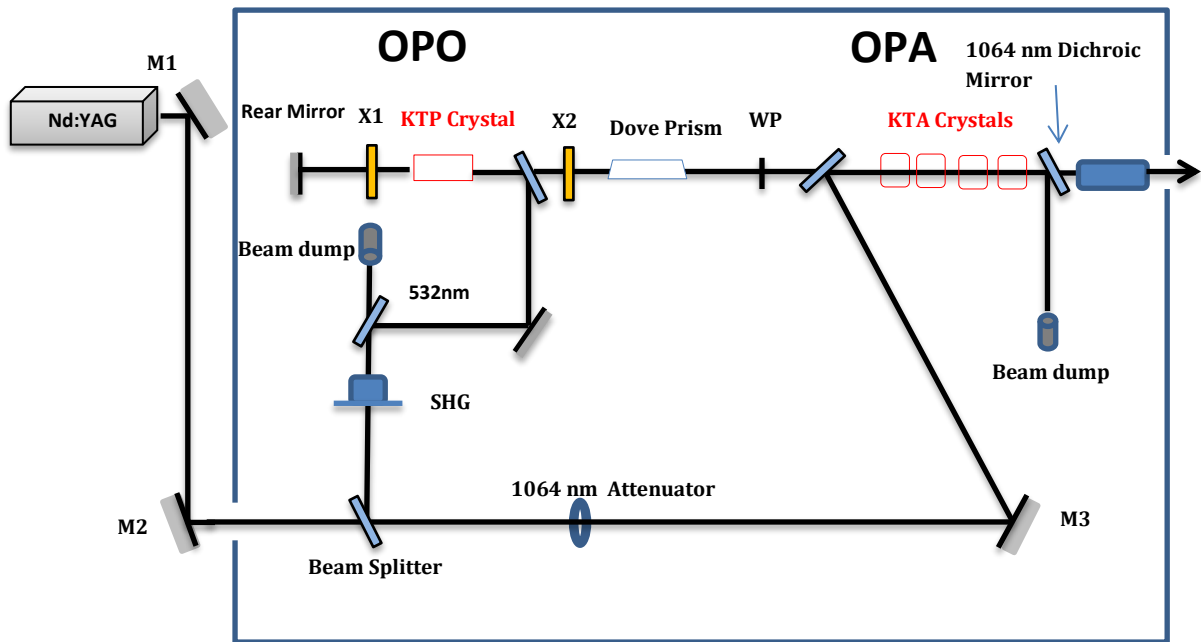


**Figure 2.7.** Configuration of the OPO/A laser system. M1, M2, M3 are turning mirrors. SHG = second harmonic generation. WP = wave plate. X1 and X2 are a totally reflecting mirrors and an output coupler, respectively.

After entering the OPO/A, the pump laser beam is split into two beams by a beam splitter. The reflected beam passes through a nonlinear frequency doubling crystal (KTP) to generate 532 nm radiation via second harmonic generation (SHG). The 532 nm beam then enters the OPO stage.

The OPO provides tuneable radiation in the near-IR. It consists of an optical cavity (optical resonator) containing a nonlinear crystal (KTP). The optical cavity consists of two plain mirrors, a totally reflecting mirror (X1) and an output coupler (X2). The nonlinear response from the KTP crystal leads to parametric conversion and the frequency of the output can be controlled via angle tuning of the KTP crystal. Essentially, the 532 nm pump beam (frequency  $\nu_3$ ) is divided into two beams with different frequencies, a signal beam ( $\nu_1$ ) and a lower frequency idler beam ( $\nu_2$ ), such that the photon energy of the pump beam ( $h\nu_3$ ) is equal to the sum of the photon energies for the idler ( $h\nu_1$ ) and signal ( $h\nu_2$ ) beams [70-72]. This process occurs when

the phase matching condition is satisfied, as represented by the conservation of momentum relationship [70-72]:

$$hk_3 = hk_1 + hk_2 \quad (2-1)$$

Here  $k_1$ ,  $k_2$ ,  $k_3$  are wave vectors that are related to frequencies of  $\nu_1$ ,  $\nu_2$  and  $\nu_3$ , respectively by  $k = n_\nu \nu/c$ , where  $c$  is the velocity of light in vacuum and  $n_\nu$  is the refractive index of the crystal at frequency  $\nu$  [69].

The idler output beam from the OPO stage passes through a Dove prism and half-waveplate (wp) before being entering the OPA stage. The waveplate rotates the vertically-polarised idler beam to horizontal polarization, while the Dove prism is used to improve the collimation of the OPA output beam.

The portion of the Nd:YAG output beam at 1064 nm that passed through the beam splitter, which is located near the entrance of the OPO/A enclosure, is used to pump the OPA stage containing four KTA crystals. This pump beam is combined with the idler beam from the OPO system and, through difference frequency mixing, it generates the tuneable mid-IR radiation. The OPA system is similar to the OPO system, however, it excludes the optical cavity (mirrors) and so radiation is generated through a single optical pass. A dichroic mirror is used to reflect the 1064 nm beam, which is dumped at beam dump 2, while the signal and idler passes through a Brewster polarizer. The polarizer allows selection of either the vertically polarized (idler) beam in the mid-infrared region (as used in this work) or horizontally polarized (signal) beam depending on the orientation of the polarizer.

The output wavelength is software controlled via a dedicated personal computer (PC). The wavelength is controlled via rotation of the KTP crystal in the OPO cavity. The KTA crystals in the OPA stage are also rotated during wavelength scanning in order to maintain maximum output power through phase matching.

The output beam travels 2.3 m to the vacuum chamber and passes through a pipe contains  $N_2$  gas, which reduces absorption of the IR laser beam by the ambient air. Silver-coated broadband metallic mirrors are used to reflect the IR beam along the path of the helium droplet spectrometer and a lens of focal length 1 m is used to focus

the IR beam. Failure to correctly align the laser beam with respect to the HeD beam can have a large effect on the depletion signal. In the mid-IR region near  $3500\text{ cm}^{-1}$  the typical mean pulse energy of the OPO/A beam as it enters the third vacuum chamber is 8 mJ.

### ***2.2.3 Depletion spectroscopy***

Depletion spectroscopy is the most popular technique used to record spectra of dopants in HeDs. As the molecules are excited via an excitation source (such as a laser), the dissipated heat from excited dopants shrinks the HeDs size which causes a reduction in the size of the HeD [60].

In early depletion experiments, a bolometer was used to detect depletion spectra, which is sensitive to the thermal energy possessed by a droplet and can determine when the droplet is smaller. An alternative to bolometer detection is the use of a mass spectrometer. Here, signal for ions are monitored and any reduction in helium droplet size results in a fall in ion signal since the electron ionization cross section scales with the geometrical size of the HeDs.

Since the OPO is pulsed, a depletion spectrum requires the use of time-synchronised events. The delay generator generates trigger pulses of time delay and width of both flash fire and Q-switching for the YAG laser, and also deliver a trigger pulse to the photon counter (SRS 400). The photon counter is used to count the ion signal from the QMS and has two independent channels, A and B (Figure 2.8). Channel A counts the ion with the laser present while channel B counts the background ion signal at a time when the laser pulse is absent, as shown in Figure 2.8. Both channels A and B have the same time width. The difference in the integrated signals in channels A and B is the IR depletion signal. This is averaged over multiple shots and is monitored as a function of the wavelength of the OPO/A to construct an IR spectrum. Figure 2.8 shows an example of a depleted ion signal caused by IR absorption.

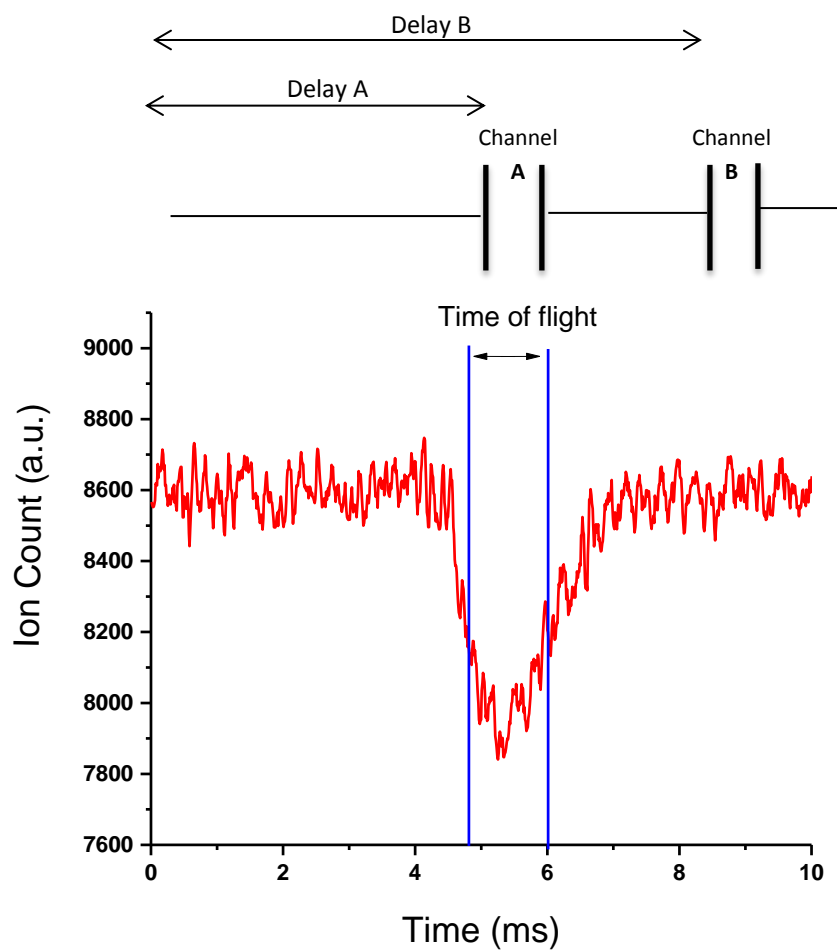


**Figure. 2.8.** Ion signal as a function of time when the IR radiation is resonant with a dopant transition. The red peak shows a decline in the ion intensity because of shrinkage in the helium droplet size on IR absorption, which reduces the HeD ionization cross section. The width of the depletion is roughly equal to the droplet transit time from the pickup cell to the QMS.

## Chapter 3

### *Infrared spectroscopy of pure water clusters in HeDs*

#### 3.1 Introduction

Many theoretical and experimental studies have been reported on water clusters  $(\text{H}_2\text{O})_n$  where  $n \leq 10$  [73-100]. The structure of the water dimer,  $(\text{H}_2\text{O})_2$ , was first studied experimentally via electric resonance spectroscopy in the gas phase in 1977 by Dyke *et al.* [73]. They detected rotational transitions of the dimer in the radiofrequency and microwave regions and found that it has a “*trans linear*” structure, in agreement with their own theoretical calculations. Much theoretical work has been carried out since then on the dimer and on larger clusters including the trimer, tetramer and pentamer. For example, Xantheas and Dunning calculated optimum structures of water clusters using the MP2 method with a double zeta basis set for  $(\text{H}_2\text{O})_{2,3,4}$  [76]. They predicted cyclic structures as the most stable arrangement for water clusters of  $(\text{H}_2\text{O})_{3-5}$ . They also found that the distance between adjacent oxygen atoms decreases as the number of water molecules increases. There is a clear structural change from a cyclic structure for the pentamer to a non-cyclic structure for the octamer in theoretical study by Knochenmuss *et al.* [75]. Experimental results via far-infrared spectroscopy in the gas phase for  $(\text{H}_2\text{O})_3$  [81],  $(\text{H}_2\text{O})_4$  [82] and  $(\text{H}_2\text{O})_5$  [79] have confirmed cyclic structures in the gas phase, where each water acts as single donor and acceptor.

The IR spectra of the dimer and trimer in HeDs were first recorded by Huisken *et al.* [80,81]. They had recorded depletion IR spectra as a function of scattering angle of a helium beam, giving some degree of mass selectivity [81]. The trimer was consistent with a cyclic structure [80], in agreement with the gas phase. Huisken *et al.* also observed spectra which are consistent with cyclic structures for the tetramer and pentamer.

Theoretical studies have shown that water clusters larger than the pentamer have global minimum energy structures which are non-cyclic [80,82]. This occurs because the cyclic isomers in these larger clusters do not make full use of the possible

hydrogen bonding opportunities when compared with more 3-D structures [80,82]. For example, MP2 calculations on the hexamer have predicted a prism structure as the lowest energy minimum [77]. Calculations have predicted the most stable isomer for water heptamer to be a prism isomer [93,95] at low temperature and a chair isomer at higher temperatures ( $\geq 200$  K) [93]. The prism heptamer has a structure which is essentially an octamer cubic structure with one of the water molecules missing [95]. This can be produced either by adding one water molecule to the stable structure of the water prism hexamer or by removing one water molecule from the cubic water octamer [94]. Acelase *et al.* predicted 38 isomers of water heptamer via B3LYP/6-31+G (d) and MP2/6-311++G (d, p) calculations, the lowest energy of which was again predicted to be a prism structure [96]. These results collectively confirm that the prism structure is likely to be the global minimum for the water heptamer.

Experimentally, the water hexamer structure was first observed as a cage in a supersonic expansion by measuring rovibrational spectra [81]. More recent experiments have used broadband microwave spectroscopy and found evidence for the presence of cage and book hexamer structures, their own theoretical predictions predict the cage isomer to have the lowest energy [94]. Experiments on water clusters formed in an argon expansion yielded a book structure as the observed isomer [90]. In these IR experiments the water cluster is assumed to have attached argon atoms, which may affect the relative stabilities of the possible isomers. A depletion spectroscopic study of larger water clusters in the gas phase has been reported and showed the water heptamer,  $(\text{H}_2\text{O})_7$  [86]. In that study multiple structures were identified of heptamer cage isomer and the theoretical calculations predicted heptamer to be a cage structure, like an octamer  $(\text{H}_2\text{O})_8$  but having lost one double acceptor or donor water molecule [86].

Nauta and Miller [100] recorded high quality IR spectra of water clusters in HeDs in the OH stretching region. An exciting finding from this work was the observation of a cyclic isomer of the water hexamer in helium nanodroplets. Indeed, this isomer was found to be the main isomer produced for the hexamer in HeDs, in stark contrast to gas phase studies. A second and weaker IR absorption band was also seen and assigned to the cage isomer [101]. However, recent theoretical calculations

by Wang and Bowman have shown that this weak peak is most likely from the bending overtone of the cyclic water hexamer, which therefore suggests that the cyclic isomer is the only one formed in HeDs [102]. There was no observation of any signal attributable to the heptamer or any larger water clusters in the HeD work by Nauta and Miller [100]. A possible explanation is that the OH stretching bands of the water heptamer are masked by the stronger bands from smaller water clusters [93,101]. Note that bolometric detection was used, which is not mass selective [93,101].

**Table 3.1** Experimental and calculated vibrational data ( $\text{cm}^{-1}$ ) for water clusters in the OH stretching region.

Water clusters in gas phase <sup>A</sup>			Water clusters in HeDs		Harmonic calculations		Anharmonic calculations	
Water cluster	Free OH	Bonded OH	Free OH	Bonded OH <sup>B</sup>	Mp2/ aug-cc-pVDZ		Local Monomermodel <sup>C</sup>	
					Free OH	Intense bonded OH-bonded	Free OH	Intense bonded OH
H <sub>2</sub> O	3755.97 <sup>A</sup>				3940	3805		
(H <sub>2</sub> O) <sub>2</sub>	3735 <sup>A</sup>	3601 <sup>A</sup>	3729 <sup>B</sup>	3597 <sup>B</sup>	3897	3704		
(H <sub>2</sub> O) <sub>3_cyclic</sub>	3726 <sup>A</sup>	3533 <sup>A</sup>	3717 <sup>B</sup>	3529 <sup>B</sup> , 3544 <sup>B</sup>	3895	3632, 3641	3717 <sup>C</sup>	3494 <sup>C</sup>
(H <sub>2</sub> O) <sub>4_cyclic</sub>	3714 <sup>A</sup>	3416 <sup>A</sup>	3717 <sup>B</sup>	3394 <sup>B</sup>	3884	3484	3719 <sup>C</sup>	3390 <sup>C</sup>
(H <sub>2</sub> O) <sub>5_cyclic</sub>	3714 <sup>A</sup>	3360 <sup>A</sup>	3717 <sup>B</sup>	3353 <sup>B</sup>	3886	3433, 3442	3726 <sup>C</sup>	3366 <sup>C</sup>
(H <sub>2</sub> O) <sub>6_cyclic</sub>		3346	3717 <sup>B</sup>	3335 <sup>B</sup>	3892	3417	3726 <sup>C</sup>	3375 <sup>C</sup>
(H <sub>2</sub> O) <sub>7_cyclic</sub>		<b>3320</b>	<b>3717</b>	<b>3320</b>	3895	3415,3420	3710 <sup>C</sup>	3398 <sup>C</sup>
(H <sub>2</sub> O) <sub>8_cyclic</sub>		<b>3344</b>	<b>3717</b>	<b>3346</b>	3892	3430	3716 <sup>C</sup>	3348 <sup>C</sup>

<sup>A</sup> Vibrational transitions of H<sub>2</sub>O from reference [20] and (H<sub>2</sub>O)<sub>2-5</sub> from references [81] and [103].

<sup>B</sup> Water OH stretching frequencies from dimer to hexamer in HeDs taken from reference [104] while bold data ((H<sub>2</sub>O)<sub>7,8</sub>) are from the current work.

<sup>C</sup> Reference [102].

The work in the present chapter employed mass selectivity to try to detect the water heptamer and larger water clusters, and then IR spectra of the  $(\text{H}_2\text{O})_7$  and  $(\text{H}_2\text{O})_8$  clusters were observed in HeDs via depletion spectroscopy. *Ab initio* calculations were performed to support assignment of the experimental spectra. As will be described, the calculations showed that the experimental IR spectra of both  $(\text{H}_2\text{O})_7$  and  $(\text{H}_2\text{O})_8$  are from cyclic structure of both water clusters, even though the cyclic structure is not the global energy minimum in either case.

## 3.2 Experimental

The HeDs were formed at a nozzle temperature of 16 K and helium gas pressure of 33 bar. Under these conditions the mean helium droplet size is expected to be approximately 5000 atoms [35,105]. Water molecules were added to the helium droplets in a pick-up cell and controlled via a needle valve. . The electron impact energy of ionization source was 70 eV.

HeDs were exposed to IR radiation from the OPO/A system with an average input pulse energy of 8.5 mJ. Depletion spectra were recorded as a decline in the signal in a specific mass channel. This wavelength-dependent signal depletion is caused by the evaporation of helium atoms when a dopant absorbs the radiation (see chapter 2).

## 3.3 Computational details

*Ab initio* calculations were carried out for water clusters ranging from the trimer to the octamer. These calculations used second-order Møller-Plesset (MP2) theory and augmented correlation consistent basis set of double zeta quality (au-cc-pVDZ). The software used for these calculations was Gaussian 03. Predictions of the IR spectra were made using the harmonic oscillator model. Predictions of anharmonic IR spectra of cyclic water clusters were also provided by Yimin Wang and Joel Bowman (Emory University, Atlanta).

Two different scaling factors are chosen in the harmonic theoretical calculations of the heptamer water clusters (Figure 3.8) and the octamer (Figure 3.9) in the present work. These scaling factors of frequencies ( $\text{cm}^{-1}$ ) of peaks in IR spectrum are used to bring the IR spectrum of calculated cyclic water hexamer into agreement with the IR spectrum for the cyclic water hexamer that observed by Millers group [104]. One scaling factor is used for the free OH stretches (0.955) and another one for the bonded OH stretches (0.972) since it was not possible to fit theoretical spectrum with the experimental IR spectra via a global scaling factor.

### 3.4 Results and Discussion

#### 3.4.1 *Ab initio* calculations of cyclic water clusters

*Ab initio* calculations have been performed in this study for water clusters,  $(\text{H}_2\text{O})_n$ , for up to  $n = 8$ . The process of finding energy minima began through the addition of a single water molecule to the most stable structure of the water cluster of smaller size. The starting point was an optimised  $\text{H}_2\text{O}$  monomer, to which second water was added and then the system was subjected to full geometry optimisation. A third molecule was then added to obtain a cyclic trimer structure. This procedure was continued for successively larger clusters up to water octamer. However at the upper limit, it was not possible to obtain a cyclic water nonomer because it always changed to a bicyclic structure during the geometry optimisation process.

The calculated cyclic structures of water clusters from  $(\text{H}_2\text{O})_3$  to  $(\text{H}_2\text{O})_8$  are presented in Figure 3.1. Each water molecule within the cyclic structure is both a single donor and single acceptor (DA). The OH groups involved in hydrogen bonds are called *bonded* OH groups while those which do not participate in hydrogen bonding are called *free* or dangling OH groups. The bonded OH stretching band of the cyclic water structures from  $(\text{H}_2\text{O})_3$  to  $(\text{H}_2\text{O})_8$  is predicted to progressively shift to the red in moving from the water trimer to heptamer cluster, and then shifts back to the blue a little for the octamer water (Figure 3.3). As might be expected, the free OH bands are barely affected by the change in cluster size. The blue shift in moving from  $(\text{H}_2\text{O})_7$  to  $(\text{H}_2\text{O})_8$  can be accounted for by the increased structural strain, i.e. the bond angles are

no longer optimum for making the strongest possible hydrogen bonds. Consequently, the OH bonds actually become marginally stronger and hence the small blue shift relative to the heptamer [106]. Because of the lower symmetry in the odd-numbered water clusters there are actually two closely spaced bonded OH stretching bands, whereas for the even clusters the high symmetry delivers only a single IR band.

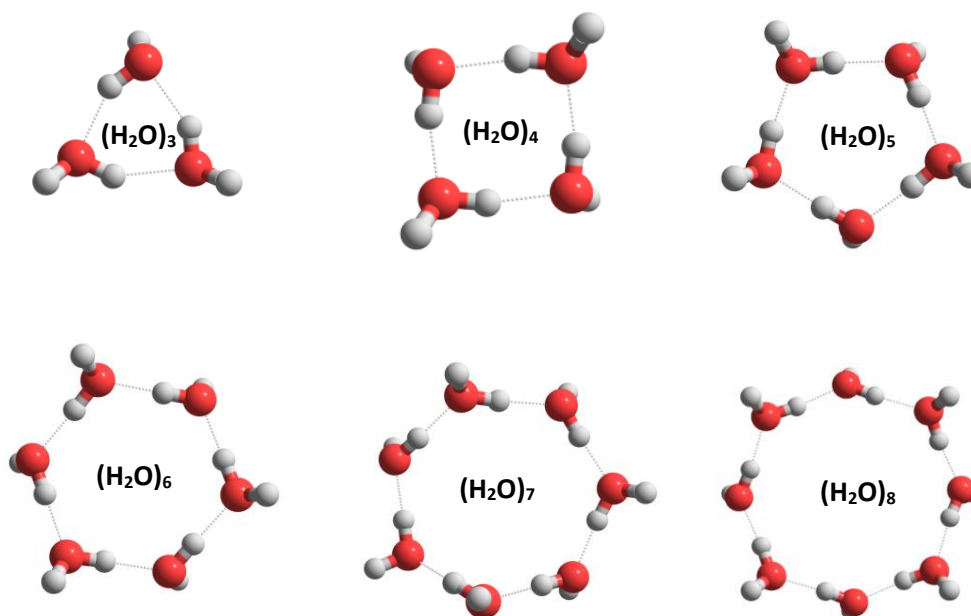


**Figure 3.1.** Cyclic water structures ((H<sub>2</sub>O)<sub>3-8</sub>) calculated by MP2 calculations

The different structures of the heptamer water were optimised and their predicted IR spectra in the OH stretching region are shown in Figure 3.2. The prism structure (Figure 3.2 (a)) is found to have the lowest energy, which is in agreement with previous theoretical studies [93,95,96], The other isomers have total energies which follow the sequence chair < bicyclic < full cyclic. The prism and chair structures of the heptamer are predicted to have IR spectra which are very different from the bicyclic (Figure 3.2(c)) and cyclic isomers (Figure 3.2 (d)). It is the variety of OH bonding environments in the 3-D structures that create a greater spectral complexity for the 3D (non-cyclic) isomers. While each water monomer in cyclic (H<sub>2</sub>O)<sub>7</sub> has only one acceptor

and one donor bond, the 3-D water heptamer structures can have donor-accepter-accepter and donor-donor-accepter hydrogen bonds. In contrast the cyclic heptamer has a calculated IR spectrum with a single dominant band in the bonded OH stretching region and a much weaker free OH stretch at higher frequency. The bicyclic (Figure 3.2 (c)) structure shows an extra OH stretching band in the bonded OH region but is still relatively simple. This extra band occurs because of the introduction of some triply coordinated bonding rather than the simple donor-acceptor bonding in the fully cyclic isomer.

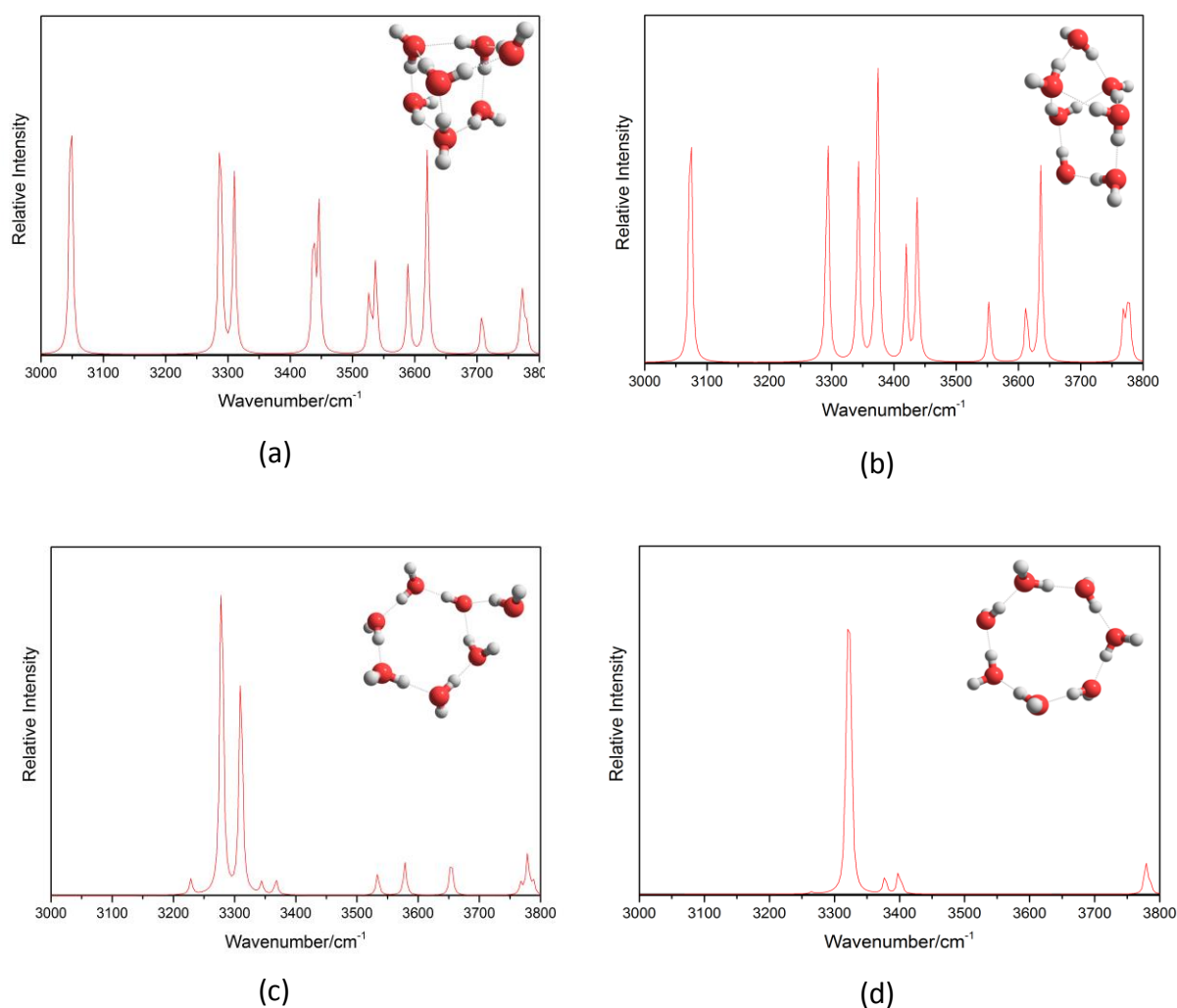


**Figure 3.2.** Calculated (MP2/aug-cc-pVDZ ) water heptamer structures. (a) Prism, (b) chair, (c) bicyclic structure and (d) fully cyclic isomers. Also shown are IR spectra predicted from a harmonic oscillator model.

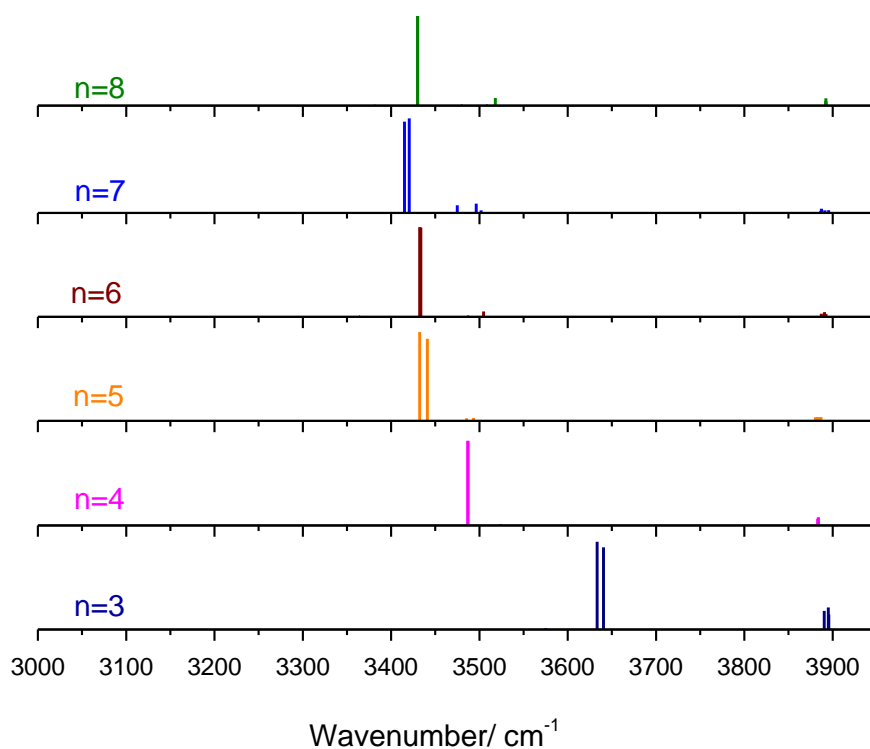


**Figure 3.3.** Calculated IR spectra (harmonic approximation) of the cyclic water clusters  $(\text{H}_2\text{O})_n$  ( $n = 3 - 8$ ) using the MP2 level of theory, and scaling factor was not used in this calculations.

Anharmonic calculations were also obtained for cyclic water clusters (Figure 3.4). As mentioned earlier, these were performed by Yimin Wang and Joel Bowman at Emory University in Atlanta and kindly sent through to us. The anharmonic calculations predict a progressive red shift in the bonding OH band from water trimer to water hexamer, and then a small shift back to the blue for the heptamer and larger water clusters. This is similar to but not identical with the harmonic predictions.

A significant difference between the harmonic (Figure 3.3) and anharmonic calculations (Figure 3.4) is that the position of the free OH band spanned a range of about  $20 \text{ cm}^{-1}$  for different water clusters in the anharmonic case while it is virtually the same for all clusters in the harmonic calculations (Figure 3.3).

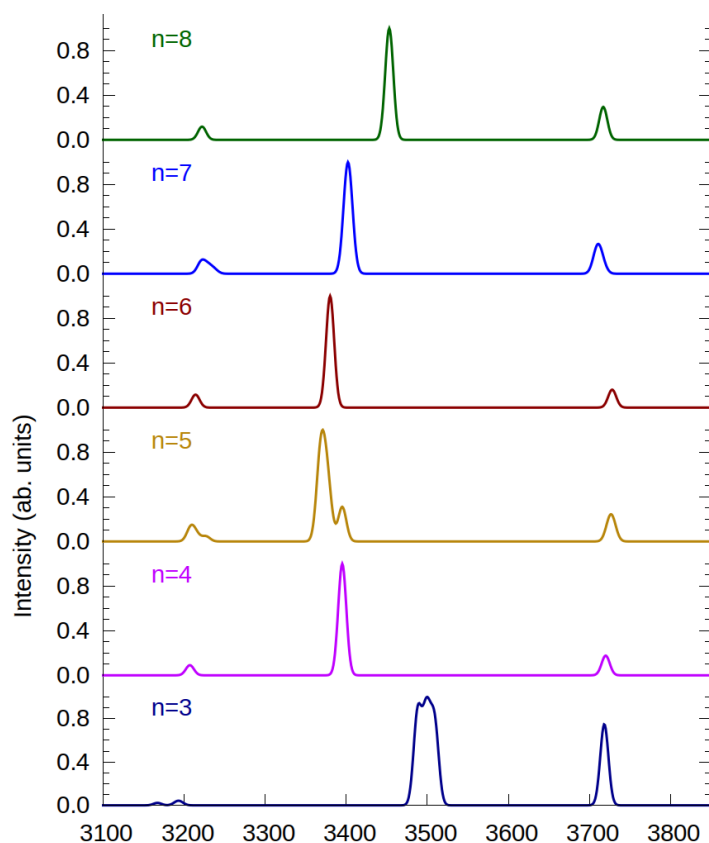
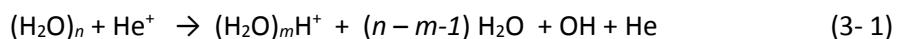


**Figure 3.4.** Calculation of the IR spectra of cyclic water clusters using an anharmonic model.

For the anharmonic calculations, overtone transitions were also predicted. An overtone of the water bending vibration is predicted in the anharmonic spectrum at  $3220\text{ cm}^{-1}$  (Figure 3. 4). This band is significantly broader for the water heptamer,  $(\text{H}_2\text{O})_7$ , than for  $(\text{H}_2\text{O})_6$  and  $(\text{H}_2\text{O})_8$ . This presumably arises because the heptamer has a lower symmetry than the other two clusters. Since harmonic oscillator calculations cannot predict overtone transitions, therefore, there is not any overtone band of OH bending in the harmonic calculations for cyclic water clusters (Figure 3.3).

### 3.4.2 Mass Spectrum

As the aim of the present work is to record IR depletion spectra of water clusters, it is first necessary to record mass spectra. Mass spectra were obtained via electron ionization of water-doped HeDs. The ionization of water clusters presumably occurs by indirect ionization of HeDs. A helium atom within the droplet is ionized and then transfers the charge to the water cluster via charge hopping, i.e.



An illustrative mass spectrum which covers the range from  $m/z$  8 to 200  $m/z$ , as shown in Figure 3.5. This spectrum is recorded at nozzle temperature of 16 K and helium pressure of 33 bar. In the present work, low amount of water is added to HeDs. By adding a small amount of water vapour the contribution from large water clusters is kept to a minimum.

The spectrum (Figure 3.5) shows a progressive decline in the  $(\text{H}_2\text{O})_m\text{H}^+$  signal as a function of  $m$ . Note, however, that we cannot associate a specific ion with a particular neutral water cluster. As can be seen from reaction (3-1), fragmentation of the water cluster ions following the ionization event is expected and the branching ratios of the various fragmentation channels may vary strongly with cluster size.

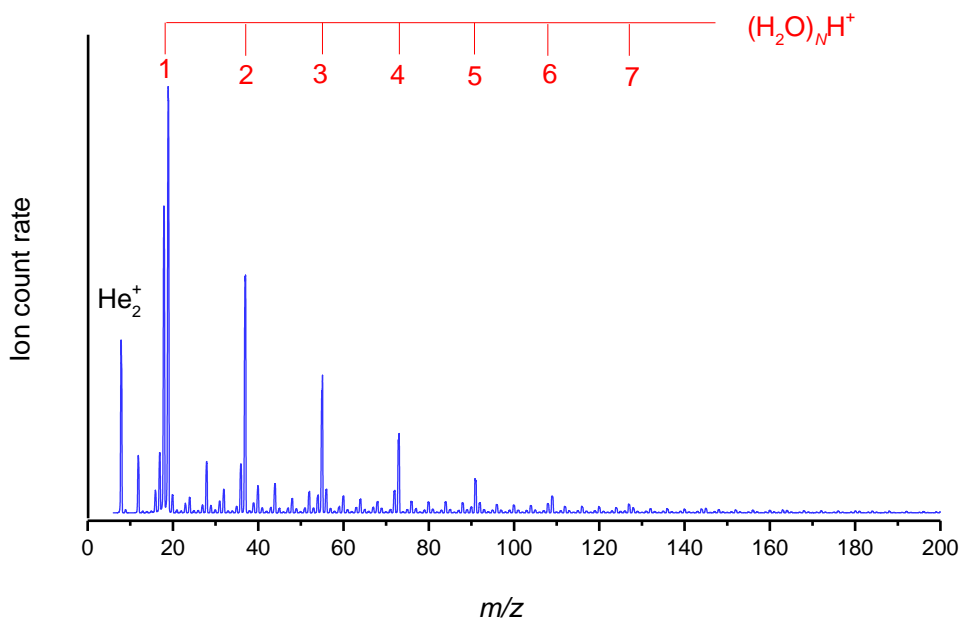


**Figure 3.5.** Mass spectrum for water clusters in HeDs recorded at a nozzle temperature of 16 K and helium pressure of 33 bar.

### 3.4.3 IR Spectroscopy of small water clusters $(\text{H}_2\text{O})_n$ ( $n = 2-6$ )

The experimental aim was to record new water cluster spectra larger than the water hexamer. However, to set the scene we first record the IR spectra of small water clusters and discuss those in this section. Figure 3.6 shows the IR spectrum recorded under conditions where the water vapour pressure in the pickup cell was relatively low. This spectrum focuses on the OH stretching region in the range  $3000 - 3800 \text{ cm}^{-1}$  and was obtained by monitoring the ion signal at  $m/z = 19$ , which corresponds to  $(\text{H}_2\text{O})\text{H}^+$ . By monitoring the signal for this ion, contributions to the IR spectrum from the water monomer are automatically removed (since  $(\text{H}_2\text{O})\text{H}^+$  cannot be formed by ionization of a single  $\text{H}_2\text{O}$  molecule). The IR spectrum in Figure 3.6 is in agreement with previous experimental studies of small water clusters in HeDs [101,107]. The peak at  $3592 \text{ cm}^{-1}$  belongs to the bonded OH stretch of  $(\text{H}_2\text{O})_2$  while the peak at  $3717 \text{ cm}^{-1}$  is from free O–H bond of all water clusters. The bonded OH bands of the trimer, tetramer and pentamer bands are located at  $3529$ ,  $3394$  and  $3354 \text{ cm}^{-1}$ , respectively.

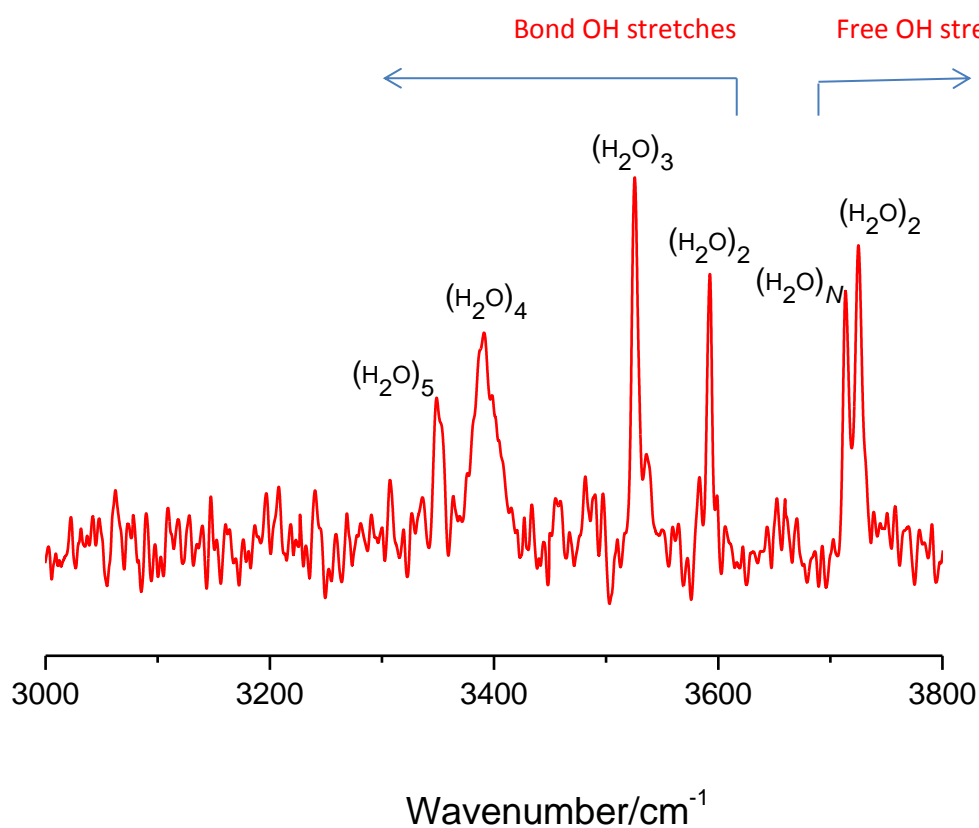


**Figure 3.6.** IR spectrum recorded by monitoring ion depletion at  $m/z$  19.

Mass selection can aid the assignment of specific IR bands. For example, by recording the IR spectrum while collecting signal for  $(\text{H}_2\text{O})_2\text{H}^+$  ( $m/z = 37$ ), only  $(\text{H}_2\text{O})_3$  and larger clusters can contribute. This approach can be used successively to strip away contributions from smaller water clusters and is employed in the next section.

#### **3.4.4 Infrared Spectroscopy of Water Clusters $(\text{H}_2\text{O})_n$ ( $n = 7-9$ )**

Attempts were made to record IR spectra of larger water clusters ( $(\text{H}_2\text{O})_n$  for  $n = 6, 7, 8$  and 9) using the mass-selective approach described previously to strip away the contributions from smaller clusters. The lowest possible vapour pressure of water was added to the HeDs while keeping a reasonable signal/noise ratio. The reason for doing this was to try to avoid, as much as possible, the formation of excessively large water clusters. If such clusters form, their IR signal could potentially overwhelm that of the

smaller (desired) water clusters. Of course this control of pressure can only take one so far, since if one is looking for the spectrum of, say, the water octamer then there are bound to be some contributions from the nonamer and larger clusters because the pickup process is statistical. In the results that follow IR spectra of  $(\text{H}_2\text{O})_6$  and  $(\text{H}_2\text{O})_7$  were recorded at water partial pressures of  $4.68 \times 10^{-6}$  mbar while for  $(\text{H}_2\text{O})_8$  and  $(\text{H}_2\text{O})_9$  the pressure was raised to  $5.15 \times 10^{-6}$  mbar.

The IR spectrum in the lowest panel in Figure 3.7 was recorded at  $m/z$  91, which corresponds to  $(\text{H}_2\text{O})_5\text{H}^+$ . Detection using this ion precludes any contribution from the water pentamer and smaller clusters and so any IR bands must come from the hexamer and larger water clusters. A red dashed line shows the position of the band at  $3346 \text{ cm}^{-1}$  which belongs to  $(\text{H}_2\text{O})_6$  since this peak disappears at higher mass channel. However, the cyclic water hexamer was observed in previous study at  $3335 \text{ cm}^{-1}$  by Nauta and Miller [101]. Here we are taking in account that it could be some error that causes the difference of  $11 \text{ cm}^{-1}$  between our experimental observation of hexamer water cluster and that of the previous study [101]. A peak at  $3226 \text{ cm}^{-1}$  in our experiment is in agreement with previous study [101] and was thought to be from the cage isomer of the water hexamer [104] but a later assignment suggests that it is a bending overtone of the cyclic water hexamer [102]. As we observed the cyclic water hexamer and overtone band, our findings in the OH stretching region for  $m/z$  91 is broadly in agreement with that by Nauta and Miler [101]. The peak at  $3717 \text{ cm}^{-1}$  in the same trace is the free OH stretching band from various water clusters. There is also a broad absorption from  $3100$  to  $3700 \text{ cm}^{-1}$  which includes many small peaks, such as one at  $3450 \text{ cm}^{-1}$ . These features are also seen for larger water clusters and are therefore assigned to these larger clusters.

When the mass channel switches to  $m/z$  109 ( $(\text{H}_2\text{O})_6\text{H}^+$ ) the IR spectrum changes. Here, the spectrum can only arise from the water heptamer  $(\text{H}_2\text{O})_7$  and larger clusters, *i.e.* the contribution from the hexamer has been removed by the mass selection. A new peak at  $3320 \text{ cm}^{-1}$  is observed, which is shifted to the red of the cyclic water hexamer in the previously discussed spectrum. This new peak is consistent with the OH stretching band of the water heptamer since it disappears when the mass channel is switched from  $m/z$  109 to  $m/z$  127 ( $(\text{H}_2\text{O})_7\text{H}^+$ ). Previous experimental work

in the gas phase gave a cage structure as the most stable isomer [86], while theoretical studies predict a prism structure [76,92,94,95] as the global minimum energy structure of water heptamer. However, the current study does not show the absorption bands below  $3200\text{ cm}^{-1}$  expected of non-cyclic structures. Consequently, we conclude that we are producing cyclic water heptamer in our HeDs experiments.

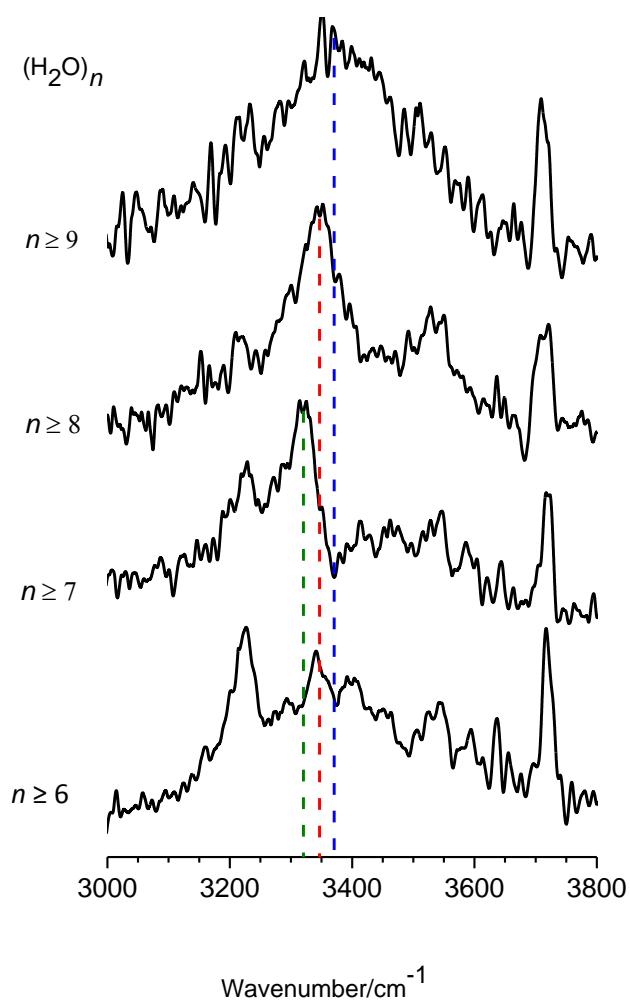


**Figure 3.7.** IR spectra of water clusters recorded in mass channels of 91, 109, 127 and 145  $m/z$  from the bottom to the top. The dashed lines show positions of the bonded OH stretch maxima for each  $m/z$ , except the same colour is used for  $m/z$  91 and 127 because their maxima are at almost identical positions. The sharp peak at  $3717\text{ cm}^{-1}$  (present in all the spectra above) is the free OH stretching band from various water clusters.

There is no evidence that water heptamer forms prism or chair structures in HeDs, since such structures should have signals of bonded OH at lower frequencies at  $\ll 3300 \text{ cm}^{-1}$ , as shown in the simulations in Figure 3.2 (a) and (b). The calculations suggest that the bicyclic structure of the heptamer has two strong and distinct bands near  $3300 \text{ cm}^{-1}$  (Figure 3.2(c)), which again are absent in the experimental IR spectrum. Therefore, the bonded OH stretching band at  $3320 \text{ cm}^{-1}$  is assigned to the cyclic isomer (see green dashed line in Figure 3.7).

Our *ab initio* calculations at the MP2/aug-ccpVDZ level showed a red shift of the bonded OH stretch from water hexamer to the heptamer of  $12 \text{ cm}^{-1}$  (Figure 3.3). The experimental shift from OH bond from  $(\text{H}_2\text{O})_6$  to  $(\text{H}_2\text{O})_7$  value is  $25 \text{ cm}^{-1}$  (Figure 3.7). The previous experimental study by Miller group [104] showed that the peak at  $3321 \text{ cm}^{-1}$  is  $14 \text{ cm}^{-1}$  red shift to the cyclic water hexamer.

In the anharmonic calculations, the bonded OH stretching band of the water heptamer is predicted to be at  $\sim 3405 \text{ cm}^{-1}$ . In addition, the anharmonic calculations (Figure 3.4) predict a red shift from of the bonded OH stretching bands in moving from water trimer to the pentamer but then a blue shift in moving to the hexamer. On the other hand, there is blue shift in bonded OH stretching from spectrum at  $m/z$  of 109 to the higher spectra in both the experimental and the scaled harmonic approximation calculations. There is a disagreement between the calculated anharmonic and heptamer band positions, the difference being  $16 \text{ cm}^{-1}$ . The same is also true for the bonded OH stretching of water hexamer, where the anharmonic calculations predict a band at  $3390 \text{ cm}^{-1}$  while it was observed at  $3335 \text{ cm}^{-1}$  by Nauta and Miller and at  $3346 \text{ cm}^{-1}$  in the present work. Thus we know that the anharmonic calculations are not able to predict the band positions particularly accurately.

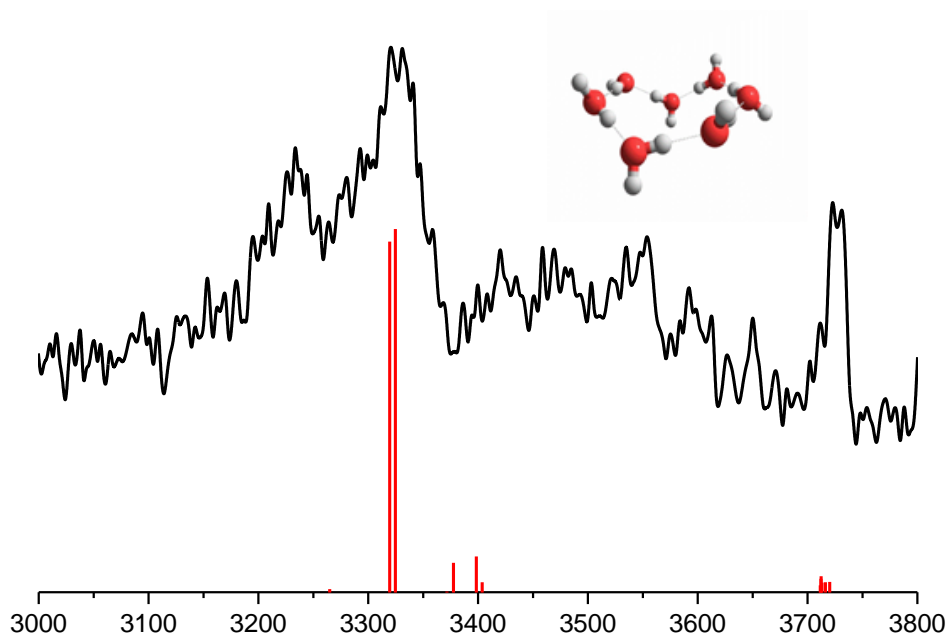


**Figure 3.8.** Experimental spectrum of water clusters with  $n \geq 7$  (previously shown as second bottom spectrum in Fig 3.7). The red lines are predictions from *ab initio* calculations for the fully cyclic heptamer isomer, however the theoretical frequencies of the current figure are scaled using scaling factors of 0.955 for the free OH stretch and 0.972 for the OH hydrogen-bonded stretches. The observed spectra (and all other observed spectra in the current work) are not normalized to any variation of the laser intensity since the pulse energy only varied from 8 mJ to 12 mJ in all experiments of the current work

There is additional evidence for the assignment of the strongest band in Figure 3.8 to the cyclic water heptamer, namely the width of the free OH peak of the water heptamer at  $3721 \text{ cm}^{-1}$  in  $m/z$  of 109 ( $(\text{H}_2\text{O})_6\text{H}^+$ ). This width of the free OH is same as that of the lower trace of  $(\text{H}_2\text{O})_5\text{H}^+$  in Figure 3.7. The width of the free OH at  $m/z$  109 can be explained as a single band arising since there is essentially only a single type of free OH stretching environment. The position of the free OH in all our experimental spectra is at  $3721 \text{ cm}^{-1}$ , as shown in Figure (3.7), which is in agreement with the scaled harmonic calculations. However, the theoretical anharmonic calculations predicted some differences in the frequency of the free OH for different water clusters size although the size of the cluster has no influence on the frequency of the dangling OH.

Since this difference is about  $20 \text{ cm}^{-1}$ , therefore, it could relate to the error in the anharmonic calculations since it be expected the uncertainty is about  $20 \text{ cm}^{-1}$ .

Spectra of the heptamer and larger water clusters in HeDs have not previously been reported. Previous experimental work of observing cyclic water hexamer in HeDs [104] by Miller's group expected that the heptamer water spectrum was covered via spectrum from higher water clusters [104].

The IR spectrum recorded at  $m/z$  127 ( $(\text{H}_2\text{O})_7\text{H}^+$ ) has its strongest band intensity at  $3344 \text{ cm}^{-1}$  and this peak maximum is shifted to the blue of that for  $m/z$  109 ( $(\text{H}_2\text{O})_6\text{H}^+$ ), as shown by the dashed red line in Figure 3.7. This peak disappeared when the mass channel was switched to  $m/z$  145, and instead a new peak appeared at about  $3368 \text{ cm}^{-1}$ , as shown by the dashed blue line in Figure 3.7. It therefore seems likely that the peak at  $3344 \text{ cm}^{-1}$  derives from the water octamer,  $(\text{H}_2\text{O})_8$ . The spectrum recorded at  $m/z$  127 has a small band at  $3530 \text{ cm}^{-1}$  which appears at all previous mass channels, which implies it comes from even larger water clusters.

Theoretical calculation of harmonic oscillator at MP2/aug-cc-pVDZ predicted cyclic water octamer that is in excellent agreement with the observed OH stretching of the water octamer at  $m/z$  of 145 (Figure 3.9). Anharmonic calculations predict a separation of about  $50 \text{ cm}^{-1}$  between the  $n = 7$  and  $n = 8$  peaks which is very similar to what we see in the experiment.

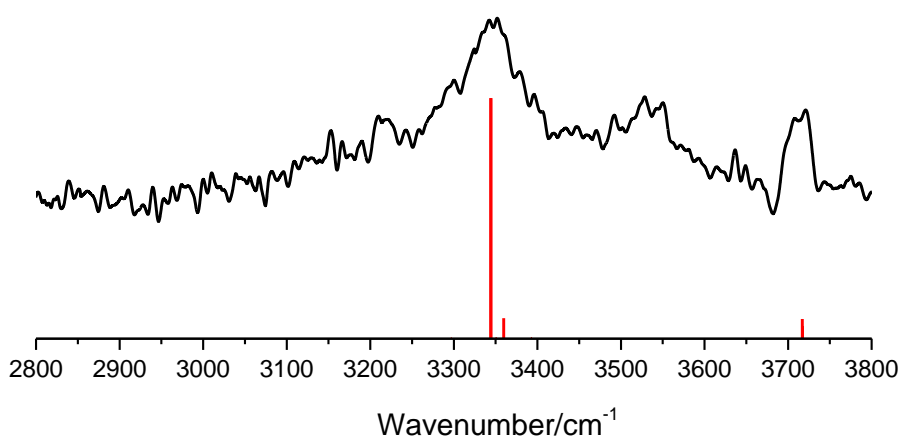


**Figure 3.9.** IR spectrum recorded at  $m/z = 127$  ( $(\text{H}_2\text{O})_7\text{H}^+$ ) (same as showed in Figure 3.7, second spectrum from the top). The nozzle temperature was 16 K, the helium pressure was 33 bar and the water vapour pressure in the pickup cell was  $5.15 \times 10^{-6}$  mbar. Also shown is the MP2/ aug-cc-pVDZ harmonic prediction (in red), which is showed also in Figure 3.3 but before adding scal factor. The calculated vibrational frequencies were scaled using scaling factors of 0.955 for the free OH stretch and 0.972 for the OH hydrogen-bonded stretches.

It is not possible to expect formation of non-cyclic octamer water isomer in HeDs in our experimental spectra. The theoretical calculations predicted the minimum energy of the octamer as a cubic structure at MP2 level of *ab initio* calculations, which is in agreement with the experimental studies of  $(\text{H}_2\text{O})_8$  in the gas phase [108], as shown in Figure 3.10. Cubic octamer water structure has shown bonded OH signals in the range  $3000 - 3100 \text{ cm}^{-1}$  in both the experimental and theoretical results. Therefore, more than one peak (close to those in Figure 3.10) would be observed if the cubic structure was present in the present work. However, there is no evidence for the cubic structure in HeDs since a single clear peak at  $3350 \text{ cm}^{-1}$  is observed in the present work. This peak is absent in both theory and previous experimental spectra of the water octamer structure as shown in Figure 3.10.

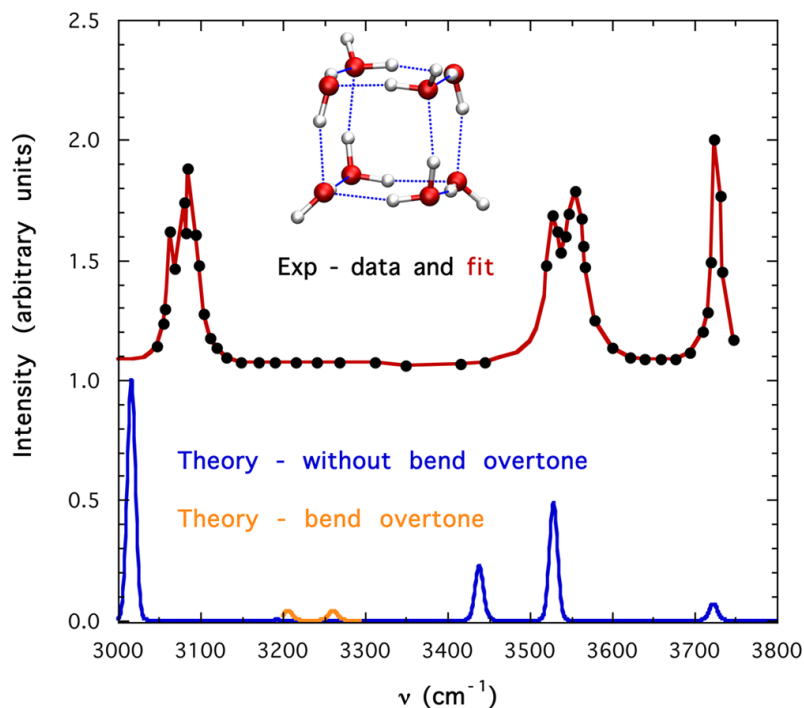


**Figure 3.10** . Theoretical (blue) and experimental IR spectra of the cubic water octamer in the gas phase (red colour). Reprinted from reference [102].

The IR spectrum recorded at  $m/z$  of 145 in the present work must come from neutral water clusters with  $n \geq 9$ . The OH region showed maximum intensity of bonded OH stretching at approximately  $3368 \text{ cm}^{-1}$  (blue dashed line), as shown in Figure 3.7. The signal is shifted to the blue of the bonded OH peak of the octamer water, so this peak is therefore tentatively assigned to the water nonamer. The free OH region showed a sharp peak similar to those appearing in spectra at lower mass channels. The scaled harmonic calculations failed to predict a cyclic nonomer structure at the MP2 level. Instead, a bi-cyclic isomer formed. More work (experimentally and theoretically) is required to prove formation of a cyclic water nonomer in HeDs.

Finally, the experimental bonded OH band positions are compared with the scaled harmonic predictions for the trimer through to the octamer in Figure 3.11. The red shift from the trimer to hexamer is already established but the scaled harmonic

prediction is for a further, small, red shift for the heptamer. Our experimental observation is consistent with this. Also consistent is the small blue shift we see for the peak assigned to the octamer. This blue shift is attributed to increasing hydrogen-bonding strain in the cluster in going from the heptamer to the octamer.

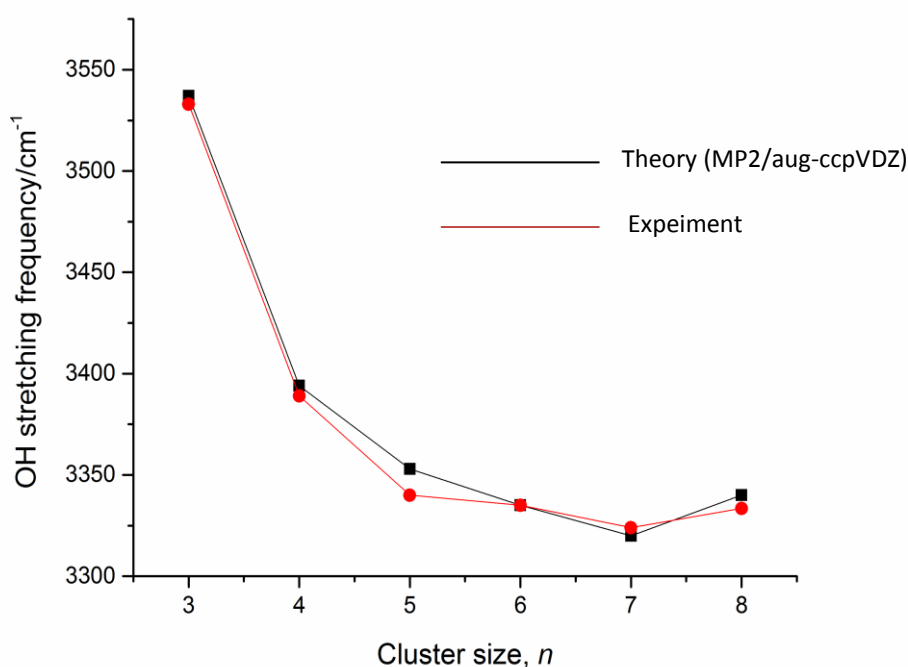


**Figure 3.11.** Comparison of the experimental and theoretical (MP2/aug-cc-pVDZ; scaled harmonic approximation) positions of the bonded OH stretching bands of cyclic water clusters from  $(\text{H}_2\text{O})_3$  to  $(\text{H}_2\text{O})_8$ .

The difference between hexamer and heptamer water clusters' structures found in prior experiments (and calculations) performed in the gas phase versus these experiments in HeDs is due to the very low temperature of HeDs (0.37 K). This cool environment trapped the water clusters in local energy minima (2-dimensional molecular structures, i.e. cyclic) instead of the global energy minimum (three dimensional structures, i.e. cages).

### 3.5 Conclusions

In this work, evidence for the formation of cyclic structures has been reported for the heptamer and octamer. This evidence derives from mass-selective IR spectra of water clusters in HeDs. IR spectrum at  $m/z$  of 109 ( $(\text{H}_2\text{O})_6\text{H}^+$ ) shows signal of water heptamer at  $3321\text{ cm}^{-1}$  and the theoretical calculations predicted a cyclic structure for this signal. This peak shifted to blue at a higher mass channel at  $m/z$  of 127 ( $(\text{H}_2\text{O})_7\text{H}^+$ ). The highest bonded OH stretching observed at  $3344\text{ cm}^{-1}$  at mass channel of  $(\text{H}_2\text{O})_7\text{H}^+$  and again this peak shifted blue at  $m/z$  of 145 ( $(\text{H}_2\text{O})_8\text{H}^+$ ). Harmonic scaled and anharmonic calculations predicted cyclic water octamer of the peak at  $3344\text{ cm}^{-1}$ .

## Chapter 4

### *Larger water clusters (H<sub>2</sub>O)<sub>n</sub> (n = 10 – 21)*

#### 4.1 Introduction

Multiple hydrogen bonds in water clusters are of broad interest because of the potential relevance to the operation of a collection of such bonds in bulk water and ice. However, they also represent a finite system and can therefore be modelled more easily than the bulk systems. For this reason there has been considerable interest in large water clusters and these have been studied theoretically and experimentally [109-140].

*Ab initio* calculations are, in principle, possible for water clusters containing even up to dozens of water molecules, although approximations will inevitably be needed for such large systems. For example, the polarizability of (H<sub>2</sub>O)<sub>n</sub> (n = 2 – 20) has been studied using Hartree-Fock calculations in combination with a 6-311++G (d, p) basis set, and it was predicted that the polarizability of the water clusters rises with increasing size of the cluster [114]. Fanourgakis *et al.* studied the binding energy of four minimum energy structures of (H<sub>2</sub>O)<sub>20</sub> using MP2 calculations: dodecahedron, edge-sharing pentagonal prisms, fused cubes and face-sharing pentagonal prisms [115]. They found that the minimum energy of these isomers is independent on the number of H-bonds in the isomers [115]. Julius *et al.* used hybrid density functional (X3LYP) theory with aug-cc-PVTZ basis sets to obtain accurate minimum energies of water clusters up to (H<sub>2</sub>O)<sub>19</sub> [116]. They compared their results with MP2 theory with the same basis set and corrected for the basis set superposition error (BSSE). It was found that the X3LYP approach was the most useful in terms of both accuracy and speed to predict the structures and energies of (H<sub>2</sub>O)<sub>n</sub> isomers [116]. Fanourgakis *et al.* expanded their previous theoretical study [115] to calculate the harmonic vibrations for the four common isomers of (H<sub>2</sub>O)<sub>20</sub> [118]. They predicted that the dodecahedron isomer has a high number of IR active bands while the pentagonal prism structure has the highest intensity OH absorption [118]. Infrared spectra of (H<sub>2</sub>O)<sub>9-21</sub> have also been predicted at the DFT/B3LYP level [119]. This study explained that shifts in the OH

stretching spectra depend on the number of donor/accepter hydrogen bonds and also depends on the other hydrogen bonds of molecules which are around the two main molecules of the hydrogen bond [119]. The hydrogen-bond that suffers the largest red-shift occurs from a single-donor 3 -coordinated molecule and a single acceptor isomer [119].

Some experimental studies of IR spectra of large water clusters in the OH stretching region have been reported. To make sense of these spectra it is helpful to be able to make spectral assignments as a function of cluster size. This requires mass selectivity or some other technique that can provide some degree of size discrimination. IR spectra of charged water clusters are particularly convenient for this approach, since specific ions can be pre-selected by mass spectrometry. The OH stretching spectra of protonated water clusters,  $H^+(H_2O)_n$ , in the range of  $n = 2 - 28$  in the gas phase at a temperature of  $\sim 10$  K have been recorded and the spectra are consistent with three-dimensional structures for  $n \geq 10$  [137].

For large uncharged water clusters size selectivity is much more of a challenge, especially given that any technique that uses ionization for detection is likely to lead to ion fragmentation [110]. One solution has been used is to attach a chromophore to a water cluster and then the attached chromophore is ionized at its threshold ionization energy [111,120]. For example, benzene was used to tag small water clusters  $(H_2O)_{1-7}$  and thereby record their IR spectra mass-selectively, since benzene can be ionized by resonance-enhanced multiphoton ionization (REMPI) [141]. This idea has been extended to larger water clusters through the use of phenol as the chromophore and this has provided IR spectra for  $10 < n \leq 50$  [122,123] and even up to hundreds of water molecules [128]. The resulting spectra showed that the free OH stretch of large water clusters is shifted to the red with increasing water cluster size starting from  $(H_2O)_{10}$ . Theory has explained this in terms of a decrease in the strain of hydrogen bonds with an increase in the water cluster size [122]. However, one must always bear in mind that the use of a tag may actually affect the structure of the underlying molecular cluster.

Another tag that has been used is the Na atom. Buck co-workers used Na atoms attached to water clusters since the photoionization energy of Na is much lower than

water. Consequently, Na can be ionized with little effect on the water clusters [114,120,121,127,135]. By using Na as the tag, IR spectra were recorded mass selectively by enhanced photoionization probability of the Na-water clusters [127,135]. Here, the UV wavelength, with less energy than the threshold energy of photoionization Na-water cluster, was applied to photoionize the excited Na-water clusters which are excited via IR radiation [120,127]. This technique has been used to record IR spectra across a wide range of cluster sizes, from small to large. One of the most interesting findings was a change from amorphous to crystalline structures at sizes for  $\geq 275 \pm 25$  [127]. Later, Buck *et al.* compared the experimental spectra in the OH stretching region of  $\text{Na}(\text{H}_2\text{O})_n$  for  $n = 8, 10, 16$  and  $20$  with theoretical predictions [121]. They concluded that the observed signals between  $3430$  and  $3550 \text{ cm}^{-1}$  were generated from interaction between hydrogen atoms of OH groups with solvated electrons [121]. IR spectra of  $(\text{H}_2\text{O})_{20}$  were obtained via tagging water with Na atoms at a temperature of  $373 \text{ K}$  by Pradzynski *et al.* using IR excitation and photoionization spectroscopy [114]. Their observations of spectra in the OH stretching region was in agreement with a theoretical prediction of two isomers of  $(\text{H}_2\text{O})_{20}$  which are an edge-sharing pentagonal structure and a drop-like structure with a fully coordinated and interconnected water molecule [114].

In the present work, IR spectra of large water clusters  $(\text{H}_2\text{O})_n$  are reported in HeDs for the first time. The approach used is similar to that described in Chapter 3 but uses larger masses for detection and higher water partial pressures. The spectra have been compared with those of liquid water and ice and show some agreement.

## 4.2 Experimental details

The experimental setup has been described in Chapter 2 and the procedure used is very similar to that described in Chapter 3, except that a higher water pickup cell pressure of  $1.01 \times 10^{-6} \text{ mbar}$  is used and depletion spectra were recorded by detecting larger  $(\text{H}_2\text{O})_n\text{H}^+$  ions. Often in this thesis only qualitative information can be provided about the dopant concentrations used (e.g. spectrum A was obtained at higher water pressure than spectrum B) because, at the time these data were acquired, the HeD apparatus didn't have the capacity to monitor dopant concentrations. However, the

new version of the apparatus now has pressure gauges to record the concentration of the dopant in each of the pickup chambers, so experimental conditions can now be controlled and reproduced quantitatively. For this reason, the account given here is deliberately brief. Helium is pressurised at stagnation pressure of 34 bar and then passes to the vacuum system through a cooled nozzle at temperature of 15 to 14 K.

Mass spectra were recorded before recording IR spectra in order to gain some idea about the likely sizes of the water clusters (although ion fragmentation makes this difficult to judge precisely). The mass spectrum in Figure 4.1 shows a much broader  $(\text{H}_2\text{O})_n\text{H}^+$  distribution than that shown in Chapter 3. Indeed there is a signal maximum at  $m/z$  73 ( $(\text{H}_2\text{O})_4\text{H}^+$ ) before the signal declines gradually with an increasing number of water molecules.

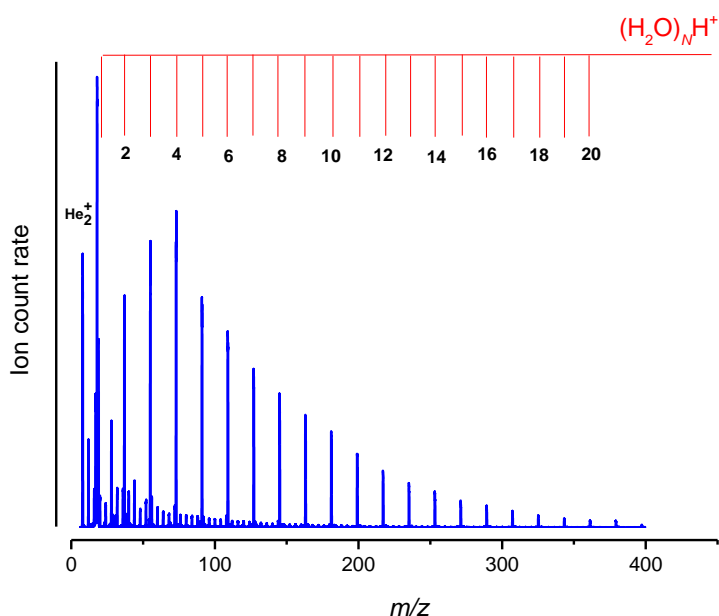


**Figure 4.1.** Mass spectrum obtained from water clusters in helium droplets in the range  $m/z$  8 – 400.

## 4.3 Results and discussion

### 4.3.1 Infra-red spectroscopy of $(\text{H}_2\text{O})_n$ ( $n = 10 - 21$ )

IR spectra of large water clusters of  $(\text{H}_2\text{O})_n$  were recorded in HeDs in the range 3000-3800  $\text{cm}^{-1}$ . The heaviest ion mass considered was  $m/z = 361$ , which corresponds to

$(\text{H}_2\text{O})_{20}\text{H}^+$ . For reasons already discussed in Chapter 3, this ion can only be created from  $(\text{H}_2\text{O})_{21}$  and larger water clusters.

Some examples of spectra for larger water clusters are shown in Figure 4.2. There are two main features in these spectra. First, there is a relatively weak free OH stretching absorption near  $3700\text{ cm}^{-1}$ . For large water clusters this is expected to arise from water molecules at the surface of the cluster with dangling OH bonds. Further discussion of this absorption will be provided later. The second and more obvious feature is the very broad absorption which extends across the range  $3000\text{--}3650\text{ cm}^{-1}$ . This broad absorption, which arises from those OH groups involved in hydrogen bonding, seems to have some structure.

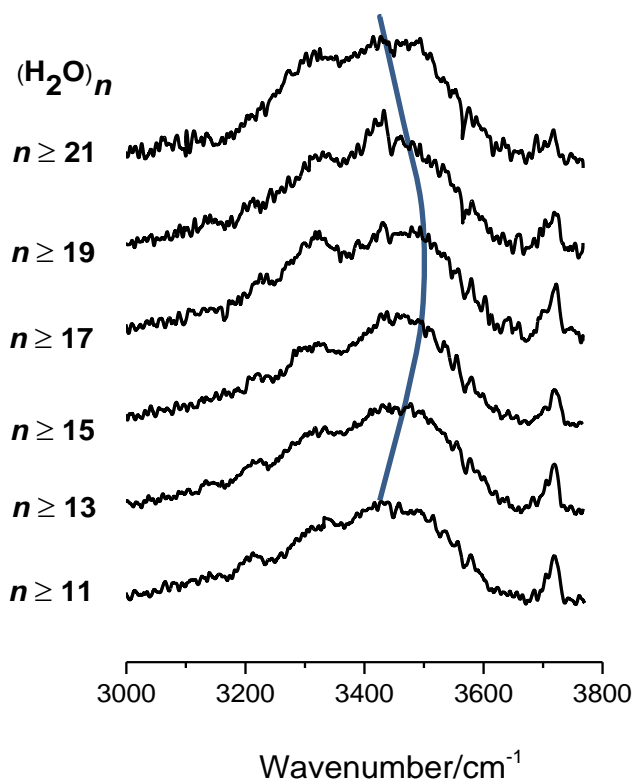


**Figure 4.2.** IR spectrum of large water clusters  $(\text{H}_2\text{O})_n$ . This was recorded by monitoring  $(\text{H}_2\text{O})_N\text{H}^+$  ions, and hence must come from neutral  $(\text{H}_2\text{O})_n$  clusters with  $n \geq N + 1$ . Each spectrum is an average of four separately recorded spectra, each recorded under the same experimental conditions. The blue line is a guide to the eye and shows the estimated maximum of the most intense of the bonded OH feature.

In comparison between Figure 3.7 for small water clusters ( $n = 6$  to  $9$ ) and Figure 4.2 of large water clusters ( $n = 11$  to  $21$ ), the trend in the size depended frequency shifts to blue from  $n = 7$  to  $n = 9$  (Figure 3.7). This blue shift is also observed in Figure 4.2 from  $n = 11$  to  $n = 17$ . Thus the blue shift is continuous from  $n = 7$  to  $n = 17$ .

#### **4.3.2 Hydrogen-bonded OH region**

As mentioned above there is clear evidence of reproducible structure in the bonded OH stretching region in Figure 4.2. However, the underlying absorption features are broad and are not fully resolved. The discussion here will focus on the most intense frequency component, the position of which is illustrated by the blue line in Figure 4.2. The maximum for this peak seems to shift to the blue initially as the mass of the detected ion (and therefore presumably the mean size of the contributing neutral water cluster) increases. For the spectra from the largest ions in Figure 4.2 there is some uncertainty about where the maximum is, and indeed there may even be additional structure for these larger species which causes confusion. Thus, while the blue line shows the maximum shifting back to the red, this must be regarded as tentative.

For the lowest spectrum in Figure 4.2, which arises from  $(\text{H}_2\text{O})_n$  clusters with  $n \geq 11$ , the peak maximum is at  $\sim 3420 \text{ cm}^{-1}$ . The shift to the blue for larger clusters suggests that the hydrogen bonds become marginally weaker as the cluster size initially increases. There is a second peak at *ca.*  $3320 \text{ cm}^{-1}$  in all spectra, and this becomes marginally more prominent for the larger clusters, suggesting it is associated with the largest water clusters. A small peak at  $3220 \text{ cm}^{-1}$ , which is particularly noticeable in the spectra at smaller ion masses, is in the same position as the water bending overtone band described previously in Chapter 3.

### **4.3.3 Free OH region**

The free OH stretching vibration derives from those OH bonds that are not contributing to hydrogen bonds [68,142]. Molecules within water clusters can be classified as single acceptor (A), double acceptor (AA), single donor (D), double donor (DD), double acceptor-single donor (AAD), double donor-single acceptor (DDA) and double donor-double acceptor (DDAA) [142]. These classifications indicate how many hydrogen bonds each water molecule makes with surrounding water molecules and how many such bonds it receives. Take, for example, the water octamer (see Figure 4.3), which might exist as a ring structure where all molecules are of the single donor–single acceptor (AD) variety. On the other hand, a cubic isomer is possible where the water molecules are either in the double acceptor-single donor (AAD) form or are single acceptor-double donor (ADD) molecules (Figure 4.3) [142]. Each of the water molecules in the cyclic isomer has a free OH whereas in the cubic isomer only the AAD water molecules have free OH bonds.

*Ab initio* calculations predict that water clusters larger than the pentamer are arranged in their lowest energy minimum as three dimensional structures [77,79] while for a cluster size of a few tens of water molecules half of all water molecules are ADD and AAD [143].

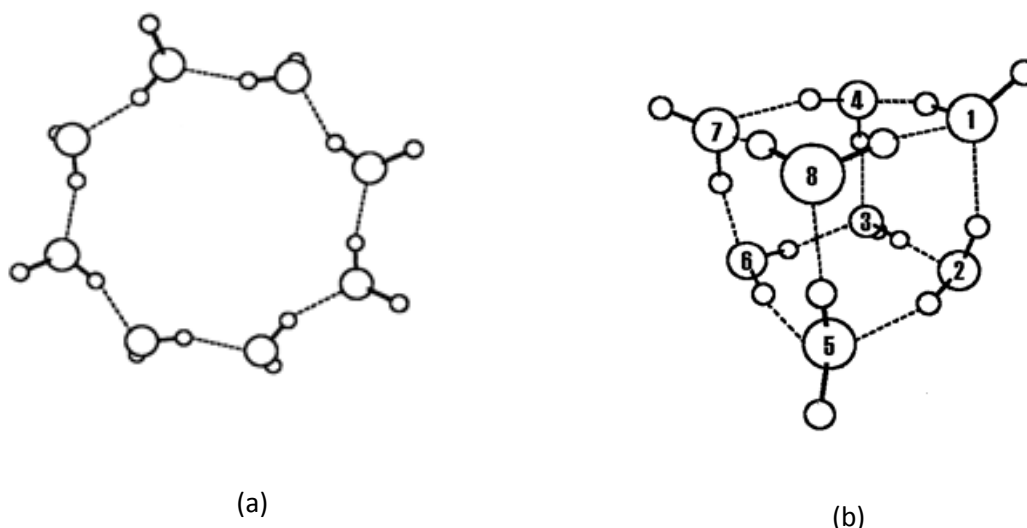


**Figure 4.3.** Calculated structures of  $(\text{H}_2\text{O})_8$  cluster taken from reference [142]. (a) Ring structure, all water molecules are involved in DDA binding. (b) 'Cubic' octamer in which water molecules with dangling OH bands are involved in AAD binding (molecules 1, 3, 5 and 7) while the others have DDA binding.

Studies have shown that water clusters with 3-coordinated molecules have lower frequency free OH stretching bands than those of 2-coordinated (AD) molecules [142,144]. The first of these studies was by Buch and Devlin, who observed the free OH stretches for different size of water clusters of 2- and 3- coordinate water molecules at  $3720$  and  $3696\text{ cm}^{-1}$ , respectively [144]. The free OH of 3- coordinated molecules is close to that of the two-coordinate water molecules, which makes assignment of the free OH band to a specific type of coordination challenging [142]. In addition, it was found that the position of the free OH band of 3-coordinated molecules depends on the orientations of the molecules in the water structure [142]. The free OH absorption was recorded at  $3719\text{ cm}^{-1}$  for water clusters  $(\text{H}_2\text{O})_n$  in HeDs with  $n = 3-8$ .

In the present work, there is a clear signal in the free OH stretching region in all water cluster spectra (Figure 4.2). This band is much sharper and has a much lower intensity than the bonded OH bands at lower wavenumbers. The free OH peak intensity decreases with the water cluster size relative to the bonded OH features. The likely explanation is that the number of 2-coordinated water molecules decreases as the cluster size increases, whereas the opposite is true for 3-coordinated molecules.

The free OH band is itself structured, with a strong feature at high frequency at  $3719\text{ cm}^{-1}$  and a weaker peak at lower frequency at  $3704\text{ cm}^{-1}$ , as shown in Figure 4.4. These two peaks prove that there are at least two different environments of water molecules in the clusters grown in HeDs. These findings in the free OH stretching region are different from those in the earlier work by Buch and Devlin [144]. However, since we expect a frequency ordering of AD > AAD [142], the peak at  $3704\text{ cm}^{-1}$  is the dangling OH that belongs to three-coordinated water molecules while the peak at position of  $3719\text{ cm}^{-1}$  is from 2-coordinated molecules.

Since the intensity of the  $3719\text{ cm}^{-1}$  peak is higher than the intensity of  $3704\text{ cm}^{-1}$  (Figure 4.4 **a** and **b**), 2-coordinated water molecules are more abundant than 3-coordinated H<sub>2</sub>O in the water clusters studied in the current work. The exact reasons for this are unknown. Since we know that small water clusters ( $n \leq 6$ ) are always cyclic in HeDs and we have also found evidence for cyclic forms of the heptamer and octamer, this may suggest that ring-like structures also predominate in larger water clusters in HeDs. However, there is no suggestion here of a single ring. Instead, it might be that the clusters are arranged in the form of several small connected rings, where most water molecules are of the AD variety but those at the connection points are 3-coordinate molecules. Such a scenario would explain the predominance of the signal  $3719\text{ cm}^{-1}$  from 2-coordinate molecules while also explaining the additional  $3704\text{ cm}^{-1}$  signal from 3-coordinate molecules.

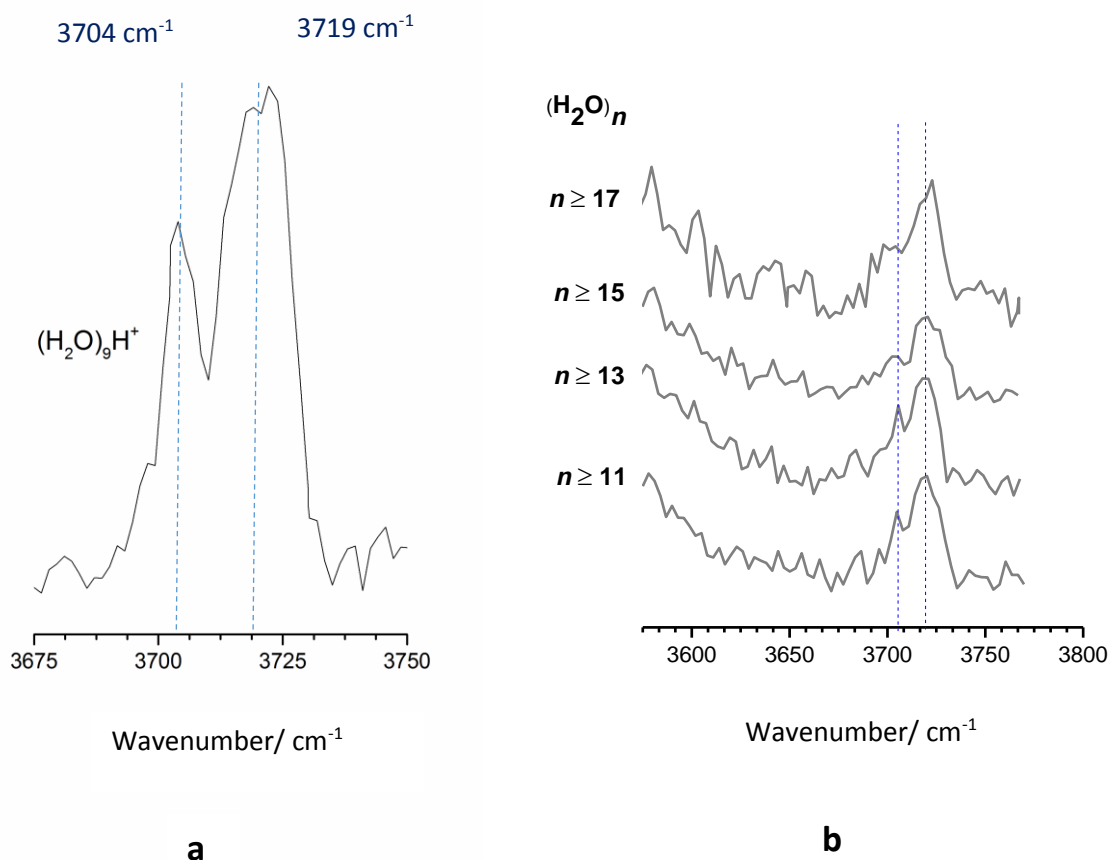


**Figure 4.4** Free OH stretching region, **a** is recorded by detecting  $\text{H}^+(\text{H}_2\text{O})_9$  ions. This spectrum was obtained at a water pressure higher than that used to record the spectrum in Figure 4.2. - **b** Free OH spectra of larger water clusters the free-OH stretch at  $3719\text{ cm}^{-1}$  is the dominant feature in IR spectra up to (at least)  $n = 17$ , showing that clusters up to  $n = 17$  also have many unbound OH bonds.

#### 4.4 Comparison between IR spectra of large water clusters, liquid water and ice

Page *et al.* [109] studied infrared spectra in a supersonic molecular beam of large water clusters and compared their water cluster spectra with literature spectra of ice  $\text{I}_h$  (the hexagonal crystal form of ordinary ice) at a temperature of 50 K [145] and liquid water at a temperature of 313 K [146]. They observed that the broad IR absorption of large water clusters in the bonded OH region is similar to the broad absorption of

liquid water [146], as well as the spectrum of thin films of ice [145]. Page *et al.* observed the free OH stretching band at  $3715\text{ cm}^{-1}$  in the  $(\text{H}_2\text{O})_{19}$  spectrum, where as it was absent in ice and liquid water [109]. Buck co-workers observed that the free OH gradually disappears with increasing water cluster size ( $n = 85$  to  $n = 475$ ) (Figure 4.5) [127], which indicated that only four- coordinated molecules (AADD) are formed once the clusters become sufficiently large [144]. Small water clusters show their highest bonded OH band intensity at  $3400\text{ cm}^{-1}$  while for larger clusters this occurs at  $3200\text{ cm}^{-1}$  [127].

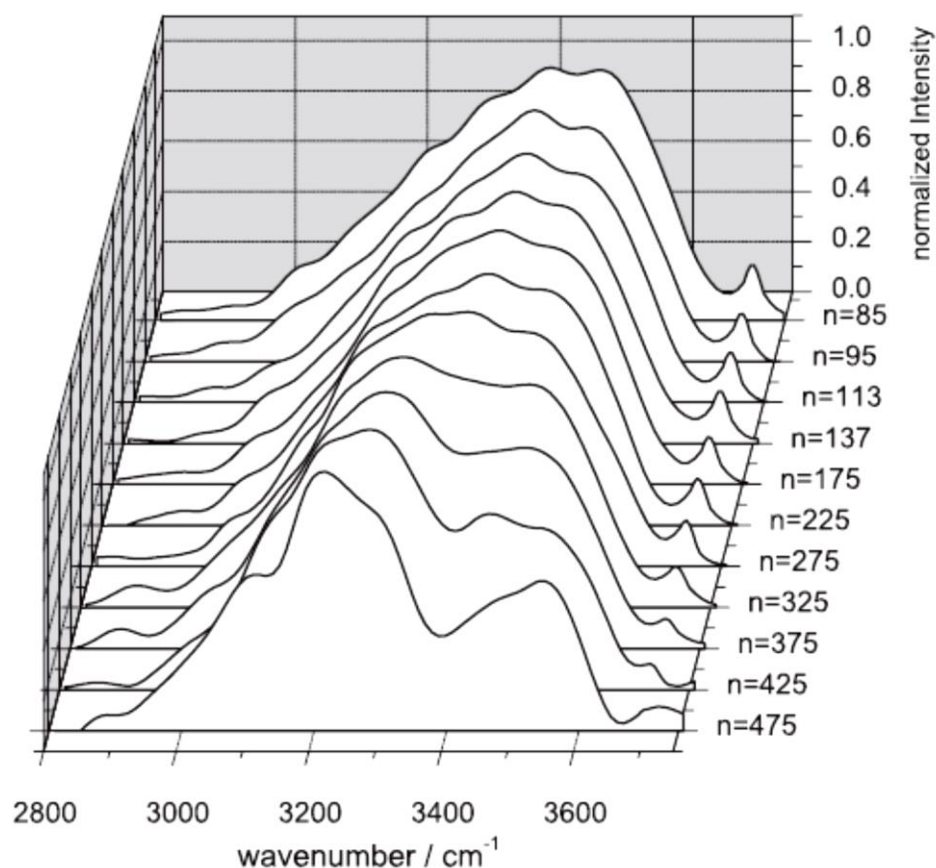


**Figure 4.5.** Size-selective IR spectra of  $(\text{H}_2\text{O})_n$  ( $n = 85 - 475$ ), reprinted from reference [127].

IR spectra of water clusters in the present work are compared with those of liquid water, supercooled water and ice [128,146,148], in Figure 4.6. Crystalline ice has almost exclusively 4-coordinated water molecules [149], while supercooled water has both 3- coordinated and 4- coordinated molecules [149]. The obvious finding from Figure 4.6 is that the bonded OH regions for supercooled water, and especially ice

(Figure 4.6 (b)), have very different shapes and maxima in comparison with liquid water. In addition, the spectra from both supercooled water and ice I<sub>h</sub> are different than those of the water clusters recorded in the present study (Figure 4.6 (a)). The maximum intensity of the OH bonded band of the largest water cluster (H<sub>2</sub>O)<sub>n</sub>,  $n \geq 21$ , is around 3450 cm<sup>-1</sup>, which is a long way from the maximum seen for supercooled water which is at 3300 cm<sup>-1</sup> [150]. The water cluster spectra are very different than those of the crystalline ice since the crystalline ice has a maximum main peak at ~ 3200 cm<sup>-1</sup>.

There is no significant free OH absorption in liquid water and the maximum peak intensity of water clusters is higher than those of liquid water. However, the liquid water clusters spectrum is closest to the water clusters' spectrum since the OH bonded spectrum of liquid water is similar to that of (H<sub>2</sub>O)<sub>n</sub> where  $n \geq 17$  (in the present work), in terms of the position of the highest bonded OH intensity, as shown in Figure 4.6. This suggests that the structures of water clusters in the present work are similar to the spectrum of liquid water.

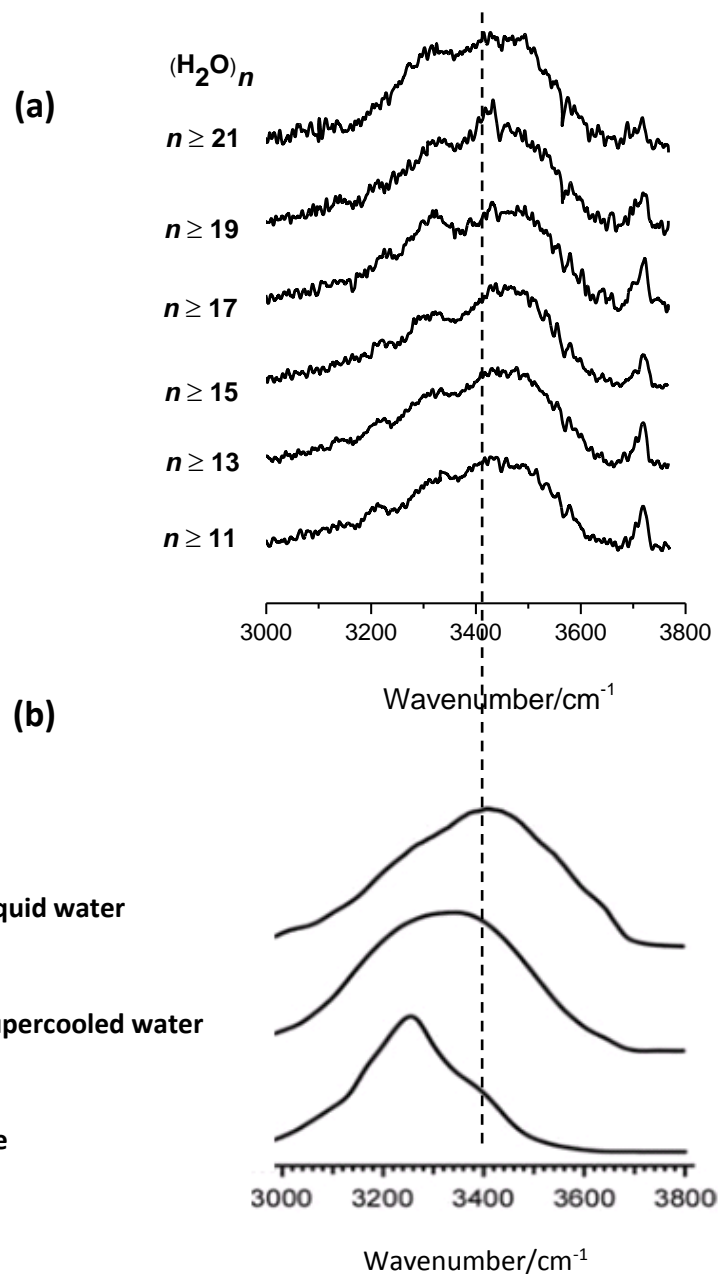


**Figure 4.6** (a) Infrared spectra of large water clusters (this work). (b) Infrared spectra of liquid water at 298K, supercooled water at 240 K and water ice at 235 K (reprinted from reference [128]).

The position of highest intensity of the large water cluster spectra in the present work is shifted to red from  $n \geq 17$  to  $n = 21$  (Figure 4.6 a). The same trend was observed in Figure 4.5 of clusters from  $n = 85$  to  $n = 475$  [127]. In addition, the position of the peak maximum of the spectrum at  $n \geq 17$  (Figure 4.6 a) is similar to that of  $n = 85$  in the Figure 4.5 and is also close to the shape of liquid water spectrum in the Figure 4.6 b. While the clusters size is increasing from  $n = 85$  to  $n = 475$  (Figure 4.5), the highest OH intensity at  $n = 475$  is similar to the shape of the ice (Figure 4.5 b). Therefore, the shape of the spectra is initially close to the shape of the

spectrum of bulk water; however it then becomes close to the spectrum of ice as the cluster size is increased.

## 4.5 Conclusions

In this chapter IR, spectra of larger water clusters  $(\text{H}_2\text{O})_n$  ( $n \geq 11, 13, 15, 17, 19, 21$ ) have reported for the first time in HeDs. Mass selectivity was used for each spectrum by detecting specific  $\text{H}^+(\text{H}_2\text{O})_N$  ions, thus avoiding contributions to the spectra from water molecules with  $n < N + 1$ . The OH bonding region shows a blue shift in going from  $n \geq 11$  to  $n \geq 17$ , while there then seems to be a red shift for larger water clusters. The free OH stretching region shows two clear peaks at  $3704$  and  $3719 \text{ cm}^{-1}$ , which are presumed to derive from 3-coordinated and 2-coordinated water molecules, respectively. This suggests that the large water clusters formed two structures of water clusters in HeDs, AD and AAD.

The spectra of large water clusters were compared with those of liquid water, supercooled water, and ice. The comparison shows best agreement between the spectrum for  $(\text{H}_2\text{O})_n$   $n \geq 17$  and liquid water in terms of the intensity maximum in the bonded OH region. Therefore, the structure of water clusters in the current experiment is more likely to be similar to liquid water

## Chapter 5

### *Infrared Spectroscopy of Pure Methanol Clusters*

#### 5.1 Introduction

Hydrogen bonds have a huge effect on the properties of liquid methanol. Study of methanol clusters is a way to understand the intermolecular forces between the methanol molecules. Several experimental studies have been reported on methanol clusters in the gas phase, such as IR spectroscopic work by Huisken and Stemmler for  $(\text{CH}_3\text{OH})_n$  ( $n= 2-4$ ) [151] and work by Buck *et al.* in the CO stretching region for the dimer through to the octamer [152]. A peak was observed for  $(\text{CH}_3\text{OH})_n$  clusters for  $n = 2 - 5$ . The observation of single peaks when there are multiple OH groups was explained by ring (cyclic) structures in which all of the CO bonds are equivalent [151,152].

However, a different situation was found for the methanol hexamer. For the hexamer, two CO stretching bands were observed and these were assigned two different isomers; one with an approximately planer cyclic structure and the other to a distorted cyclic structure. Likewise, double CO stretching bands were seen for the heptamer and octamer [152].

Although the methanol trimer was observed as a cyclic structure [152], however it was predicted as asymmetric cyclic structure via theoretical calculations [1523,154]. The asymmetric feature results from that the Me group ( $-\text{CH}_3$ ) where in one of the methanol molecules the Me group is pointing up while the Me of the other methanol molecules are pointing down to the plane that contains the O atoms [153-155]. This theoretical result was confirmed experimentally by Huisken *et al.* in 1996 [155]. They used size selectivity for the methanol trimer, and they recorded three signals of OH stretching at 3434, 3472 and 3503  $\text{cm}^{-1}$ , which were explained as asymmetric cyclic structure [155].

IR spectra of methanol clusters larger than hexamer were recorded via a size selective method for  $(\text{CH}_3\text{OH})_n$  with  $n = 4 - 9$  in the OH stretching region and  $n = 7 - 8$  in the CO region by Buck and Ettischer, and they predicted symmetric and asymmetric ring structures for even and odd numbers of methanol molecules, respectively [156]. Many experiments about methanol molecules in the gas phase were performed via both infrared and Raman spectroscopy, and through expansion of methanol molecules in supersonically cooling systems and in molecular beam expansion [157-164]. These experiments showed signals of cyclic structures for both  $(\text{CH}_3\text{OH})_3$  and  $(\text{CH}_3\text{OH})_4$  while a broad band of OH stretching was observed in a range of 3000 to 3700  $\text{cm}^{-1}$  at clusters larger than methanol tetramer [157-164].

In addition, experiments on methanol clusters trapped in low temperature matrices have been reported. Coussan *et al.* observed methanol trimer in the OH stretching in solid nitrogen using IR spectroscopy [165]. They observed spectra of two ring structures and three open chain structures of methanol trimer [155]. In addition, Coussan *et al.* observed different isotopic of four stable structures of dimer methanol in argon matrix at 7 K in infrared OH and CO stretching regions [166,167]. Perchard and Mielke have IR spectra of the monomer and dimer methanol in solid argon and nitrogen matrices [168].

Theoretical calculations performed to study different structures of methanol clusters, which can be categorised as cyclic, chain and branched chain structures [169]. It was predicted that the cyclic structure is the most stable conformer for trimer, tetramer and pentamer methanol clusters [169] and also for  $(\text{CH}_3\text{OH})_4$  at B3LYP theory [170]. Nishmiura *et al.* explained both OH and CH stretching vibrations of methanol clusters from dimer methanol to pentamer methanol by the self-consistent-charge density functional tight-binding SCC-DFTB method [171]. However, For clusters larger than the pentamer, Kazachenko *et al.* predicted  $(\text{CH}_3\text{OH})_n$  structures at both B3LYP-DCP and BLYP-D3 levels of theory [172]. They predicted noncyclic conformers of methanol clusters while it became folded and twisted at clusters larger than octamer methanol [172].

Behrens *et al.* studied methanol in HeDs in 1999 [173]. They observed methanol spectra in the CO stretching region and used depletion spectroscopy with mass-selective detection of ions [173]. Their results for the methanol trimer were in agreement with previous experiments in the gas phase [152], i.e. were consistent with a cyclic structure. However, the spectra for  $(\text{CH}_3\text{OH})_4$  and  $(\text{CH}_3\text{OH})_5$  were attributed to non-cyclic structures and are explained as  $(\text{CH}_3\text{OH})$  or  $(\text{CH}_3\text{OH})_2$  attached to a trimer ring cluster [173]. The difference in structures between the gas phase clusters and those in HeDs was attributed to the low temperature in HeDs and its ability to trap clusters in a local minimum energy instead of the lowest energy minimum. Something similar has been seen previously for water clusters, as was discussed in Chapter 3. What was found for water clusters was that cyclic structures are seen for the trimer, tetramer and pentamer in HeDs and this is consistent with the gas phase [174]. However, while a non-cyclic structure is the most stable for water hexamer only the cyclic structure forms in HeDs [101,175]. In addition, we reported evidence for the cyclic water heptamer and octamer in HeDs in Chapter 3. Note that the only other spectroscopic study of methanol in HeDs focused on the methanol monomer [176].

In this work, infrared spectra of methanol clusters are reported in HeDs in the OH stretching region for first time and are in agreement with those in the gas phase. In support of the experimental work *ab initio* calculations were performed. The calculations shows that the experimental spectra of tetramer and pentamer methanol clusters in HeDs in OH stretching are cyclic structure

## 5.2 Experimental

The present work has been done using the experimental setup described in Chapter 2 and therefore details here are restricted to the experimental conditions used. Helium droplets were generated at a nozzle temperature of 16 K and a stagnation pressure of 33 bar, conditions which should produce HeDs of an average size of about 5000 atoms [35].

$\text{CH}_3\text{OH}$  molecules were provided to a pickup cell via a needle valve. A low amount of methanol was used to avoid production of a significant quantity of methanol clusters

larger than  $(\text{CH}_3\text{OH})_5$ . An indication of the amount of methanol captured by the HeDs can be gained from observation of a mass spectrum, and example of which is shown in Figure 5.1. The mass spectrum shows clear ion signals which derive from  $(\text{CH}_3\text{OH})_n$  clusters and these monotonically decline with mass. As detailed later the cluster ions observed correspond to  $(\text{CH}_3\text{OH})_n\text{H}^+$  which derive from the fragmentation of larger clusters on ionization.

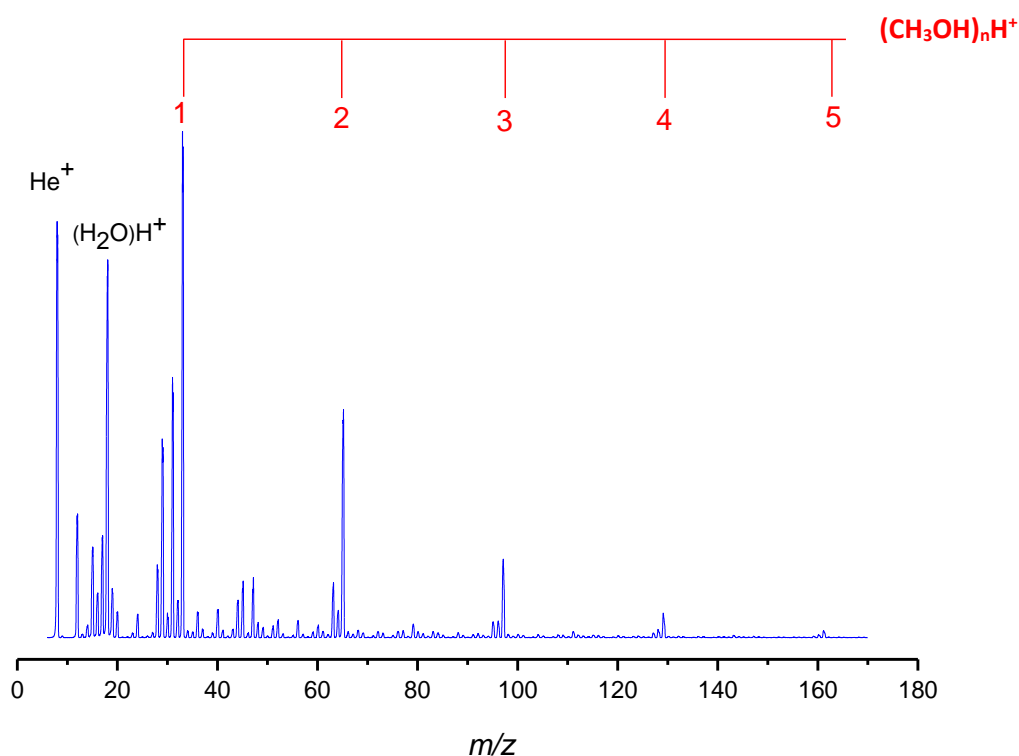


**Figure 5.1.** Mass spectrum of methanol clusters in a range from  $m/z = 8$  to 170.

Infrared spectra in the OH stretching region for  $(\text{CH}_3\text{OH})_n$   $n=1$  to 5 were observed via depletion spectroscopy in the range of  $3000 - 3700 \text{ cm}^{-1}$ . Measurements were made for a specific ion mass, as detailed again later.

### 5.3 Computational details

Theoretical calculations were performed to predict IR spectra of optimised fully cyclic and branched cyclic methanol structures. These calculations were performed via Gaussian 09 [177] using the Slater cluster at the UK National Service for Computational Chemistry Software (NSCCS).

In the current work, two sorts of methanol clusters structures are calculated; fully cyclic and branched structures. Finding most stable structure of each full-cyclic methanol clusters is managed by adding methanol monomers to the global minima energy of the lower methanol clusters size to obtain the next larger methanol ring structure. This procedure is started with the optimised CH<sub>3</sub>OH monomer and adding a new methanol molecule to get global minima energy of the methanol dimer. A third methanol molecule is added to the optimised methanol dimer to create a methanol trimer cluster. This process was continued to get tetramer and pentamer cyclic methanol clusters. Finally the IR spectra for optimised cyclic tetramer and optimised cyclic pentamer are calculated to get OH stretching spectra for each structure.

For the second group of the methanol clusters, which is the branched structure for methanol clusters, the monomer methanol or optimised methanol dimer is added to the outside of the global minima energy of the cyclic methanol trimer. Then the structure is optimised to the minimum global energy, and the OH frequencies of each optimum structure is calculated to predict positions of OH stretching for the clusters.

The notation used to distinguish between fully cyclic and branched structures is  $n + m$ , where  $n$  refers to the number of methanol molecules in the ring and  $m$  is the number dangling from that ring (in a chain). Thus a 4+0 structure implies a fully cyclic tetramer whereas 3+1 implies a ring trimer with a fourth methanol molecule hydrogen-bonded to one of the methanol molecules in the ring.

MP2 theory and aug-cc-pVDZ basis sets are used for all structures in the current work except the 3+2 structure, which is optimised to the global minimum energy using DFT/B3LYP theory and same previous basis sets. For the prediction of vibrational frequencies, a scaling of the harmonic vibrational frequencies was used. The scale factor employed in the present work was 0.972. This value was obtained by

comparison the OH stretching of the well known methanol dimer to our calculated dimer methanol. However, this scale factor is not used for the 3+1 methanol structure whose OH stretching frequencies were instead scaled by 0.976 (see later)

## 5.4 Results and discussion

IR spectra of methanol clusters were recorded in both the CH and OH stretching regions spanning the range 2800 – 3800  $\text{cm}^{-1}$ , as shown in Figure 5.2. The lowest trace was recorded at an  $m/z$  of 33, which corresponds to detection of the  $(\text{CH}_3\text{OH})\text{H}^+$  ion (Figure 5.2a). IR spectra at  $m/z$  of 33 shows OH stretching of methanol dimer and larger clusters since mass selectivity is used in this work. A spectrum obtained by detecting a larger cluster ion,  $(\text{CH}_3\text{OH})_3\text{H}^+$  ( $m/z$  of 97) is shown in Figure 5.2b. A third spectrum also obtained by detecting  $(\text{CH}_3\text{OH})_3\text{H}^+$ , is shown in Figure 5.2c and was obtained at a higher methanol pressure in the pick up chamber than that used for Figure 5.2b.

Previous study of methanol clusters [173] concluded that the fragmentations of  $\text{CH}_3\text{OH}$  in HeDs takes place during the ionization process, as shown in the scheme below:



Thus, for example, any IR signals due to detecting  $m/z$  33  $(\text{CH}_3\text{OH})\text{H}^+$  could come from the neutral methanol dimer or trimer according to equations (5-1) and (5-2). IR signals from both methanol dimer and methanol trimer (Figure 5.2a) were indeed observed at  $m/z$  33 in the present work. However, there are also signals from the tetramer and a very small signal for the pentamer. Therefore, the ion fragmentation is more extensive than implied in the equations above.

The IR spectrum at  $m/z$  33 shows four peaks indicated by the highest intensity for a given cluster (vertical dashed lines in Figure 5.2). Note that detection of  $(\text{CH}_3\text{OH})\text{H}^+$  means that the neutral monomer cannot contribute to this IR spectrum. The weak signal at  $3686\text{ cm}^{-1}$  and the stronger one at  $3571\text{ cm}^{-1}$  are both assigned to the methanol dimer since they are absent in spectra recorded at higher masses (e.g.  $m/z$  97). This assignment is in excellent agreement with previous experimental work [157,158]. The higher frequency  $3686\text{ cm}^{-1}$  peak corresponds to IR absorption by a dangling OH group, while that at  $3571\text{ cm}^{-1}$  is from the other OH group, which is involved in a hydrogen bond. A significant red-shift is characteristic of OH groups involved in hydrogen bonding and arises because the hydrogen bond weakens the O-H bond.

The highest intensity peak recorded in Figure 5.2a ( $m/z$  33) is seen at  $3477\text{ cm}^{-1}$ . This peak is the OH stretching band of methanol trimer and this is easily confirmed since it disappears from the spectrum recorded at  $m/z$  97 (Figure 5.2b). Furthermore, this band is in good agreement with earlier reports in the gas phase [157,158]. Finally, the lowest frequency peak at  $3295\text{ cm}^{-1}$  recorded by detecting  $m/z$  33 corresponds to the methanol tetramer. Once again the position of this peak is in agreement with earlier studies in the gas phase [157,158].

Conversely, the spectrum at  $m/z$  97 in the Figure 5.2b shows only two strong peaks which derive from methanol tetramer and methanol pentamer. When the vapour pressure of methanol is increased, the pentamer peak becomes slightly stronger and broader (see Figure 5.2c). The broadening of this peak may be the result of underlying contributions from clusters larger than the pentamer, although we have no direct evidence for this. This is, however, plausible since the difference in peak positions for the pentamer and the hexamer is likely to be small.

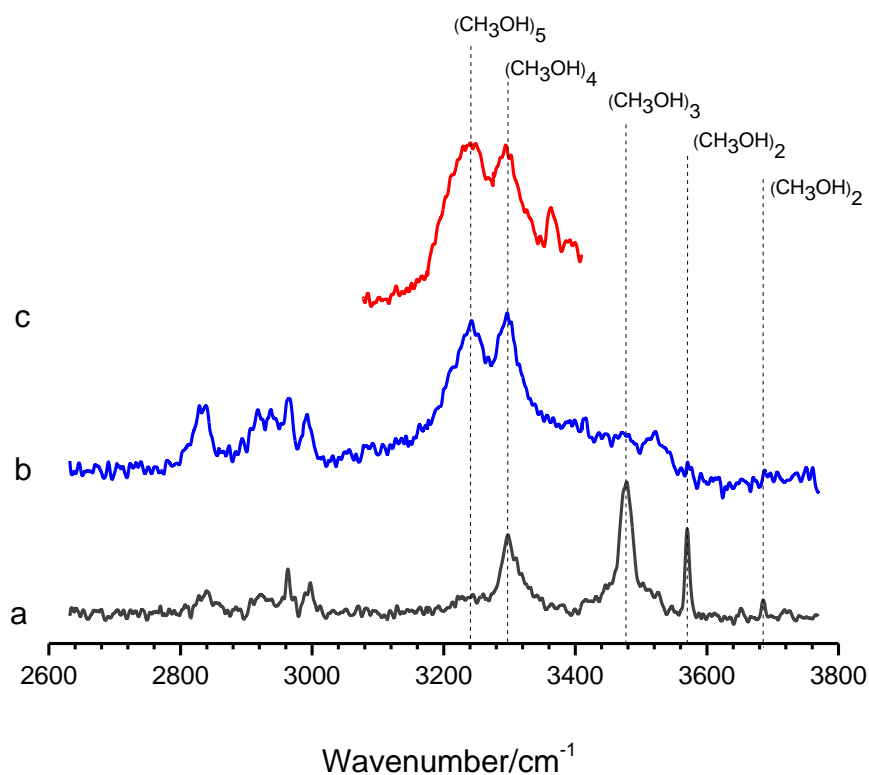


**Figure 5.2.** Experimental IR spectra of methanol clusters recorded using depletion spectroscopy. The lowest trace ((a), black colour) was recorded by detecting ions at  $m/z$  33. The blue spectrum (b) was recorded by detecting at  $m/z$  97. The red spectrum (c) was also obtained for  $m/z$  97 but at a higher methanol pressure than spectrum (b).

To support the assignment our experimental results of observing methanol cyclic structures in HeDs, theoretical calculations of fully cyclic methanol clusters (3+0, 4+0 and 5+0) and branched cyclic structures of both tetramer (3+1) and pentamer (3+2) are performed, as shown in Figure 5.3 and 5.4.

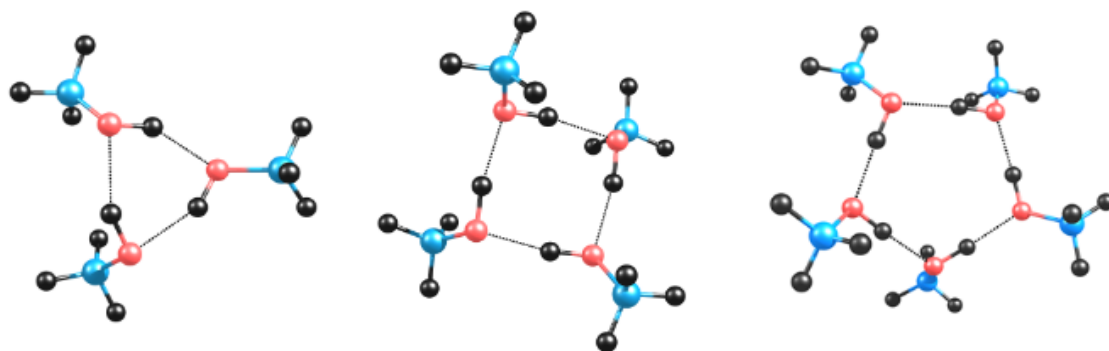


**Figure 5.3.** Optimised fully cyclic structures of  $(\text{CH}_3\text{OH})_3$ ,  $(\text{CH}_3\text{OH})_4$  and  $(\text{CH}_3\text{OH})_4$  at MP2/aug-pVDZ.

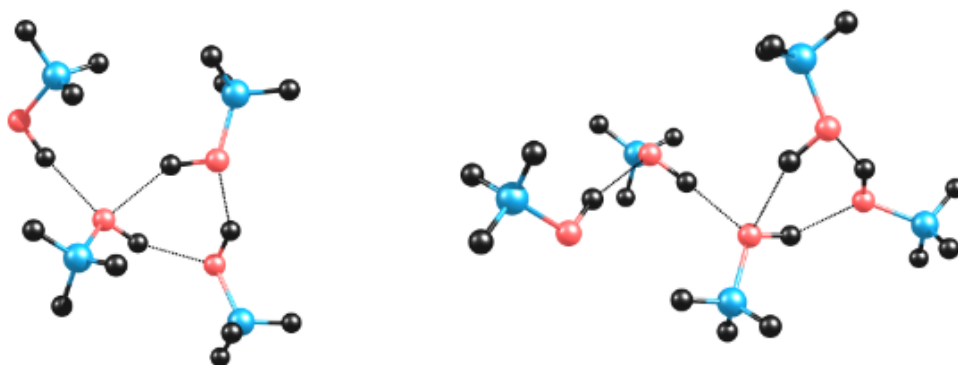


**Figure 5.4.** Optimum structures of methanol clusters. Left: cluster 3+1 predicted at MP2/aug-cc-pVDZ. Right: structure 3+2 performed at DFT-B3LYP/aug-cc-pVDZ.

Our *ab initio* calculations of the IR spectra of the cyclic structures (Figure 5.5) of both trimer (blue line) and tetramer (black line) are in excellent agreement with the observed IR spectra in current work. However, the previous study of observing methanol clusters in HeDs concluded that the observed band of tetramer methanol in the CO region was assigned to 3+1 methanol structure [173]. Since our prediction for tetramer methanol is different from previous study, the calculated IR spectrum of branched tetramer methanol (3+1) are compared with experimental IR spectrum, as shown in Figure 5.5. While the cyclic tetramer methanol has a simple band of OH

stretching, the 3+1 methanol structure consists of five different OH stretching bands. These bands are far away from the experimental peak ( $3477\text{ cm}^{-1}$ ) of the methanol tetramer and other bands predicted (red lines) for the 3+1 tetramer are missing from the observed spectrum. Therefore, the branched cyclic tetramer structure clearly does not form in HeDs in our experiments.

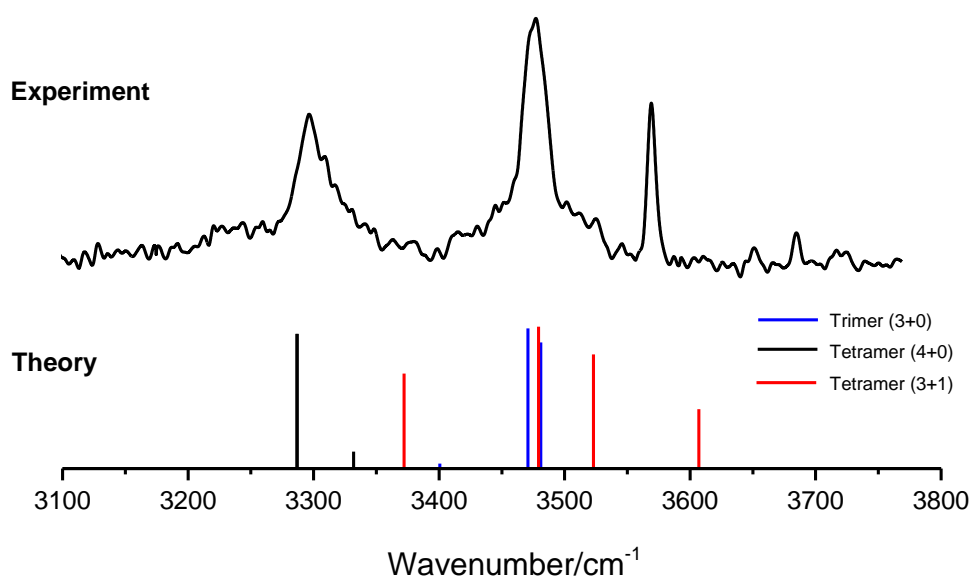


**Figure 5.5.** Observed infrared spectrum for  $m/z = 33$  (pure methanol), higher trace. The lower trace show the OH stretching bands predicted from ab initio calculations for different methanol structures.

The OH stretching band of methanol pentamer was observed at  $3295\text{ cm}^{-1}$ , as shown in Figure 5.6. This peak is in agreement with theoretical predictions for a cyclic pentamer, as well as agreeing with several gas phase studies [157,158]. However in the study by Behrens et al. of methanol clusters in HeDs, a branched structure (3+2) was deduced. We performed DFT calculations for the 3+2 structure at the B3LYP/aug-cc-pVDZ level of theory and the predicted IR spectrum is shown in Figure 5.6. Here, the 3+2 structure does not converge to stable conformer via using MP2 theory. Since the 3+2 structure

is an asymmetrical structure, five different OH stretching bands are predicted. This is clearly very different to the experimental IR spectrum and this rule out any significant contribution from the 3+2 structure.

The experimental peak at  $3295\text{ cm}^{-1}$  cannot be assigned to  $(\text{CH}_3\text{OH})_5$  although theoretical calculations of  $(\text{CH}_3\text{OH})_5$  shows two weak OH stretching close to  $3300\text{ cm}^{-1}$  (Figure 5.6). This because the peak at  $3295\text{ cm}^{-1}$  disappeared in the IR spectrum recorded at higher mass channel ( $m/z = 129$ ,  $(\text{CH}_3\text{OH})_4\text{H}^+$ ).

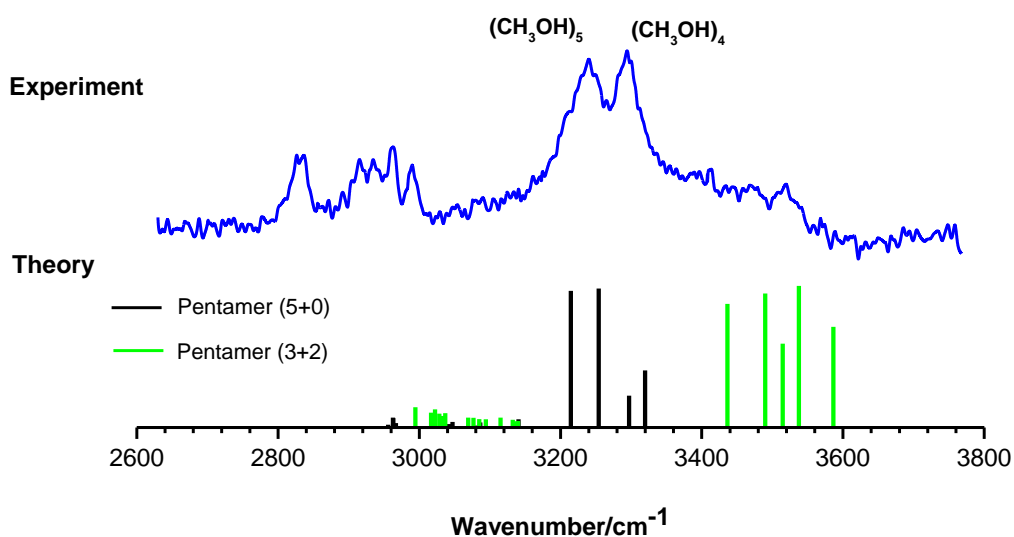


**Figure 5.6.** The higher trace is the experimental spectrum at  $m/z$  of 97 which includes peaks from the methanol tetramer and pentamer. The lower trace is the predicted OH stretching of 5+0 and 3+2 methanol pentamers.

The fact that we see structures of methanol clusters in HeDs that are different from those reported in the earlier work by Behrens *et al.* [173] merits some explanation. There are a number of possibilities. One possibility is that very different helium droplet sizes were used in that earlier work compared to ours. Behrens *et al.* apparently used droplets with a mean size of 2700 helium atoms, which is smaller than

those used in the present work (ca. 5000). Perhaps the cooling efficiency in these smaller droplets was insufficient to quench the structures into their lowest energy minimum in every case, although this would seem an unlikely explanation for the different structures. A more likely explanation is the poor quality of the IR spectra recorded in the CO stretching region. Furthermore, the CO stretching region is not particularly sensitive to changes in structure, particularly for a hydrogen-bonded system, when compared to the OH stretching region.

## 5.5 Conclusions

In the present work, IR spectra of methanol clusters have been recorded in the OH stretching region in HeDs for the first time. The IR spectra were recorded mass selectively and this has helped with the assignments of the spectral carriers. Further information has also been extracted from *ab initio* calculations. The calculations are in excellent agreement with our experimental IR spectra for fully cyclic structures for the clusters. In contrast, our theoretical predictions of spectra for the branched cyclic structures are not consistent with our observations. This suggests that earlier work on methanol clusters in HeDs, which recorded spectra in the CO stretching region, and which gave rise to claims of branched cyclic structures for the methanol tetramer and pentamer, are likely

## Chapter 6

### *Mixed methanol and water clusters*

#### 6.1 Introduction

Mixtures of methanol and water are interesting since both molecules have substantial hydrogen bonds in the pure liquids and therefore the question arises as to how the hydrogen bonds are affected in mixtures [178]. The simplest water/methanol mixture is the heterodimer  $(\text{CH}_3\text{OH})\text{H}_2\text{O}$ . This cluster may be able to produce some insight to the interaction that take place in bulk methanol/water. Consequently, this dimer has been extensively studied in the gas phase. Studies of mixtures of methanol and water concentrated mostly on the heterodimer [178-189]. These studies started with the experimental work of Huisken *et al.* in 1991, when they recorded IR spectra of  $(\text{CH}_3\text{OH})\text{H}_2\text{O}$  via photodepletion spectroscopy [179]. Their spectra were found to be consistent with the methanol molecule playing the role of proton acceptor and the water the proton donor, i.e.  $\text{CH}_3\text{HO}\dots\text{HOH}$  [179]. We shall abbreviate this structure by the label WM (here water (W) is the proton donor since it is written first while methanol (M) is the acceptor). However, experimental work of Bakkas *et al.* in a  $\text{N}_2$  matrix recorded an IR spectrum of a  $\text{CH}_3\text{OH}\dots\text{OH}_2$  structure, where methanol is the proton donor and water the acceptor (MW structure) [180]. In an argon matrix the structure reverted to that seen in the gas phase experiment [181].

Theoretical studies identified the WM as a lower energy minimum than the MW conformer [182,183,185,189] and showed that the hydrogen bond in WM is stronger (and shorter) than in MW structure, as shown in Figure 6.1 [189]. The energy minima of WM and MW have also been studied theoretically via calculations of diffusion Monte Carlo (DMC) method. The calculations predicted greater difference in the energy minima between the WM and MW isomers in comparison with calculations that do not include internal rotations [186].

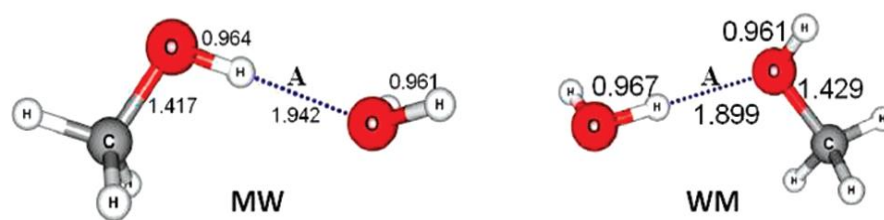


**Figure 6.1.** Methanol-water dimer structures. In MW methanol is a proton donor and in the WM water is the proton donor [189].

Although  $\text{CH}_3\text{OH}(\text{H}_2\text{O})$  complexes have been the subject of many experimental and theoretical studies, larger  $(\text{CH}_3\text{OH})_n\text{H}_2\text{O}$  ( $n > 2$ ) species have been only investigated in a small number of studies [182, 184, 188-191, 193]. For example, Mejía *et al.* performed MP2 and B3LYP calculations of geometry optimization of  $(\text{CH}_3\text{OH})_3\text{H}_2\text{O}$  [188]. They predicted that the fully cyclic structure is the most stable structure of  $(\text{CH}_3\text{OH})_3\text{H}_2\text{O}$ , and they predicted that the increasing number of molecules in  $(\text{CH}_3\text{OH})_n\text{H}_2\text{O}$  causes increase in stability of the cluster [188].

IR spectra of the  $(\text{CH}_3\text{OH})\text{OH}$  radical-molecule complex was recently observed in HeDs in OH stretching region via depletion spectroscopy [192]. The only spectroscopic study of methanol clusters attached to a monomer water were performed using IR and Raman spectroscopy [190]. In this experiment, the signal from OH stretching of Raman spectrum was assigned to dimer methanol attached to monomer water. In addition, two uncertain OH stretching bands were recorded from trimer methanol attached to a single water molecule (M3W) and tetramer methanol with one water molecule (M4W) [190], while no IR spectra were assigned to these clusters.

In the present work, IR spectra of methanol clusters attached to water monomer in OH stretching region in HeDs have been recorded for first time, along with *ab initio* calculations in support of the experimental work. Also the current work is the first spectroscopic observation of infrared spectra of  $(\text{CH}_3\text{OH})_n \text{H}_2\text{O}$  ( $n=2,3$ ).

## 6.2 Experimental details

The experimental setup of the present work is similar to those described in Chapters 3-5. In the current experiment, a mixture of 80:20 of methanol/water by volume is prepared in liquid state. The ratio of vapour methanol to water in volume was 31:1 because methanol has a higher vapour than water. Here, a lower amount of water is used in attempt to add a single H<sub>2</sub>O molecule to the methanol clusters. This was observed in mass spectra of the mixture as a series of ion signals of monomer water attached to methanol clusters (Figure 6.2). The mixture was kept at 2 °C temperature during the experimental work. Vapour of the mixture was added to the pick-up cell of vacuum system and the amount of the vapour was controlled via a needle valve. Experimental conditions of the stagnation temperature (16 K) and pressure (33 bar) were similar to those of the pure methanol experiment (see Chapter 5).

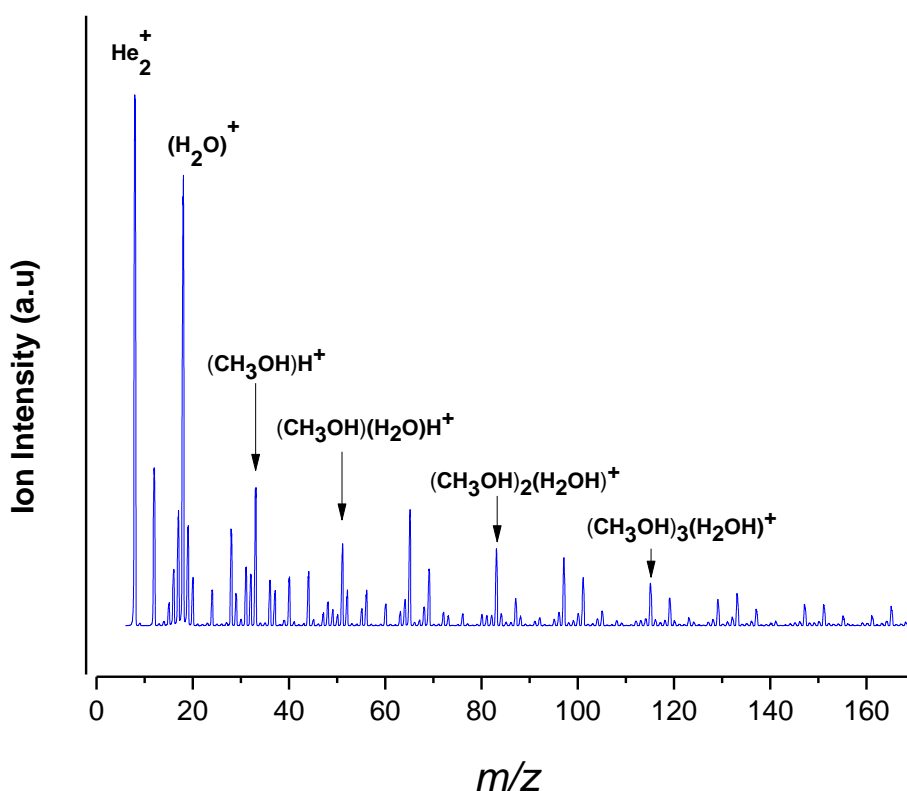


**Figure 6.2.** Mass spectrum in the range from  $m/z = 4$  to 170 of a mixture methanol and water at a vapour mix of methanol/H<sub>2</sub>O of 31: 1. The mass spectrum shows clear signals of methanol clusters attached to single water molecule.

### 6.3 Computational Details

*Ab initio* calculations were performed in the current work to assist in the assignment of the experimental spectra. These calculations confirm the experimental results of both  $(\text{CH}_3\text{OH})_2\text{H}_2\text{O}$  and  $(\text{CH}_3\text{OH})_3\text{H}_2\text{O}$ , as shown in Figure 6.3. In these calculations, optimum structures of the  $(\text{CH}_3\text{OH})_2$  and cyclic  $(\text{CH}_3\text{OH})_3$  were predicted first, and then the water monomer was added to the optimised methanol structure. Calculations were performed at the MP2/aug-cc-pVDZ level of theory. Since harmonic calculations were used to predict the appearance of vibrational spectra, the OH stretching needed to be scaled to by a scale factor value to facilitate comparison with the experimental results. OH vibrational frequencies are scaled by 0.972. This value, as we described in chapter 5, is obtained via comparison of the experimental OH stretching vibrational frequency of the methanol dimer with our calculated value.

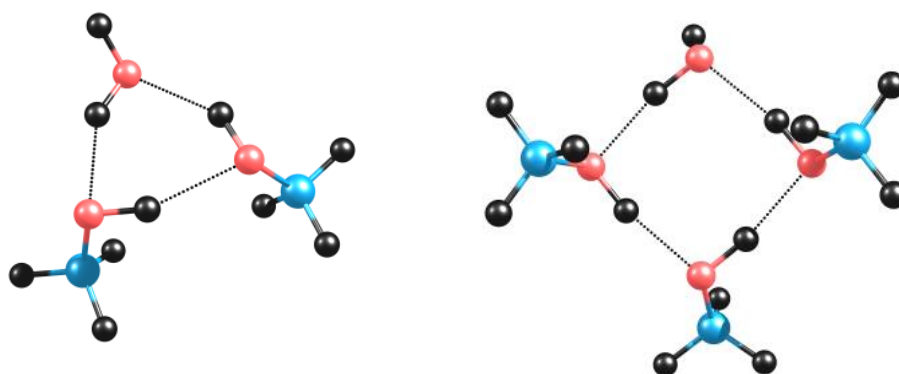


**Figure 6.3.** Optimum structures of  $(\text{CH}_3\text{OH})_2\text{H}_2\text{O}$  and  $(\text{CH}_3\text{OH})_3\text{H}_2\text{O}$  are calculated via double harmonic calculations at MP2/aug-cc-pVDZ.

### 6.4 Results and discussion

The starting point for this work was the IR spectrum obtained from the pickup of methanol only, which is shown by the black trace in Figure 6.4. Here, we chose the range  $3455 - 3750 \text{ cm}^{-1}$  because it includes the OH stretching bands of both  $\text{H}_2\text{O}$  and

CH<sub>3</sub>OH. As already discussed in Chapter 5 and Figure 5.2, methanol dimer peaks are seen at 3686 cm<sup>-1</sup> (free OH stretch) and 3571 cm<sup>-1</sup> (bonded OH stretch), while the methanol trimer has a peak at 3477 cm<sup>-1</sup>.

Next, a spectrum was recorded with a mixture of 4% water (by volume) in methanol (expected vapour abundance ratio of methanol/water = 185: 1). This showed a new and small signal at 3530 cm<sup>-1</sup> (see Figure 4.6). This peak become stronger when the water concentration was increased to 20% in the mixture (vapour abundance ratio of methanol/water = 31:1).

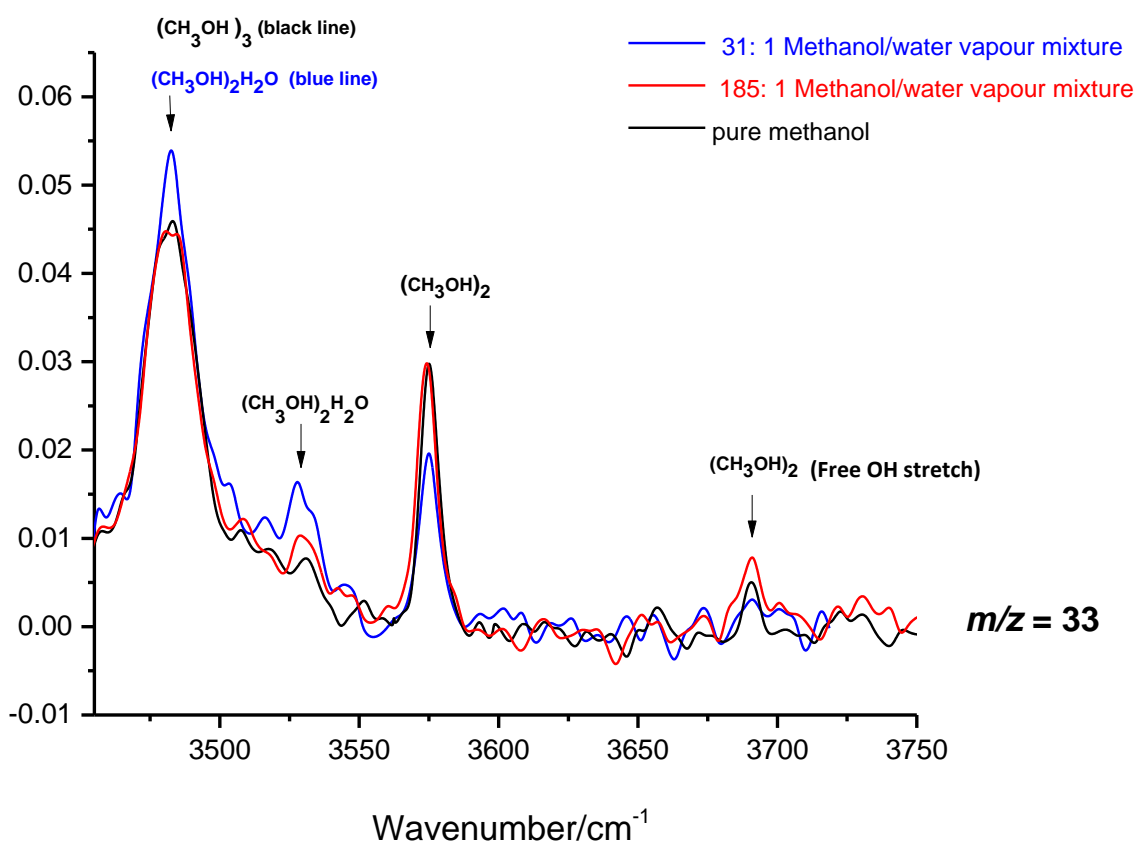


**Figure 6.4.** IR spectra of different mixture of water/methanol in the range 3455 – 3750 cm<sup>-1</sup>.

Figure 6.4 shows that the abundance of the methanol dimer in the HeDs decreases as the amount of water in the mixture increased. This can be observed through the peak at 3571 cm<sup>-1</sup> in spectrum of the mixture 20% of water (blue trace in

the Figure 6.4) which is has lower intensity than that of the mixture 4% (red trace in the Figure 6.4).

However, the strongest peak at  $3477\text{ cm}^{-1}$ , which is in the position of the OH stretching of the methanol trimer, rises with increasing ratio water in the mixtures, as shown in Figure 6.4. This peak is in the same position as the trimer methanol. However, any IR absorption detected by monitoring ions at  $m/z$  of 51 cannot come from pure methanol clusters (since the ion of this mass must contain a water molecule). This must mean that the  $(\text{CH}_3\text{OH})_2\text{H}_2\text{O}$  cluster is created in HeDs, as will be described in more detail later.

Since the mixture of vapour methanol/water at 31:1 shows clear signal of methanol attached to a water monomer, IR spectra of this mixture were recorded in the range  $2800 - 3800\text{ cm}^{-1}$  at two different mass channels: at  $m/z = 33$  and 51. The IR spectrum at mass channel  $m/z$  of 33, which corresponds to  $(\text{CH}_3\text{OH})\text{H}^+$ , shows sharp peaks assigned to the pure methanol dimer, trimer and tetramer, as shown in Figure 6.5. In addition, there are two extra peaks labelled by the red arrows at  $3380\text{ cm}^{-1}$  and  $3525\text{ cm}^{-1}$  in this mass channel. When the mass channel is switched to  $m/z = 51$ , the peaks at  $3380$  and  $3525\text{ cm}^{-1}$  both become more intense than in the spectrum of lower mass channel. *Ab initio* calculations predict two OH stretching bands near  $3400\text{ cm}^{-1}$ , one is an OH stretch of a methanol molecule in  $(\text{CH}_3\text{OH})_3\text{H}_2\text{O}$  and the other is an OH stretch of the water molecule in  $(\text{CH}_3\text{OH})_2\text{H}_2\text{O}$ ; either of these stretch modes could be assigned to the experimentally observed band at  $3380\text{ cm}^{-1}$ . In addition, the calculations predict a band of  $(\text{CH}_3\text{OH})_2\text{H}_2\text{O}$  at  $3530\text{ cm}^{-1}$  that is in reasonable agreement with the experimentally observed bands at  $3525\text{ cm}^{-1}$ , as shown in Figure 6.5.

In addition, there are two strong peaks in the  $m/z = 51$  spectrum at  $3300$  and  $3477\text{ cm}^{-1}$  (Figure 6.5) which are at the same positions as bands seen for  $(\text{CH}_3\text{OH})_4$  and  $(\text{CH}_3\text{OH})_3$ , respectively in the  $m/z = 33$  spectrum. However, there is not any pure methanol cluster in this mass channel as we described before. Therefore, the peaks here are from OH stretching bands of  $(\text{CH}_3\text{OH})_n(\text{H}_2\text{O})$  or  $(\text{CH}_3\text{OH})_n(\text{H}_2\text{O})_2$ , since the mixture contains low amount of the water. *Ab initio* calculations confirm that there are OH stretching bonds of methanol part of the cluster in the positions at  $3280$  and  $3320\text{ cm}^{-1}$  from  $(\text{CH}_3\text{OH})_3\text{H}_2\text{O}$  (blue line in the Figure 6.5) and these are close to the

experimental peak at  $3300\text{ cm}^{-1}$ . The other predicted OH vibration at  $3475\text{ cm}^{-1}$  (which are from excitation of stretching frequencies of methanol molecules in the cluster) is in agreement with experimental peak at  $3477\text{ cm}^{-1}$  that is from cyclic  $(\text{CH}_3\text{OH})_2(\text{H}_2\text{O})$  cluster.

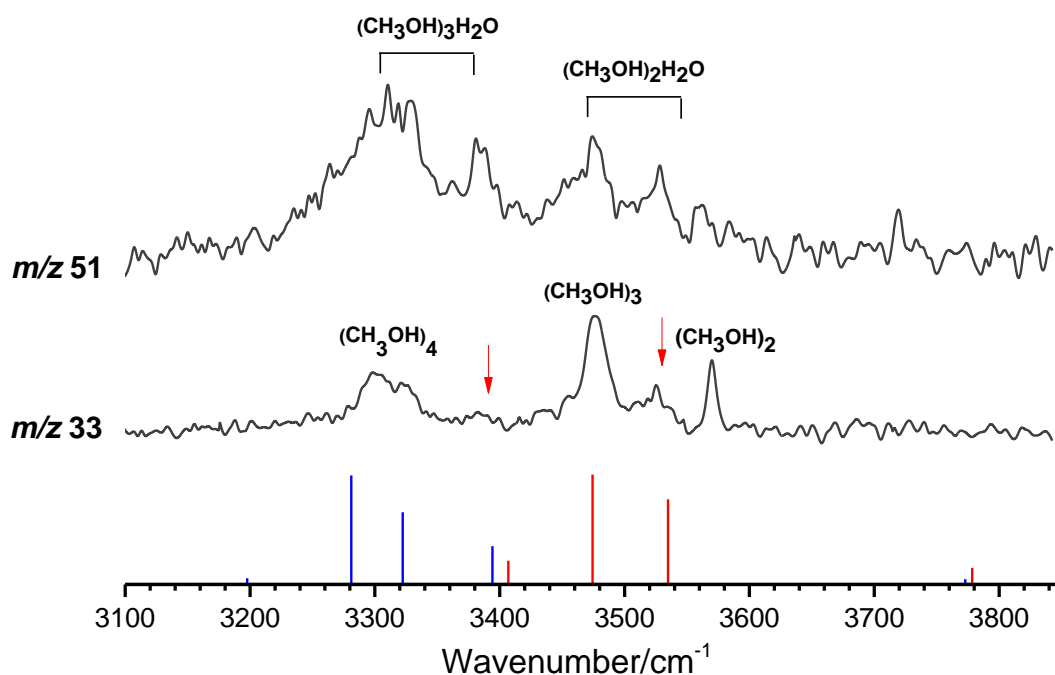


**Figure 6.5.** IR spectra of a mixture of methanol and water in range  $3100 - 3850\text{ cm}^{-1}$  for two different mass channels at  $m/z$  of 33 and 51. The lower trace shows theoretical calculations of band positions for cyclic  $(\text{CH}_3\text{OH})_2\text{H}_2\text{O}$  (red lines) and  $(\text{CH}_3\text{OH})_3\text{H}_2\text{O}$  (blue lines) clusters. Experimental spectra are shown in upper traces. Red arrows refer to attached methanol clusters and monomer water that described in the text.

Therefore, the theoretical calculations confirmed that cyclic structures of both  $(\text{CH}_3\text{OH})_2\text{H}_2\text{O}$  and  $(\text{CH}_3\text{OH})_3\text{H}_2\text{O}$  are observed in HeDs in OH stretching region for first time.

## 6.5 Conclusions

In the current work, IR spectra of mixed  $(\text{CH}_3\text{OH})_2\text{H}_2\text{O}$  and  $(\text{CH}_3\text{OH})_3\text{H}_2\text{O}$  clusters have been recorded for the first time. The observed spectra, in combination with *ab initio* calculations, confirm that these complexes are cyclic.

This work could be expanded in the future to include the detection of IR spectra of larger methanol clusters attached to a water monomer  $(\text{CH}_3\text{OH})_n\text{H}_2\text{O}$  where  $n > 3$  to study their possible structures in HeDs. In addition, structures of the water dimer attached to methanol clusters  $(\text{CH}_3\text{OH})_n(\text{H}_2\text{O})_2$  are also possible to be studied in HeDs through recording their infrared bands whilst changing the ratio of mixture vapour.

## Chapter 7

### *IR spectroscopy of Iodine-Water complexes in helium nanodroplets*

#### 7.1 Introduction

The reactions of halogen atoms with small molecules are classic reactions that have been of much interest to those who study detailed reaction dynamics. Part of the motivation for studying these particular reaction systems is that they are sufficiently small systems that their potential energy surfaces are accessible to realistic quantum mechanical simulation, and especially so for the lighter halogens and their reactions with small organic molecules. For example, several experimental and theoretical investigations have been reported on the dynamics of the reaction  $\text{Cl} + \text{CH}_4 \rightarrow \text{HCl} + \text{CH}_3$  [194]. Hydrogen abstraction from organic molecules by chlorine atoms is also significant in atmospheric chemistry [195-197]

The shape of the reaction potential energy surface is well known to have a significant influence on reaction dynamics and in ion-molecule reactions this has been widely studied [34]. In contrast, few studies have focused on the significance of van der Waals minima of neutral reactions on reacting potential energy surfaces. These minima can have a major impact on the reaction process: for example, entrance channel minima have a role in orientating reactants prior to the transition state [195]. One way to identify and characterize these minima is via *ab initio* calculations. However, because the minima may be very shallow, it becomes important to test the calculations through experimental measurements which directly probe the entrance and exit channel minima. Supersonic expansion and matrix isolation methods have been used as cooling techniques to probe entrance channel complexes but are not always suitable when the complexes have particularly shallow minima because sufficient cooling cannot be achieved to form stable complexes [34].

HeDs can be used as a technique to cool reactants to explore van der Waals minima on reaction potential energy surfaces since rapid cooling of the dopants to 0.37 K (steady state temperature of the HeDs) [34]. The entrance channel complexes of  $\text{X} + \text{HF}$  ( $\text{X} = \text{Cl}$ ,  $\text{Br}$  and  $\text{I}$ ) reactions have been previously studied in HeDs and the first infrared spectra

of these complexes were recorded via depletion spectroscopy [34]. These spectra show that the complex on the electronic ground state potential energy surface has a linear hydrogen bonded structure, which is in agreement with theory [34].

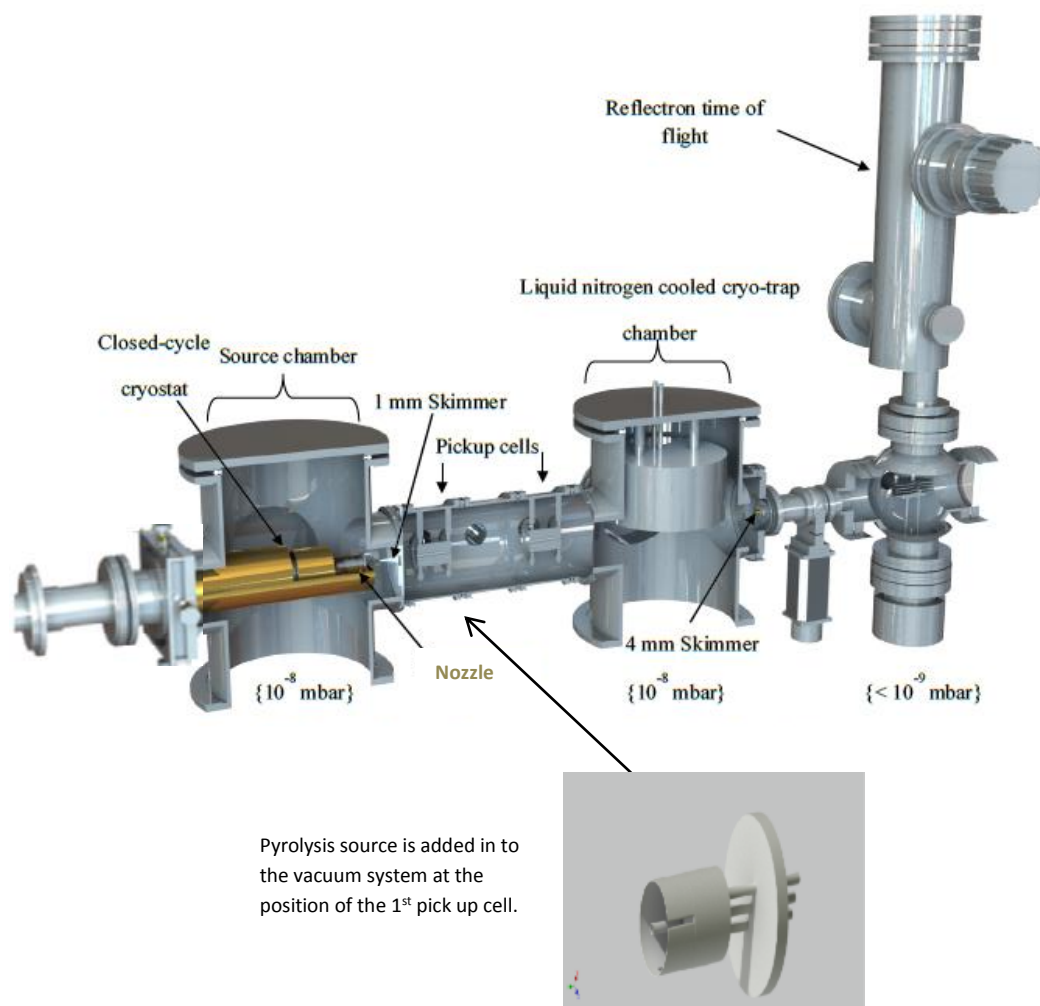
To explore entrance channel complexes involving halogen atoms one must find a way to generate these species. Thermal dissociation is one of the main techniques for generating free radicals for spectroscopic studies [198] and Kohn *et al.* were the first to combine flash pyrolysis with supersonic cooling to produce cold free radicals [199]. Sources with similar designs have subsequently been used to generate a variety of small organic free radicals and transient molecules [200,201]. Merritt *et al.* adapted these ideas to generate a pyrolysis pick-up cell and to make halogen atoms by the thermal dissociation of the corresponding diatomic halogen molecules [198].

In the present work, the original aim was to make complexes of halogen atoms with small organic molecules, which at the time this work was initiated had not been done previously. One such target was I-CH<sub>4</sub>, which would be an entrance channel intermediate in the I + CH<sub>4</sub> → CH<sub>3</sub> + HI reaction. I atoms were the priority because thermal dissociation of I<sub>2</sub> is easier than for the lighter halogen molecules since I<sub>2</sub> thermally dissociates at a lower temperature than the other halogens. However, in the longer term the aim was to extend this work to other halogen atoms and a variety of organic molecules. Unfortunately, the progress made was limited, as will be detailed later, and the primary focus turned out to be a preliminary investigation of iodine clustering with water molecules.

## 7.2 Experimental details

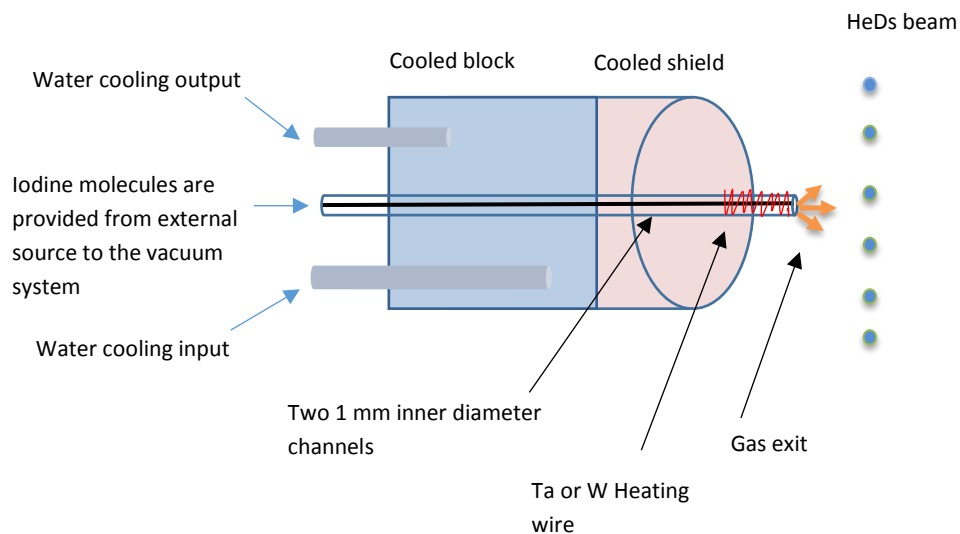
In the current work, two different helium droplet instruments were used. In an attempt to create I atoms from pyrolysis of I<sub>2</sub>, a pyrolysis source was made with a design similar to that used by the Miller group [34,198]. For initial studies, the oldest helium droplet system in the Ellis laboratory was employed, while for spectroscopic work the helium droplet apparatus was the one described in Chapter 2 of this thesis (and hence needs no further description).

Figure 7.1 shows the experimental arrangement used for experiments on the old helium droplet instrument. The helium droplet source chamber is pumped by a large diffusion pump ( $3000 \text{ l s}^{-1}$  pumping speed) and can reach a base pressure of  $10^{-8}$  mbar. A cooled nozzle similar to that used for the other work described in this thesis was employed. The stagnation temperature and pressure employed were 11.2 K and 15 bar, respectively, which should give helium droplets with a mean size of 5000 helium atoms [9]. Once formed the HeDs pass through a skimmer (1 mm aperture) into a second vacuum chamber (pickup chamber) that includes the pyrolysis source. A second pickup cell allows addition of other molecules if desired. Further downstream is a liquid nitrogen trap, which is used to remove condensable trace gases in the chamber, such as water. Finally, the system ends with a time-of-flight mass spectrometer (TOF-MS), which is equipped with an electron ionization source. The TOF-MS was used to make some initial judgements about the performance of the pyrolysis source before it was transferred over to the newer helium droplet system for spectroscopic work.

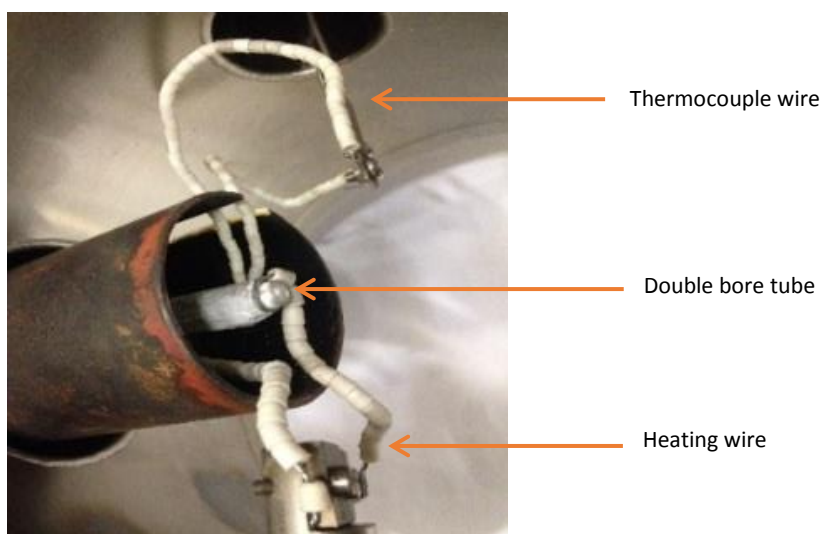


**Figure 7.1.** Overall setup of the old helium droplet system [69] used for initial pyrolysis experiments.

To create I atoms, a pyrolysis source was designed by the author and made by the workshop within the Chemistry Department at the University of Leicester. The design of the pyrolysis source is similar to that used by Miller group [34,198] and is illustrated in Figure 7.2(a).



(a)



(b)

**Figure 7.2.** (a) Simplified illustration of the iodine pyrolysis source. (b) Photograph of the actual arrangement.

The pyrolysis source consists of a rod containing two parallel holes running along its length, each with an inner diameter of 1 mm. The source gas ( $I_2$  vapour) flows through both channels. The rod is made from 99.8 % pure aluminium oxide (alumina). Heating

wire, made from either tantalum or tungsten and having a diameter of 0.25 mm, was wrapped around the tube and then held firmly in place by high thermal conductivity ceramic glue. This arrangement was used to resistively heat the pickup cell via an external power DC supply. The temperature of the cell was measured with a K-type thermocouple, which was attached to the ceramic glue. The cell was mounted via a copper block and a shield around the pickup cell provided water cooling to prevent excessive heating of surrounding chamber walls. . The oven reached a temperature of 1450 K when provided with a voltage of 21 V and 18 A of current.

The pyrolysis source is mounted in a ‘crossed beam’ arrangement, *i.e.* the heated gases travel out of the oven in a direction perpendicular to the direction of travel of the HeD beam. To maximise the pickup probability, the end of the pickup cell was placed close to the HeD beam and was typically only 1 mm away. Determination of this distance was done with the aid of He–Ne alignment laser. Note that the thermal radiation of the pyrolysis source does not directly affect the helium droplets since the latter are transparent to infrared and visible radiation [60].

The doped HeDs exit the pickup region by passing through a second skimmer (4 aperture mm diameter) and eventually reach the ionization region of a TOF-MS (Kore Technology). The ionization source is an electron beam which is operated typically at 70 eV, which is well above the ionization threshold for atomic helium. Any ions produced were detected by a micro-channel plate detector and mass spectra were accumulated via a digital oscilloscope.

In the second part of the experiment, IR depletion spectra were recorded. The apparatus and operational details are essentially the same as described in previous chapters in this thesis, except for the use of the pyrolysis pickup cell.

### **7.3 Computational details**

*Ab initio* calculations were performed to support and explain the experimental results. MP2 theory with aug-cc-pVDZ basis sets was used for this purpose. The calculations

were used to predict possible equilibrium structures of  $I_2(H_2O)$  clusters for reasons that will become clear shortly. Subsequently, IR spectra were predicted using the harmonic approximation. All calculations used Gaussian 03 [202] and were performed on the ALICE HPC system at the University of Leicester.

## 7.4 Results and discussion

### 7.4.1 Thermal dissociation of $I_2$

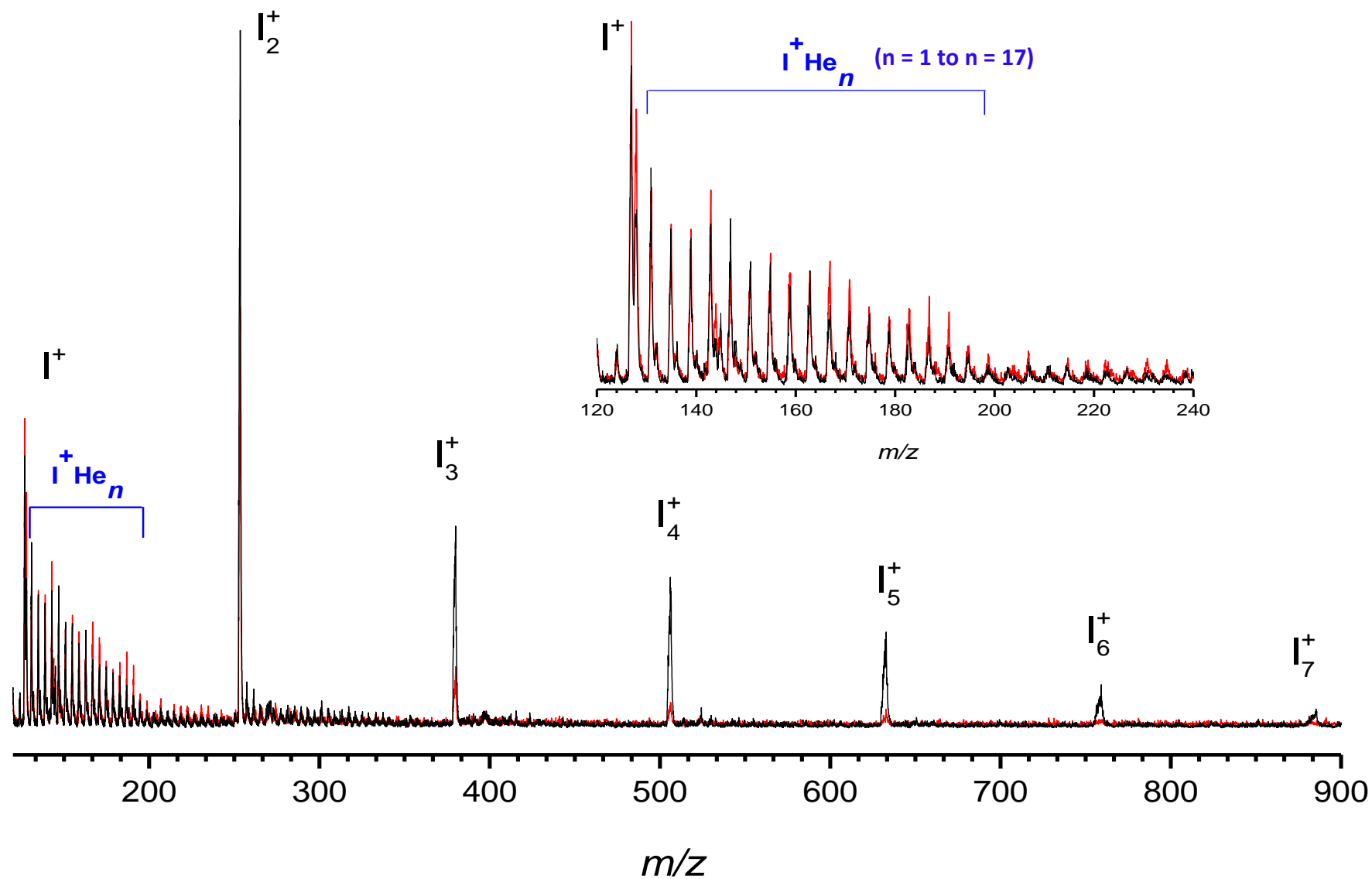
In initial tests of the pyrolysis source, attempts were made to provide evidence for successful thermal dissociation of  $I_2$  molecules into I atoms. We start this section by considering the mass spectrum observed before pyrolysis was carried out and then move on to consider the effect of heating the pickup cell.

The black trace in Figure 7.3 shows a mass spectrum obtained when the pyrolysis cell was at room temperature. The mass spectrum consists of a series of  $I_n^+$  ions starting from  $n = 1$  and extending to beyond  $n = 7$  (the maximum shown in Figure 7.3).  $I_2^+$  clearly gives the strongest signal but other ions are seen, such as  $I^+$  and  $I_3^+$ . The ions with an odd number of I atoms are presumably the result of  $I_2^+$  dissociation after charge transfer from  $He^+$  to  $I_2$  or  $(I_2)_n$  clusters.

Also seen in the room temperature mass spectrum are ions of the type  $I^+He_n$  for  $n = 1 - 17$  and this series is highlighted by the blue label above the spectrum. Note that helium atoms predominantly stick to  $I^+$  ions because molecular ions such as  $I_2^+$  and  $I_3^+$  may be formed with excess rotational and vibrational energy on ionization which results in the evaporation of helium atoms. Note that Silva *et al.* have previously doped HeDs with  $I_2$  and ionised it via free electrons [203]. They observed a series ion mass signals of  $I^+He_n$ ,  $I_2^+He_n$  and  $I_3^+He_n$  [203].

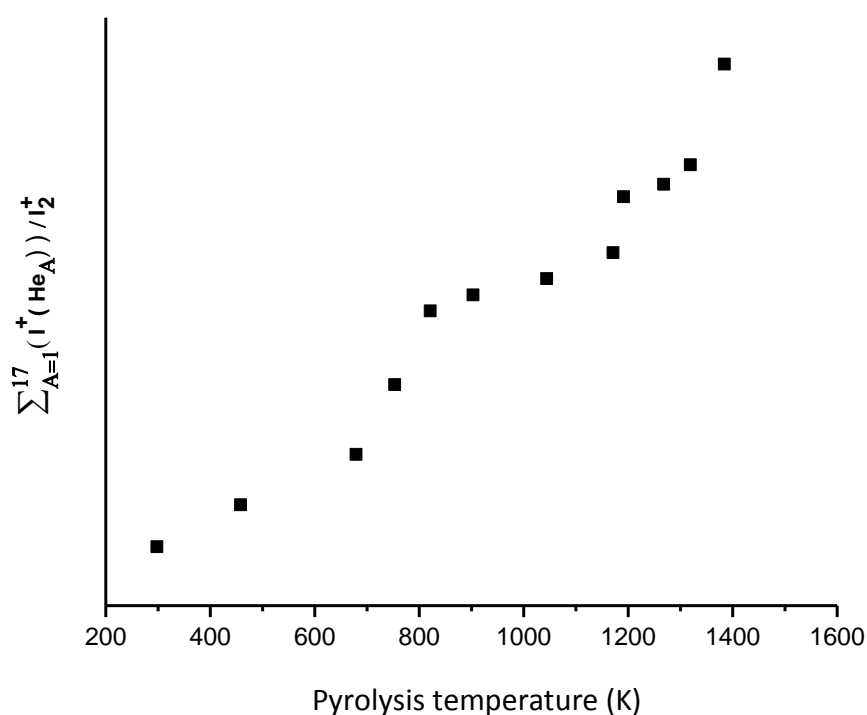
When the temperature of the pyrolysis source was increased from room temperature to 1190 K the mass spectrum shown in red in Figure 7.3 was obtained. The ion signal ( $I^+$ ) at 1190 K is more intense than the signal at room temperature and

this will be discussed shortly. There are significant decline in  $I_n^+$  where  $n \geq 2$  with increasing oven temperature, as shown in Figure 7.3.



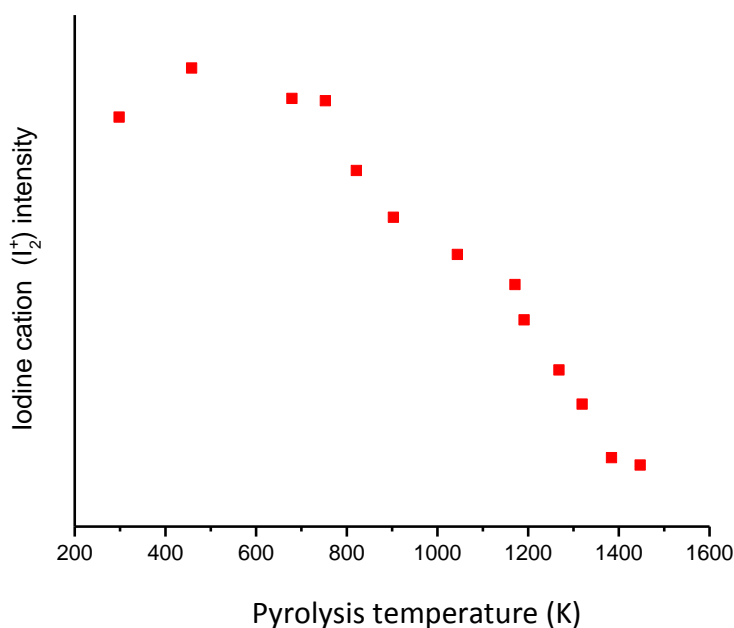
**Figure 7.3.** Mass spectrum obtained for pick of  $I_2$  in helium droplets at room temperature (black line) and at a temperature of 1190 K (red line). The blue line refers to the helium atoms attached to ( $I^+$ ,  $I_2^+$ ,  $I_3^+$ ,.....) while the other iodine ions are not attached to the He atoms.

Figure 7.4 shows how the ratio of  $I^+$  to  $I_2^+$  signals changes with temperature. There is a gradual increase in this ratio as the temperature rises. Note that the  $I^+/I_2^+$  signal ratio is determined by including the effect of temperature on the  $I^+He_n$  signals, *i.e.* including the latter in the net  $I^+$  signal.



**Figure 7.4.** Plot of the  $I^+/I_2^+$  signal ratio as a function of temperature.

The  $I_2^+$  signal declined substantially with rising oven temperature, which causes an increase in the  $I^+/I_2^+$  ratio with temperature. As can be seen in Figure 7.5, a sharp decline begins at a temperature of about 800 K. This observation, coupled with that shown in Figure 7.4, suggests that the pyrolysis source was successfully dissociating  $I_2$  molecules beyond  $\sim 800K$ .



**Figure 7.5.** I<sub>2</sub><sup>+</sup> signal versus temperature.

Although the intensity of I<sup>+</sup> increased with rising temperature up to around 800 K, there is a subsequent decrease at higher temperatures, as shown in Figure 7.6. At temperatures around 800 K a signal attributed to CO<sub>2</sub><sup>+</sup> at  $m/z = 44$  (and therefore below lower limit of mass scan in Figure 7.3) appeared in the mass spectrum and its intensity increased with rising temperature. The signal of CO<sub>2</sub> presumably derives from the oven material and we suspect that pickup of the CO<sub>2</sub> causes shrink of the helium droplets, and hence reduced pickup of I<sub>2</sub>. This may explain why the I<sup>+</sup> signal decreases after reaching its maximum intensity around 800 K. It is this emission of CO<sub>2</sub> which lead to abandonment of these thermal dissociation experiments and a switch to look at complexes from the undissociated I<sub>2</sub> molecule.

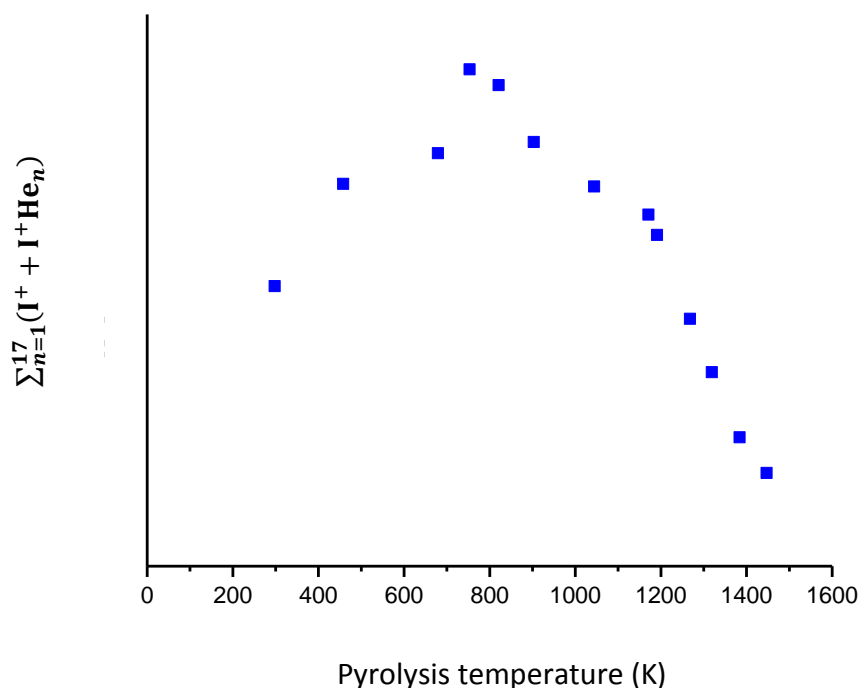


**Figure 7.6.** I<sup>+</sup> signal as a function of temperature.

#### **7.4.2 I<sub>2</sub> + H<sub>2</sub>O complexes**

To find a somewhat simpler target to investigate, complexes between I<sub>2</sub> and water molecules were explored. No previous work has been done on these complexes before and therefore the plan was to focus particularly on I<sub>2</sub>(H<sub>2</sub>O). H<sub>2</sub>O was chosen rather than CH<sub>4</sub> because H<sub>2</sub>O is a much stronger IR absorber and so would represent a good starting point.

##### **7.4.2.1 Mass spectra**

A mass spectrum recorded in the range  $m/z$  8 – 800 is shown in Figure 7.7. This mass spectrum was recorded without adding water to the HeDs via a second pick up cell. The resulting mass spectrum in Figure 7.7 was recorded on the newer helium droplet instrument using a quadrupole mass spectrometer. I<sub>2</sub><sup>+</sup> is the dominant iodine-

containing ion but other ions are seen. Presumably the dominance of  $I_2^+$  implies that most helium droplets pick up only one  $I_2$  molecule.

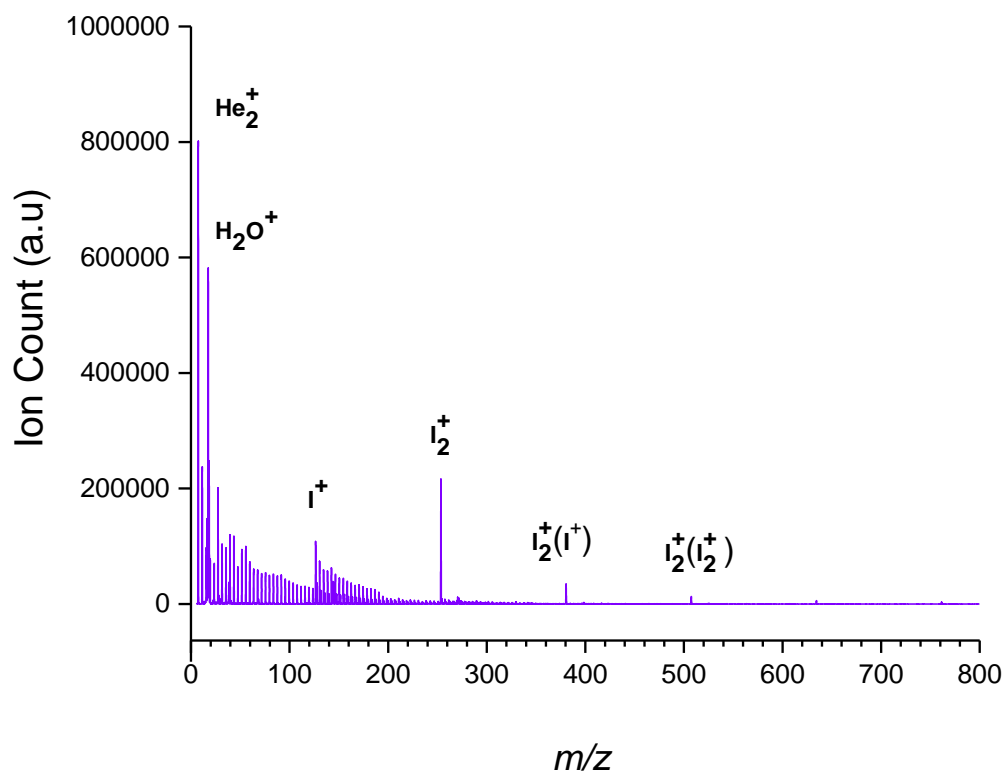


**Figure 7.7.** Mass spectrum of iodine clusters in helium droplets formed at a helium stagnation pressure and temperature of 32 bar and 15 K, respectively.

When water was added to the HeDs, the  $He_2^+$  signal was reduced (see Figure 7.8). This decline in  $He_2^+$  is due to transfer energy from  $H_2O$  to the HeDs which causes evaporation of helium atoms and decreasing cross section ionization of the HeDs. Clearly the  $H_2O^+$  signal increases when water is added and the signal from  $I_n^+$  cluster ions decreases. New ions detected include  $I^+(H_2O)$  at  $m/z = 145$  and  $I_2^+(H_2O)$  at  $m/z = 172$ . The expanded part of Figure 7.8 shows there is another peak at  $m/z = 171$ , which presumably arises from  $I^+(OH)$ . In addition, peaks attributable to  $I_2^+(H_2O)OH$  at  $m/z = 289$  and  $I_2^+(H_2O)_2$  at  $m/z = 290$  can be seen. The latter presumably arise predominantly from the ionization of  $I_2(H_2O)_2$  clusters inside the HeDs.

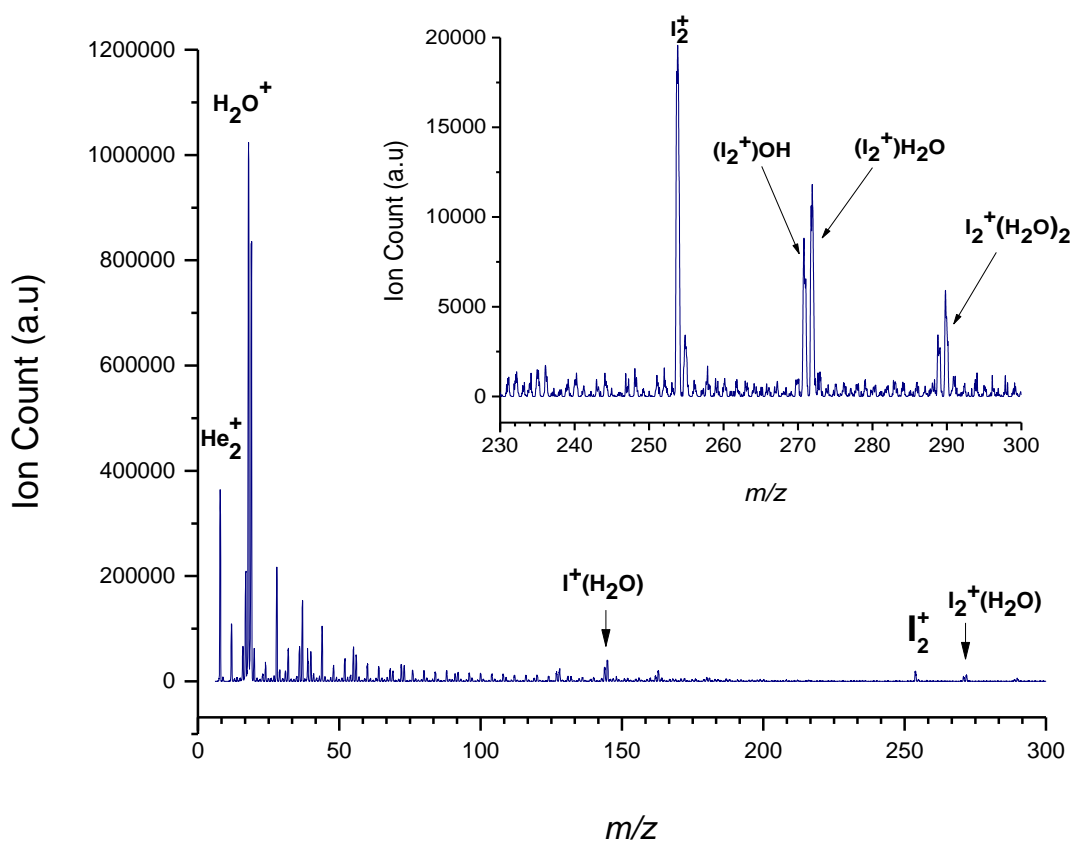


**Figure 7.8.** Mass spectrum of HeDs doped with both water and iodine molecules. Two ion series are highlighted, one from  $I^+(H_2O)_n$  and the other from  $I_2^+(H_2O)_n$ .

Increasing the vapour pressure of the iodine and water molecules generates a wider range of clusters, as illustrated in Figure 7.9. Two series are highlighted (Figure 7.9), one assigned to  $I^+(H_2O)_n$  and the other to  $I_2^+(H_2O)_n$ .

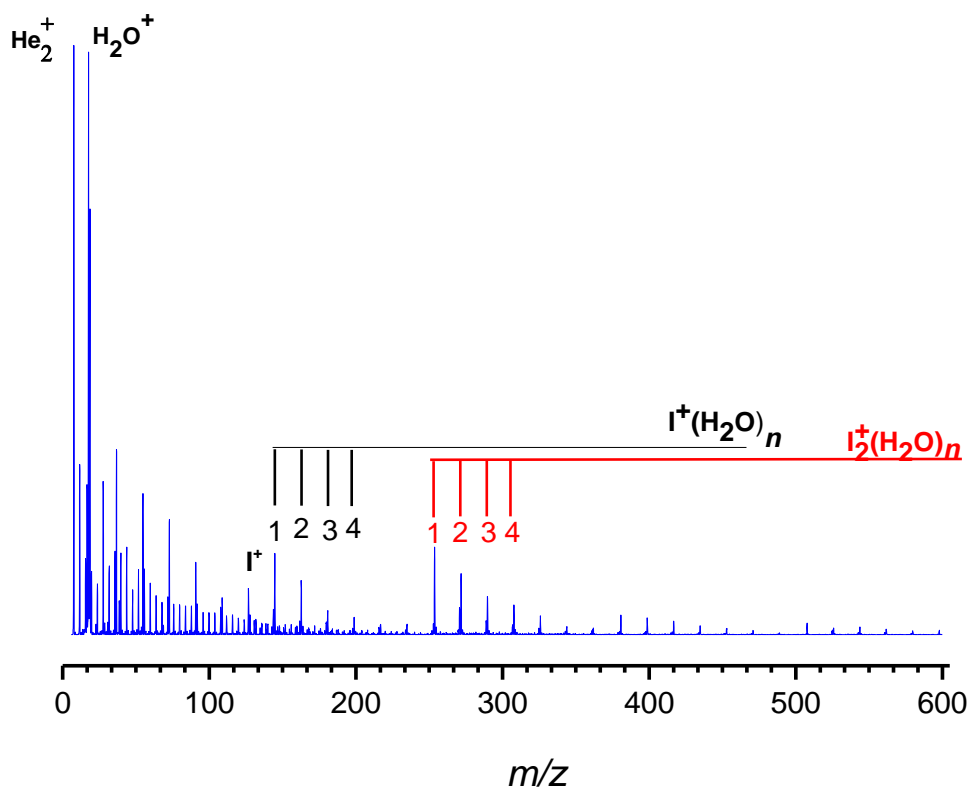


**Figure 7.9.** Mass spectrum recorded for higher dopant pressures than the spectrum shown in Figure 7.8.

#### **7.4.2.2 Infrared spectra of water/iodine complexes**

After measuring the mass spectra, IR spectra in the OH stretching region were recorded. In these experiments the quantity of both iodine and water was kept deliberately low in order to try and maximise production of  $I_2(H_2O)$  at the expense of larger mixed clusters. We recorded depletion spectra by gating ions at  $m/z$  272 ( $(H_2O)_2I^+$ ) and  $m/z$  19 ( $H_3O^+$ ) and these are shown in Figure 7.10 along with predictions from *ab initio* calculations.

*Ab initio* calculations were performed to predict the possible structures of van der Waals complexes between iodine and water molecules. Two different structures were predicted for  $I_2(H_2O)$ . In one of the structures (structure 1), both the water monomer and  $I_2$  are planar, while they are non-planar in the other isomer (structure

2), as shown in Figure 7.11. Structure 1 is lower in energy than structure 2 by 0.0675 eV and has two OH stretching bands at 3575  $\text{cm}^{-1}$  and at 3704  $\text{cm}^{-1}$  with approximately equal intensity. In comparison, structure 2 has two OH stretching bands with very different intensities; the main one at 3735  $\text{cm}^{-1}$  and a lower intensity band at 3607  $\text{cm}^{-1}$ . In addition, ab initio calculations are performed to predict the OH stretching for  $(\text{H}_2\text{O})_2\text{I}_2$ . This calculations help to identify whether there are any IR spectral features due to this larger parent cluster in the spectrum recorded at  $m/z = 272$ , as will be discussed later.

Part of the experimental IR spectrum recorded for pure water at  $m/z = 19$  ( $\text{H}_3\text{O}^+$ ) is shown in Figure 7.10 (black trace). The IR spectrum obtained by detecting  $\text{H}_3\text{O}^+$  is expected to show OH stretching bands of the water dimer and larger water clusters. In the black (pure water) trace there are two peaks in the range of 3710 – 3730  $\text{cm}^{-1}$  region which fit with known peaks of water clusters. The higher frequency peak at 3730  $\text{cm}^{-1}$  is assigned to the water dimer while the lower frequency at 3715  $\text{cm}^{-1}$  has contributions from a variety of water clusters including the dimer [104]. There is no possibility to detect IR spectrum of water monomer at  $m/z = 19$  since this would require data collections at  $m/z = 18$ .

When  $\text{I}_2$  molecules were added to the HeDs, new bands appeared. This is seen in the experimental IR spectrum recorded at  $m/z = 272$  (detecting  $(\text{H}_2\text{O})\text{I}_2^+$ ). The new bands are observed at 3695 and 3575  $\text{cm}^{-1}$  and they disappear when turning to  $m/z = 290$   $(\text{H}_2\text{O})_2\text{I}_2^+$ . This suggests that both peaks derive from IR absorption by the  $(\text{H}_2\text{O})\text{I}_2$  complexes with just one  $\text{H}_2\text{O}$  molecules in cluster. It is emphasised that the IR spectrum at  $m/z = 272$  was recorded with a deliberately low water partial pressure and therefore the dominant contribution should come from a single water molecule in combination with  $\text{I}_2$ , i.e. from  $\text{I}_2(\text{H}_2\text{O})$ . However, there are two peaks in the spectrum recorded at  $m/z = 272$ , namely at 3715 and 3710  $\text{cm}^{-1}$ , which are in same position as peaks observed in the pure water ( $m/z = 19$ ) spectrum. Assignment of these peaks has not been made. In addition there is a peak at 3615  $\text{cm}^{-1}$  in IR spectrum at  $m/z = 272$  which we could not assign.

A comparison between the experimental and theoretical IR spectra assists in the assignment of the  $I_2(H_2O)$  parent cluster to either structure 1 or 2. Figure 7.10 indicates a calculated OH stretch level for structure 1 at  $3704\text{ cm}^{-1}$  (blue line), which is in close agreement with the experimental peak at  $3695\text{ cm}^{-1}$ . In addition, there is good agreement between the frequencies of the calculated and experimental IR frequencies for the OH stretch at  $3575\text{ cm}^{-1}$ . Therefore, the new bands can both be assigned to OH stretching of  $(H_2O)_I_2$  of structure 1. In addition, theoretical calculations of  $(H_2O)_2I_2$  (Figure 7.10, green lines) shows that the frequencies of OH vibration stretch levels are far from the IR peaks observed in the spectrum for  $m/z = 272$ . This provides evidence that the observed experimental peaks do not originate from clusters larger than  $I_2(H_2O)$ .

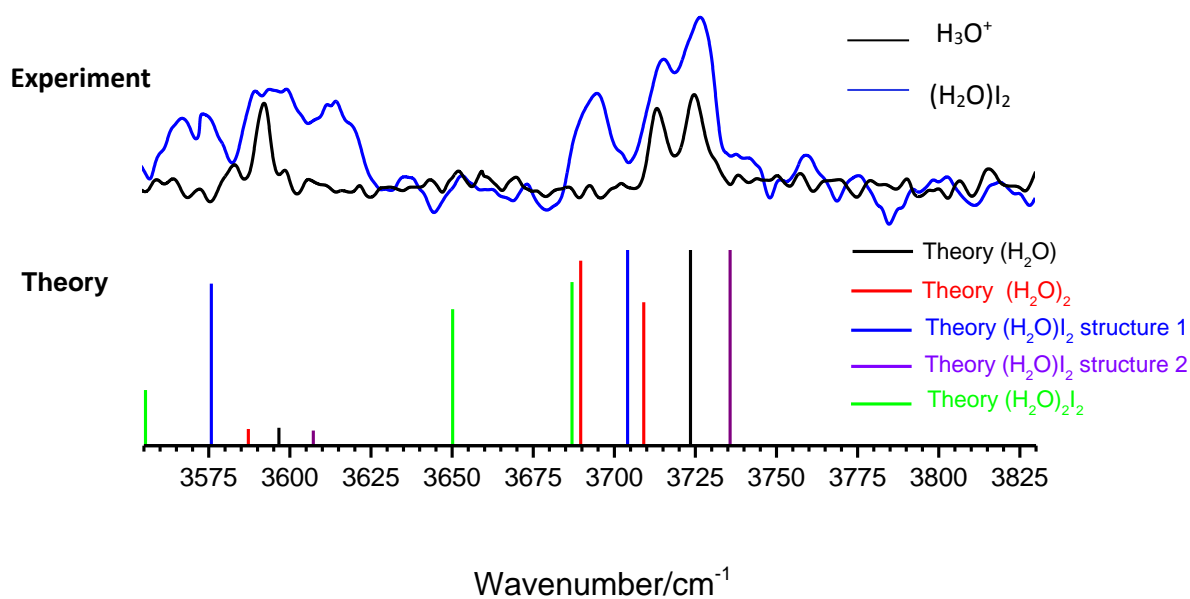


**Figure 7.10.** Depletion IR spectra recorded at  $m/z = 19$  ( $H_2OH^+$ ) (black curve) when the HeDs were doped with only pure water, and IR spectrum at  $m/z = 272$  ( $(H_2O)I_2^+$ ) (blue curve) when HeDs are doped with both water molecules and iodine. In the stick diagram at the bottom are scaled harmonic predictions for the water monomer (black line), the water dimer (red line), structure 1 of  $I_2(H_2O)$  (blue line), structure 2 of  $I_2(H_2O)$  (purple line) and  $(H_2O)_2I_2$  (green line).



(a) Structure 1

(b) Structure 2

**Figure 7.11.**  $(\text{H}_2\text{O})\text{I}_2$  isomers. (a) In structure 1 both water and iodine molecules are planar while (b) in structure 2  $\text{H}_2\text{O}$  and  $\text{I}_2$  are non-planar.

## 7.5 Conclusions

The original aim of the work was to record entrance channel complexes derived from the  $\text{I} + \text{CH}_4 \rightarrow \text{CH}_3 + \text{HI}$  reaction. In practice these experiments were not performed due to contaminating emission of  $\text{CO}_2$  from the heated pyrolysis cell. Consequently, attention switched to the  $\text{I}_2(\text{H}_2\text{O})$  complex.

In the second part of the current work, the pyrolysis source was not used and, instead, the IR spectrum of the OH stretching region for  $(\text{H}_2\text{O})\text{I}_2$  at  $m/z = 272$  is recorded. The resulting IR spectrum was compared with that measured for the OH stretching region of pure water of  $(\text{H}_2\text{O})_2$  at  $m/z = 19$ . The comparison showed two additional peaks at  $3695 \text{ cm}^{-1}$  and at  $3575 \text{ cm}^{-1}$  in the IR spectrum recorded at mass channel 272 that were not observed for pure water, and which disappeared in IR spectra at a higher mass channel corresponding to detection of  $(\text{H}_2\text{O})_2\text{I}_2^+$ . This shows that the experimental IR peaks can be assigned to  $(\text{H}_2\text{O})\text{I}_2$  parent molecules. Scaled harmonic calculations were performed to support the experimental results. The calculations predicted two different isomers of  $(\text{H}_2\text{O})\text{I}_2$ . In one of these structures, both

iodine and water molecule are planar (structure 1) and the calculated IR frequencies for the structure 1 are in the best agreement of the two possible structures explored here with experimental spectra measured in the OH stretching region of  $(\text{H}_2\text{O})\text{I}_2$ . For the other structure (structure 2),  $\text{I}_2$  and  $\text{H}_2\text{O}$  are non-planar and there is poor agreement between the calculated and experimental IR frequencies, indicating that the structure of the parent molecules corresponds to structure 1 and not 2. This work is preliminary and would require much more work to generate a publishable paper.

## Chapter 8

### 8.1 Thesis Summary

This thesis has focused on the spectroscopic study of molecular clusters in helium droplets. The low temperature and superfluidity make HeDs a unique environment for molecular aggregation. As the dopants are added to the HeDs, the high thermal conductivity rapidly cools the dopants to the helium steady-state temperature, 0.37 K. In some cases this can lead to the formation and trapping of molecular clusters with different structures from those in the gas phase.

In Chapter 3, OH stretching of heptamer and octamer water clusters are recorded via depletion spectroscopy for first time in HeDs in OH stretching region. This has been done through adding low amount of water molecules to the HeDs. Theoretical calculations at the MP2/aug-ccpVDZ level predicted cyclic structures for the OH spectra of experimental work. Evidence of the heptamer water cluster was observed from previous study [103] of observing OH stretching of hexamer water cluster in HeDs. This was suggested that the OH stretching of  $(\text{H}_2\text{O})_7$  could be covered via OH stretching of the higher water clusters since mass selectivity was not used in the earlier study.

In Chapter 4, IR spectra of large water clusters  $(\text{H}_2\text{O})_n$  ( $n = 11 - 21$ ) were described in the OH stretching region. The intensity maximum in these spectra shows a blue shift from  $n = 11$  to  $n = 17$ , while it shows red shift for even larger water clusters. The free OH stretching region in these spectra shows two peaks, which indicates that two different environments occur for the water molecules: 2-coordinate (AD) and 3-coordinate (AAD) molecules.

In Chapter 5, IR spectra of methanol clusters were recorded in the OH stretching of both  $(\text{CH}_3\text{OH})_3$  and  $(\text{CH}_3\text{OH})_4$  are recorded in OH region in HeDs. *Ab initio* calculations support the experimental OH stretching spectra and predict cyclic structures of both clusters. There was no any evidence of branched cyclic structures of methanol clusters in HeDs which was observed in a previous study in CO stretching region [173].

In chapter 6, IR spectra of  $(\text{CH}_3\text{OH})_2\text{H}_2\text{O}$  and  $(\text{CH}_3\text{OH})_3\text{H}_2\text{O}$  were reported for the first time successfully. The spectra are consistent with cyclic structures and this is fully supported by predictions from electronic structure calculations.

In Chapter 7, two parts of work had been done. The first part of this work included dissociation of iodine molecules via pyrolysis source, and OH stretching of the water molecules in  $\text{I}_2(\text{H}_2\text{O})$  are observed in the second part of this work at  $m/z$  of  $\text{I}_2(\text{H}_2\text{O})$ . Theoretical calculations predicated structure of  $\text{I}_2(\text{H}_2\text{O})$  as both iodine molecule and water are planar. This work required more work to obtain valuable results for publishing.

## 8.2 Future work

It is possible to extend the experiments on water clusters further to find structures of  $(\text{H}_2\text{O})_9$  and  $(\text{H}_2\text{O})_{10}$  in HeDs since we observed IR spectra of both  $(\text{H}_2\text{O})_7$  and  $(\text{H}_2\text{O})_8$  in the present research. This will help to determine if the cyclic structure is the only structure of water clusters in HeDs, or if the water molecules will arrange into a different structure within clusters in HeDs for  $n > 8$ . However, the challenge is that it might be not easy to distinguish IR spectra of these sized cluster from each other, even with mass selectivity.

A study of the stability of the cyclic structures of water clusters in HeDs could be done via adding hydrogen to water and see how  $\text{H}_2$  molecule affect the cyclic water structures ( $n = 6, 7, 8$ ) and the strain of H-bonds. This experimental work would be similar to the other experiments in the present work.

In addition, experiments of mixtures of  $\text{CH}_3\text{OH}/\text{H}_2\text{O}$  could be extended in future to study monomer water molecule with methanol clusters larger than the current observed maximum of  $(\text{CH}_3\text{OH})_3$ . New work could be done on mixtures of water/methanol to study and understand the negative entropy of the mixture [204]. Current work on methanol/water mixtures shows that there is no segregation in the mixture at very low ratios of water to methanol. On the other hand, it could be there is segregation if the amounts of both water and methanol are equal in the clusters, i.e.

$(\text{CH}_3\text{OH})_n(\text{H}_2\text{O})_n$ . Therefore it will be interesting to study clusters with this equi-molar composition.

Since there was success in detecting IR spectra of the water monomer attached to  $\text{I}_2$ , it should also be possible to detect IR spectra of  $\text{I}_2(\text{H}_2\text{O})_n$  for  $n > 1$  and study their intermolecular interactions. Equally, since we observed good thermal dissociation of  $\text{I}_2$ , the possibility of studying  $\text{I}(\text{H}_2\text{O})$  ought to be pursued.

## Publications

### *Paper*

**Media I. Sulaiman**, Shengfu Yang, and Andrew M. Ellis. "Infrared Spectroscopy of Methanol and Methanol/Water Clusters in Helium Nanodroplets: The OH Stretching Region." *Journal of Physical Chemistry A* 121, no. 4 (2017): 771-776.

### *Talk*

Cyclic Water Heptamer. **Media I. Sulaiman**, Gautam Sarma, Andrew Ellis. RSC (Spectroscopy and Dynamics Group) conference, UK, 5<sup>th</sup>-7<sup>th</sup> of January 2016.

### *Poster*

Freezing complex in helium nanodroplets: a unique tool for Chemical Dynamics. **Media I. Sulaiman**, Gautam Sarma & Prof. Andrew M. Ellis. Post Graduate Research Festival 2015, University of Leicester, Chemistry department.

## Bibliography

- 1 Masters BR. A brief history of spectral analysis and astrospectroscopy. *OPN*. 2009, **20**, 134-9.
- 2 Anderson JB, Traynor CA, Boghosian BM. An exact quantum Monte Carlo calculation of the helium–helium intermolecular potential. *J. Chem. Phys.* 1993, **99**, 345-51.
- 3 Keesom WH, Taconis KW. On the structure of solid helium. *Physica*. 1938, **5**, 161-9.
- 4 Pekeris CL. The Zero-Point Energy of Helium. *Phys. Rev.* 1950, **79**, 884.
- 5 Chin SA, Krotscheck E. Systematics of pure and doped He 4 clusters. *Phys. Rev. B*. 1995, **52**, 10405.
- 6 Rama Krishna MV, Whaley KB. Wave functions of helium clusters. *J. Chem. Phys.* 1990, **93**, 6738-51.
- 7 Lewerenz M. Structure and energetics of small helium clusters: Quantum simulations using a recent perturbational pair potential. *J. Chem. Phys.* 1997, **106**, 4596-603.
- 8 Annett JF. Superconductivity, superfluids and condensates. *Oxford University Press*, 2004, **5**.
- 9 Gomez LF, Loginov E, Sliter R, Vilesov AF. Sizes of large He droplets. *J. Chem. Phys.* 2011, **135**, 154201.
- 10 London F. On the Bose-Einstein condensation. *Phys. Rev.* 1938, **54**, 947.
- 11 Onnes HK. The liquefaction of helium. *Koninklijke Nederlandse Akademie van Wetenschappen, Proceedings*. 1908, **11**, 1908-9.
- 12 McLennan JC, Smith HD, Wilhelm JO. XIV. The scattering of light by liquid helium. *Philos. Mag.* 1932, **14**, 161-7.

- 13 Keesom WH, Keesom AP. New measurements on the specific heat of liquid helium. *Physica*. 1935, **2**, 557-72.
- 14 Allen JF, Misener AD. Flow of liquid helium II. *Nature*. 1938, **141**, 75.
- 15 Kapitza P. Viscosity of liquid helium below the  $\lambda$ -point. *Nature*, 1938, **141**, 74.
- 16 Tisza L. The theory of liquid helium. *Phys. Rev.* 1947, **72**, 838.
- 17 Andronikashvili EL. A direct observation of two kinds of motion in helium II. *J. Phys. (USSR)*, 1946, **10**, 201.
- 18 Landau L. Theory of the Superfluidity of Helium II. *Phys. Rev.* 1941, **60**, 356.
- 19 Landau L. On the theory of superfluidity of Helium II. *J. Phys. (USSR)*, 1947, **11**, 91.
- 20 Allum DR, McClintock PV, Phillips A. The Breakdown of Superfluidity in Liquid  $^4\text{He}$ : An Experimental Test of Landau's Theory. *Phil. Trans. R. Soc. A.* 1977, **284**, 179-224.
- 21 Toennies JP, Vilesov AF. Superfluid helium droplets: a uniquely cold nanomatrix for molecules and molecular complexes. *Angew. Chem. Int. Ed.* 2004, **43**, 2622-48.
- 22 Becker EW, Klingelhöfer R, Lohse P. Strahlen aus kondensiertem Helium im Hochvakuum. *Z. Naturforsch. A.* 1961, **16**, 1259.
- 23 Scheidemann A, Schilling B, Toennies JP, Northby JA. Capture of foreign atoms by helium clusters. *Physica B.* 1990, **165**, 135-6.
- 24 Scheidemann A, Toennies JP, Northby JA. Capture of neon atoms by  $\text{He}_4$  clusters. *Phys. Rev. Lett.* 1990, **64**, 1899.
- 25 Buchenau H, Toennies JP, Northby JA. Excitation and ionization of  $\text{He}_4$  clusters by electrons. *J. Chem. Phys.* 1991, **95**, 8134-48.

- 26 Lewerenz M, Schilling B, Toennies JP. A new scattering deflection method for determining and selecting the sizes of large liquid clusters of 4He. *Chem. Phys. Lett.* 1993, **206**, 381-7.
- 27 Brühl R, Guardiola R, Kalinin A, Kornilov O, Navarro J, Savas T, Toennies JP. Diffraction of neutral helium clusters: Evidence for “magic numbers”. *Phys. Rev. Lett.* 2004, **92**, 185301.
- 28 Kanaev AV, Museur L, Laarmann T, Monticone S, Castex MC, von Haeften K, Möller T. Dissociation and suppressed ionization of H<sub>2</sub>O molecules embedded in He clusters: the role of the cluster as a cage. *J. Chem. Phys.* 2001, **115**, 10248-53.
- 29 Vongehr S, Shao-Chun T, Xiang-Kang M. Collision statistics of clusters: from Poisson model to Poisson mixtures. *Chin. Phys. B.* 2010, **19**, 023602.
- 30 Henne U, Toennies JP. Electron capture by large helium droplets. *J. Chem. Phys.* 1998, **108**, 9327-38.
- 31 Yang S, Ellis AM, Spence D, Feng C, Boatwright A, Latimer E, Binns C. Growing metal nanoparticles in superfluid helium. *Nanoscale.* 2013, **5**, 11545-53.
- 32 Lewerenz M, Schilling B, Toennies JP. Successive capture and coagulation of atoms and molecules to small clusters in large liquid helium clusters. *J. Chem. Phys.* 1995, **102**, 8191-207.
- 33 Toennies JP, Vilesov AF. Spectroscopy of atoms and molecules in liquid helium. *Annu. Rev. Phys. Chem.* 1998, **49**, 1-41.
- 34 Merritt JM, Küpper J, Miller RE. Entrance channel X–HF (X= Cl, Br and I) complexes studied by high-resolution infrared laser spectroscopy in helium nanodroplets. *Phys. Chem. Chem. Phys.* 2005, **7**, 67-78.
- 35 Sadoon AM, Sarma G, Cunningham EM, Tandy J, Hanson-Heine MW, Besley NA, Yang S, Ellis AM. Infrared spectroscopy of NaCl (CH<sub>3</sub>OH)<sub>n</sub> complexes in helium nanodroplets. *J. Phys. Chem. A.* 2016, **120**, 8085-92.

- 36 Tandy J, Feng C, Boatwright A, Sarma G, Sadoon AM, Shirley A, Das Neves Rodrigues N, Cunningham EM, Yang S, Ellis AM. Communication: Infrared spectroscopy of salt-water complexes. *J. Chem. Phys.* 2016, **144**, 121103.
- 37 Bartelt A, Close JD, Federmann F, Quaas N, Toennies JP. Cold metal clusters: Helium droplets as a nanoscale cryostat. *Phys. Rev. Lett.* 1996, **77**, 3525.
- 38 Mudrich M, Forkl B, Müller S, Dvorak M, Bünermann O, Stienkemeier F. Kilohertz laser ablation for doping helium nanodroplets. *Rev. Sci. Instrum.* 2007, **78**, 103106.
- 39 Jeffs J, Besley NA, Stace AJ, Sarma G, Cunningham EM, Boatwright A, Yang S, Ellis AM. Metastable Aluminum Atoms Floating on the Surface of Helium Nanodroplets. *Phys. Rev. Lett.* 2015, **114**, 233401.
- 40 Claas P, Mende SO, Stienkemeier F. Characterization of laser ablation as a means for doping helium nanodroplets. *Rev. Sci. Instrum.* 2003, **74**, 4071-6.
- 41 Goyal S, Schutt DL, Scoles G. Vibrational spectroscopy of sulfur hexafluoride attached to helium clusters. *Phys. Rev. Lett.* 1992, **69**, 933.
- 42 Barnett RN, Whaley KB. Molecules in helium clusters: SF<sub>6</sub>He N. *J. Chem. Phys.* 1993, **99**, 9730-44.
- 43 Krotscheck E, Chin SA. The delocalization of SF<sub>6</sub> in helium clusters. *Chem. Phys. Lett.* 1994, **227**, 143-8.
- 44 Hartmann M, Miller RE, Toennies JP, Vilesov A. Rotationally Resolved Spectroscopy of S F 6 in Liquid Helium Clusters: A Molecular Probe of Cluster Temperature. *Phys. Rev. Lett.* 1995, **75**, 1566.
- 45 Ancilotto F, Lerner PB, Cole MW. Physics of solvation. *Low Temp. Phys.* 1995, **101**, 1123-46.
- 46 Stienkemeier F, Higgins J, Ernst WE, Scoles G. Laser spectroscopy of alkali-doped helium clusters. *Phys. Rev. Lett.* 1995, **74**, 3592.

- 47 Higgins J, Callegari C, Reho J, Stienkemeier F, Ernst WE, Lehmann KK, Gutowski M, Scoles G. Photoinduced chemical dynamics of high-spin alkali trimers. *Science*. 1996, **273**, 629-31.
- 48 Reho JH, Higgins J, Nooijen M, Lehmann KK, Scoles G, Gutowski M. Photoinduced nonadiabatic dynamics in quartet Na<sub>3</sub> and K<sub>3</sub> formed using helium nanodroplet isolation. *J. Chem. Phys.* 2001, **115**, 10265-74.
- 49 Tiggesbäumker J, Stienkemeier F. Formation and properties of metal clusters isolated in helium droplets. *Phys. Chem. Chem. Phys.* 2007, **9**, 4748-70.
- 50 Stark C, Kresin VV. Critical sizes for the submersion of alkali clusters into liquid helium. *Phys. Rev. B.* 2010, **81**, 085401.
- 51 An der Lan L, Bartl P, Leidlmair C, Schöbel H, Jochum R, Denifl S, Märk TD, Ellis AM, Scheier P. The submersion of sodium clusters in helium nanodroplets: Identification of the surface→ interior transition. *J. Chem. Phys.* 2011, **135**, 044309.
- 52 Douberly GE, Miller RE. Rotational Dynamics of HCN– M (M= Na, K, Rb, Cs) van der Waals Complexes Formed on the Surface of Helium Nanodroplets. *J. Phys. Chem. A.* 2007, **111**, 7292-302.
- 53 Navarro J, Mateo D, Barranco M, Sarsa A. Mg impurity in helium droplets. *J. Chem. Phys.* 2012, **136**, 054301.
- 54 Denifl S, Zappa F, Mähr I, Mauracher A, Probst M, Urban J, Mach P, Bacher A, Bohme DK, Echt O, Märk TD. Ionization of doped helium nanodroplets: Complexes of C<sub>60</sub> with water clusters. *J. Chem. Phys.* 2010, **132**, 234307.
- 55 Shepperson B, Liu J, Ellis AM, Yang S. Ionization of doped helium nanodroplets: residual helium attached to diatomic cations and their clusters. *J. Phys. Chem. A.* 2011, **115**, 7010-6.
- 56 Yang S, Brereton SM, Nandhra S, Ellis AM, Shang B, Yuan LF, Yang J. Electron impact ionization of water-doped superfluid helium nanodroplets: Observation of He(H<sub>2</sub>O)<sub>n</sub><sup>+</sup> clusters. *J. Chem. Phys.* 2007, **127**, 134303.

- 57 Yang S, Brereton SM, Wheeler MD, Ellis AM. Electron impact ionization of haloalkanes in helium nanodroplets. *J. Phys. Chem. A*. 2006, **110**, 1791-7.
- 58 Spence D, Latimer E, York W, Boatwright A, Feng C, Yang S, Ellis AM. Formation of aluminium clusters in helium nanodroplets. *Int. J. Mass Spectrom.* 2014, **365**, 86-8.
- 59 Martini K, Toennies JP, Winkler C. Electron scattering from 4He and Ne clusters: determination of the cluster density from the electronic surface barrier potential. *Chem. Phys. Lett.* 1991, **178**, 429-34.
- 60 Yang S, Ellis AM. Helium droplets: a chemistry perspective. *Chem. Soc. Rev.* 2013, **42**, 472-84.
- 61 Al-Hagan O, Kaiser C, Madison D, Murray AJ. Atomic and molecular signatures for charged-particle ionization. *Nature Physics*. 2009, **5**, 59-63.
- 62 Shepperson B, Liu J, Ellis AM, Yang S. Communication: The formation of helium cluster cations following the ionization of helium nanodroplets: Influence of droplet size and dopant. *J. Chem. Phys.* 2011, **135**, 041101
- 63 Ellis AM, Yang S. Model for the charge-transfer probability in helium nanodroplets following electron-impact ionization. *Phys. Rev. A*. 2007, **76**, 032714.
- 64 Halberstadt N, Janda KC. The resonant charge hopping rate in positively charged helium clusters. *Chem. Phys. Lett.* 1998, **282**, 409-12.
- 65 Seong J, Janda KC, Halberstadt N, Spiegelmann F. Short-time charge motion in He  $n^+$  clusters. *J. Chem. Phys.* 1998, **109**, 10873-84.
- 66 Choi MY, Douberly GE, Falconer TM, Lewis WK, Lindsay CM, Merritt JM, Stiles PL, Miller RE. Infrared spectroscopy of helium nanodroplets: novel methods for physics and chemistry. *Int. Rev. Phys. Chem.* 2006, **25**, 15-75.
- 67 Goyal S, Schutt DL, Scoles G. Infrared spectroscopy in highly quantum matrixes: vibrational spectrum of sulfur hexafluoride ((SF<sub>6</sub>) n= 1, 2) attached to helium clusters. *J. Phys. Chem.* 1993, **97**, 2236-45.

- 68 Fröchtenicht R, Toennies JP, Vilesov A. High-resolution infrared spectroscopy of SF<sub>6</sub> embedded in He clusters. *Chem. Phys. Lett.* 1994, **29**, 1-7.
- 69 Shepperson B. *Helium Droplets: Unique Nanoreactors for the Investigation of Molecular Dopants*. Diss. University of Leicester, 2013.
- 70 Svelto, Orazio, and David C. Hanna. *Principles of lasers*. New York: Plenum press, **4**, 1998.
- 71 Foth HJ. Principles of lasers. Lackner M. *Weinheim: Wiley-VCH*. 2008.
- 72 Duarte FJ. Tunable lasers handbook. 1996, *Academic Press*.
- 73 Dyke TR, Mack KM, Muenter JS. The structure of water dimer from molecular beam electric resonance spectroscopy. *J. Chem. Phys.* 1977, **66**, 498-510.
- 74 Vernon MF, Krajnovich DJ, Kwok HS, Lisy JM, Shen YR, Lee YT. Infrared vibrational predissociation spectroscopy of water clusters by the crossed laser-molecular beam technique. *J. Chem. Phys.* 1982, **77**, 47-57.
- 75 Knochenmuss R, Leutwyler S. Structures and vibrational spectra of water clusters in the self-consistent-field approximation. *J. Chem. Phys.* 1992, **96**, 5233-44.
- 76 Xantheas SS, Dunning Jr TH. Ab initio studies of cyclic water clusters (H<sub>2</sub>O)<sub>n</sub>, n= 1– 6. Optimal structures and vibrational spectra. *J. Chem. Phys.* 1993, **99**, 8774-92.
- 77 Tsai CJ, Jordan KD. Theoretical study of the (H<sub>2</sub>O)<sub>6</sub> cluster. *Chem. Phys. Lett.* 1993, **213**, 181-8.
- 78 Watanabe T, Ebata T, Tanabe S, Mikami N. Size-selected vibrational spectra of phenol-(H<sub>2</sub>O)<sub>n</sub> (n= 1–4) clusters observed by IR–UV double resonance and stimulated Raman-UV double resonance spectroscopies. *J. Phys. Chem.* 1996, **105**, 408-19.
- 79 Liu K, Brown MG, Cruzan JD, Saykally RJ. Vibration-rotation tunneling spectra of the water pentamer: Structure and dynamics. *Science*. 1996, 62-4.

- 80 Fröchtenicht R, Kaloudis M, Koch M, Huisken F. Vibrational spectroscopy of small water complexes embedded in large liquid helium clusters. *J. Chem. Phys.* 1996, **105**, 6128-40.
- 81 Huisken F, Kaloudis M, Kulcke A. Infrared spectroscopy of small size-selected water clusters. *J. Chem. Phys.* 1996, **104**, 17-25.
- 82 Liu K, Brown MG, Carter C, Saykally RJ, Gregory JK, Clary DC. Characterization of a cage form of the water hexamer. *Nature.* 1996, **381**, 501-3.
- 83 Gruenloh CJ, Carney JR, Arrington CA, Zwier TS, Fredericks SY, Jordan KD. Infrared spectrum of a molecular ice cube: the S<sub>4</sub> and D<sub>2d</sub> water octamers in benzene-(water)<sub>8</sub>. *Science*, 1997, **276**, 1678-81
- 84 Gruenloh CJ, Carney JR, Hagemeister FC, Arrington CA, Zwier TS, Fredericks SY, Wood III JT, Jordan KD. Resonant ion-dip infrared spectroscopy of the S<sub>4</sub> and D<sub>2d</sub> water octamers in benzene-(water)<sub>8</sub> and benzene 2-(water)<sub>8</sub>. *J. Phys. Chem.* 1998, **109**, 6601-14.
- 85 Janzen C, Spangenberg D, Roth W, Kleineremanns K. Structure and vibrations of phenol (H<sub>2</sub>O)<sub>7,8</sub> studied by infrared-ultraviolet and ultraviolet-ultraviolet double-resonance spectroscopy and ab initio theory. *J. Phys. Chem.* 1999, **110**, 9898-907.
- 86 Brudermann J, Melzer M, Buck U, Kazimirski JK, Sadlej J, Bush V. The asymmetric cage structure of (H<sub>2</sub>O)<sub>7</sub> from a combined spectroscopic and computational study. *J. Chem. Phys.* 1999, **110**, 10649-52.
- 87 Gruenloh CJ, Carney JR, Hagemeister FC, Zwier TS, Wood III JT, Jordan KD. Resonant ion-dip infrared spectroscopy of benzene-(water)<sub>9</sub>: Expanding the cube. *J. Chem. Phys.* 2000, **113**, 2290-303.
- 88 Andersson P, Steinbach C, Buck U. Vibrational spectroscopy of large water clusters of known size. *Eur. Phys. J. D.* 2003, **24**, 53-6.

- 89 Keutsch FN, Cruzan JD, Saykally RJ. The water trimer. *Chem. Rev.* 2003, **103**, 2533-78.
- 90 Diken EG, Robertson WH, Johnson MA. The vibrational spectrum of the neutral (H<sub>2</sub>O)<sub>6</sub> precursor to the "Magic"(H<sub>2</sub>O)<sub>6</sub>-cluster anion by Argon-mediated, population-modulated electron attachment spectroscopy. *J. Phys. Chem. A.* 2004,**108**, 64-8.
- 91 Harker HA, Viant MR, Keutsch FN, Michael EA, McLaughlin RP, Saykally RJ. Water pentamer: characterization of the torsional-puckering manifold by terahertz VRT spectroscopy. *J. Chem. Phys. A.* 2005, **109**, 6483-97.
- 92 Lin W, Han JX, Takahashi LK, Harker HA, Keutsch FN, Saykally RJ. Terahertz vibration-rotation-tunneling spectroscopy of the water tetramer-d<sub>8</sub>: Combined analysis of vibrational bands at 4.1 and 2.0 THz. *J. Chem. Phys.* 2008, **128**, 094302.
- 93 Shields RM, Temelso B, Archer KA, Morrell TE, Shields GC. Accurate predictions of water cluster formation, (H<sub>2</sub>O)<sub>n</sub> = 2– 10. *J. Phys. Chem. A.* 2010, **114**, 11725-37.
- 94 Pérez C, Muckle MT, Zaleski DP, Seifert NA, Temelso B, Shields GC, Kisiel Z, Pate BH. Structures of cage, prism, and book isomers of water hexamer from broadband rotational spectroscopy. *Science.* 2012, **336**, 897-901.
- 95 Pérez C, Lobsiger S, Seifert NA, Zaleski DP, Temelso B, Shields GC, Kisiel Z, Pate BH. Broadband Fourier transform rotational spectroscopy for structure determination: The water heptamer. *Chem. Phys. Lett.* 2013, **571**, 1-5.
- 96 Acelas N, Hincapié G, Guerra D, David J, Restrepo A. Structures, energies, and bonding in the water heptamer. *J. Chem. Phys.* 2013, **139**, 044310.
- 97 Zischang J, Suhm MA. The OH stretching spectrum of warm water clusters. *J. Chem. Phys.* 2014, **140**, 064312.
- 98 Pérez C, Zaleski DP, Seifert NA, Temelso B, Shields GC, Kisiel Z, Pate BH. Hydrogen Bond Cooperativity and the Three-Dimensional Structures of Water Nonamers and Decamers. *Angew. Chem. Int. Ed.* 2014, **53**, 14368-72.

- 99 Mukhopadhyay A, Cole WT, Saykally RJ. The water dimer I: Experimental characterization. *Chem. Phys. Lett.* 2015, **633**, 13-26.
- 100 Tabor DP, Kusaka R, Walsh PS, Zwier TS, Sibert III EL. Local mode approach to OH stretch spectra of benzene-(H<sub>2</sub>O)<sub>n</sub> clusters, n= 2-7. *J. Phys. Chem. A.* 2015, **119**, 9917-30.
- 101 Nauta K, Miller RE. Formation of cyclic water hexamer in liquid helium: The smallest piece of ice. *Science.* 2000, **287**, 293-5.
- 102 Wang Y, Bowman JM. IR spectra of the water hexamer: Theory, with inclusion of the monomer bend overtone, and experiment are in agreement. *J. Phys. Chem. Lett.* 2013, **4**, 1104-8.
- 103 Kim K, Jordan KD, Zwier TS. Low-energy structures and vibrational frequencies of the water hexamer: comparison with benzene-(H<sub>2</sub>O)<sub>6</sub>. *JACS.* 1994, **116**, 11568-9.
- 104 Burnham CJ, Xantheas SS, Miller MA, Applegate BE, Miller RE. The formation of cyclic water complexes by sequential ring insertion: Experiment and theory. *J. Chem. Phys.* 2002, **117**, 1109-22.
- 105 Sulaiman MI, Yang S, Ellis AM. Infrared Spectroscopy of Methanol and Methanol/Water Clusters in Helium Nanodroplets: The OH Stretching Region. *J. Phys. Chem. A.* 2017, **121**, 771-6.
- 106 Keutsch FN, Saykally RJ. Water clusters: untangling the mysteries of the liquid, one molecule at a time. *Proc. Natl. Acad. Sci. U.S.A.* 2001, **98**, 10533-40.
- 107 Kuyanov-Prozument K, Choi MY, Vilesov AF. Spectrum and infrared intensities of OH-stretching bands of water dimers. *J. Chem. Phys.* 2010, **132**, 014304.
- 108 Sadlej J, Buch V, Kazimirski JK, Buck U. Theoretical study of structure and spectra of cage clusters (H<sub>2</sub>O)<sub>n</sub>, n= 7- 10. *J. Phys. Chem. A.* 1999, **103**, 4933-47.
- 109 Page RH, Vernon MF, Shen YR, Lee YT. Infrared vibrational predissociation spectra of large water clusters. *J. Chem. Phys. Lett.* 1987, **141**, 1-6.

- 110 Buck U. Properties of neutral clusters from scattering experiments. *J. Phys. Chem.* 1988, **92**, 1023-31.
- 111 Haberland H. Clusters of Atoms and Molecules 2-Solvation and Chemistry of Free Clusters, and Embedded, Supported and Compressed Clusters, Springer Ser. *Chem. Phys.* Berlin. 1994, **56**.
- 112 Paul JB, Collier CP, Saykally RJ, Scherer JJ, O'keefe A. Direct measurement of water cluster concentrations by infrared cavity ringdown laser absorption spectroscopy. *J. Phys. Chem. A.* 1997, **101**, 5211-4.
- 113 Buck U, Ettischer I, Melzer M, Buch V, Sadlej J. Structure and spectra of three-dimensional  $(\text{H}_2\text{O})_n$  clusters,  $n= 8, 9, 10$ . *Phys. Rev. Lett.* 1998, **80**, 2578.
- 114 Ghanty TK, Ghosh SK. Polarizability of water clusters: An ab initio investigation. *J. Chem. Phys.* 2003, **118**, 8547-50.
- 115 Fanourgakis GS, Apra E, Xantheas SS. High-level ab initio calculations for the four low-lying families of minima of  $(\text{H}_2\text{O})_{20}$ . I. Estimates of MP2/CBS binding energies and comparison with empirical potentials. *J. Chem. Phys.* 2004, **121**, 2655-63.
- 116 Su JT, Xu X, Goddard WA. Accurate energies and structures for large water clusters using the X3LYP hybrid density functional. *J. Phys. Chem. A.* 2004, **108**, 10518-26.
- 117 Steinbach C, Andersson P, Kazimirski JK, Buck U, Buch V, Beu TA. Infrared predissociation spectroscopy of large water clusters: a unique probe of cluster surfaces. *J. Phys. Chem. A.* 2004, **108**, 6165-74.
- 118 Fanourgakis GS, Aprà E, De Jong WA, Xantheas SS. High-level ab initio calculations for the four low-lying families of minima of  $(\text{H}_2\text{O})_{20}$ . II. Spectroscopic signatures of the dodecahedron, fused cubes, face-sharing pentagonal prisms, and edge-sharing pentagonal prisms hydrogen bonding networks. *J. Chem. Phys.* 2005, **122**, 134304.

- 119 Lenz A, Ojamäe L. Theoretical IR spectra for water clusters (H<sub>2</sub>O)<sub>n</sub> (n= 6– 22, 28, 30) and identification of spectral contributions from different H-bond conformations in gaseous and liquid water. *J. Phys. Chem. A*. 2006, **110**, 13388-93.
- 120 Steinbach C, Buck U. Vibrational spectroscopy of size-selected sodium-doped water clusters. *J. Phys. Chem. A*. 2006, **110**, 3128-31.
- 121 Buck U, Dauster I, Gao B, Liu ZF. Infrared spectroscopy of small sodium-doped water clusters: Interaction with the solvated electron. *J. Phys. Chem. A*. 2007, **111**, 12355-62.
- 122 Mizuse K, Hamashima T, Fujii A. Infrared spectroscopy of phenol –(H<sub>2</sub>O)<sub>n</sub> > 10: structural strains in hydrogen bond networks of neutral water clusters. *J. Phys. Chem. A*. 2009, **113**, 12134-41.
- 123 Hamashima T, Mizuse K, Fujii A. Spectral Signatures of Four-Coordinated Sites in Water Clusters: Infrared Spectroscopy of Phenol–(H<sub>2</sub>O)<sub>n</sub> (~ 20 ≤ n ≤ ~ 50). *J. Phys. Chem. A*. 2010, **115**, 620-5.
- 124 Shanker S, Bandyopadhyay P. Monte Carlo temperature basin paving with effective fragment potential: An efficient and fast method for finding low-energy structures of water clusters (H<sub>2</sub>O)<sub>20</sub> and (H<sub>2</sub>O)<sub>25</sub>. *J. Phys. Chem. A*. 2011, **115**, 11866-75.
- 125 Furtado JP, Rahalkar AP, Shanker S, Bandyopadhyay P, Gadre SR. Facilitating minima search for large water clusters at the mp2 level via molecular tailoring. *J. Phys. Chem. Lett*. 2012, **3**, 2253-8.
- 126 Liu H, Wang Y, Bowman JM. Quantum calculations of intramolecular IR spectra of ice models using ab initio potential and dipole moment surfaces. *J. Phys. Chem. Lett*. 2012, **3**, 3671-6.
- 127 Pradzynski CC, Forck RM, Zeuch T, Slaviček P, Buck U. A fully size-resolved perspective on the crystallization of water clusters. *Science*. 2012, **337**, 1529-32.

- 128 Fujii A, Mizuse K. Infrared spectroscopic studies on hydrogen-bonded water networks in gas phase clusters. *Int. Rev. Phys. Chem.* 2013, **32**, 266-307.
- 129 Saha A, Raghavachari K. Dimers of dimers (DOD): A new fragment-based method applied to large water clusters. *J. Chem. Theory Comput.* 2013, **10**, 58-67.
- 130 Liu H, Wang Y, Bowman JM. Vibrational Analysis of an Ice Ih Model from 0 to 4000  $\text{cm}^{-1}$  Using the Ab Initio WHBB Potential Energy Surface. *J. Phys. Chem. B.* 2013, **117**, 10046-52.
- 131 Sahu N, Gadre SR, Rakshit A, Bandyopadhyay P, Miliordos E, Xantheas SS. Low energy isomers of  $(\text{H}_2\text{O})_{25}$  from a hierarchical method based on Monte Carlo temperature basin paving and molecular tailoring approaches benchmarked by MP2 calculations. *J. Chem. Phys.* 2014, **141**, 164304.
- 132 Anacker T, Friedrich J. New accurate benchmark energies for large water clusters: DFT is better than expected. *J. Comput. Chem.* 2014, **35**, 634-43.
- 133 Wang K, Li W, Li S. Generalized energy-based fragmentation CCSD (T)-F12a method and application to the relative energies of water clusters  $(\text{H}_2\text{O})_{20}$ . *J. Chem. Theory Comput.* 2014, **10**, 1546-53.
- 134 Pradzynski CC, Dierking CW, Zurheide F, Forck RM, Buck U, Zeuch T, Xantheas SS. Infrared detection of  $(\text{H}_2\text{O})_{20}$  isomers of exceptional stability: a drop-like and a face-sharing pentagonal prism cluster. *J. Phys. Chem. Chem. Phys.* 2014, **16**, 26691-6.
- 135 Buck U, Pradzynski CC, Zeuch T, Dieterich JM, Hartke B. A size resolved investigation of large water clusters. *J. Phys. Chem. Chem. Phys.* 2014, **16**, 6859-71.
- 136 Zurheide F, Dierking CW, Pradzynski CC, Forck RM, Flüggen F, Buck U, Zeuch T. Size-Resolved Infrared Spectroscopic Study of Structural Transitions in Sodium-Doped  $(\text{H}_2\text{O})_n$  Clusters Containing 10–100 Water Molecules. *J. Phys. Chem. A.* 2014, **119**, 2709-20.
- 137 Fournier JA, Wolke CT, Johnson MA, Odbadrakh TT, Jordan KD, Kathmann SM, Xantheas SS. Snapshots of proton accommodation at a microscopic water surface:

Understanding the vibrational spectral signatures of the charge defect in cryogenically cooled  $\text{H}^+$  ( $\text{H}_2\text{O}$ )<sub>n</sub> n= 2–28 clusters. *J. Phys. Chem. A*. 2015, **119**, 9425-40.

138 Sahu N, Khire SS, Gadre SR. Structures, energetics and vibrational spectra of ( $\text{H}_2\text{O}$ )<sub>32</sub> clusters: a journey from model potentials to correlated theory. *Mol. Phys.* 2015, **113**, 2970-9.

139 Sahu N, Gadre SR. Accurate vibrational spectra via molecular tailoring approach: A case study of water clusters at MP2 level. *J. Chem. Phys.* 2015, **142**, 14107.

140 Bowman JM, Wang Y, Liu H, Mancini JS. Ab Initio Quantum Approaches to the IR Spectroscopy of Water and Hydrates. *Phys. Rev. Lett.* 2015, **6**, 366-73.

141 Pribble RN, Zwier TS. Size-Specific Infrared Spe. *Science*. 1994, **265**, 75.

142 Jiang JC, Chang JC, Wang BC, Lin SH, Lee YT, Chang HC. The free-OH stretching frequencies of 3-coordinated H<sub>2</sub>O in water clusters and on ice surfaces. *Chem. Phys. Lett.* 1998, **289**, 373-82

143 Buch V, Sigurd B, Paul Devlin J, Buck U, Kazimirski JK. Solid water clusters in the size range of tens–thousands of H<sub>2</sub>O: a combined computational/spectroscopic outlook. *Int. Rev. Phys. Chem.* 2004, **23**, 375-433.

144 Buch V, Devlin JP. Spectra of dangling OH bonds in amorphous ice: Assignment to 2-and 3-coordinated surface molecules. *J. Chem. Phys.* 1991, **94**, 4091-2.

145 Bergren MS, Schuh D, Sceats MG, Rice SA. The OH stretching region infrared spectra of low density amorphous solid water and polycrystalline ice Ih. *J. Chem. Phys.* 1978, **69**, 3477-82.

146 Walrafen GE. Raman spectral studies of the effects of temperature on water structure. *J. Chem. Phys.* 1967, **47**, 114-26.

147 Wieliczka DM, Weng S, Querry MR. Wedge shaped cell for highly absorbent liquids: infrared optical constants of water. *Appl. Opt.* 1989, **28**, 1714-9.

- 148 Zasetsky AY, Khalizov AF, Earle ME, Sloan JJ. Frequency dependent complex refractive indices of supercooled liquid water and ice determined from aerosol extinction spectra. *J. Phys. Chem. A*. 2005, **109**, 2760-4.
- 149 Zasetsky AY, Khalizov AF, Sloan JJ. Local order and dynamics in supercooled water: A study by IR spectroscopy and molecular dynamic simulations. *J. Chem. Phys.* 2004, **121**, 6941-7.
- 150 Senesi R, Flammini D, Kolesnikov AI, Murray ÉD, Galli G, Andreani C. The quantum nature of the OH stretching mode in ice and water probed by neutron scattering experiments. *J. Chem. Phys.* 2013, **139**, 074504.
- 151 Huisken F, Stemmler M. Infrared photodissociation of small methanol clusters. *Chem. Phys. Lett.* 1988, **144**, 391-5.
- 152 Buck U, Gu X, Lauenstein C, Rudolph A. A. Infrared photodissociation spectra of size-selected  $(\text{CH}_3\text{OH})_n$  clusters from  $n = 2$  to  $n = 8$ . *J. Phys. Chem.* 1988, **92**, 5561–5562.
- 153 Mó O, Yánez M, Elguero J. Cooperative effects in the cyclic trimer of methanol. An ab initio molecular orbital study. *THEOCHEM*. 1994, **314**, 73-81.
- 154 Xantheas SS. Ab initio studies of cyclic water clusters  $(\text{H}_2\text{O})_n$ ,  $n = 1-6$ . III. Comparison of density functional with MP2 results. *J. Chem. Phys.* 1995, **102**, 4505-17.
- 155 Huisken F, Kaloudis M, Koch M, Werhahn O. Experimental study of the O-H ring vibrations of the methanol trimer. *J. Chem. Phys.* 1996, **105**, 8965–8968.
- 156 Buck U, Ettischer I. Vibrational predissociation spectra of size selected methanol clusters: new experimental results. *J. Chem. Phys.* 1998, **108**, 33–38.
- 157 Provencal RA, Paul JB, Roth K, Chapo C, Casaes RN, Saykally RJ, Tschumper GS, Schaefer HF. III Infrared cavity ringdown spectroscopy of methanol clusters: single donor hydrogen bonding. *J. Chem. Phys.* 1999, **110**, 4258–4267.
- 158 Häber T, Schmitt U, Suhm MA, FTIR-spectroscopy of molecular clusters in pulsed supersonic slit-jet expansions. *Phys. Chem. Chem. Phys.* 1999, **1**, 5573–5582.

- 159 Buck U, Huisken F. Infrared spectroscopy of size-selected water and methanol clusters. *Chem. Rev.* 2000, **100**, 3863–3890.
- 160 Steinbach C, Fárnik M, Ettischer I, Siebers J, Buck U, Isomeric transitions *in size-selected methanol hexamers probed by OH-stretch spectroscopy.* *Phys. Chem. Chem. Phys.* 2006, **8**, 2752– 2758.
- 161 Fu HB, Hu YJ, Bernstein ER. IR + vacuum ultraviolet (118 nm) nonresonant ionization spectroscopy of methanol monomers and clusters: neutral cluster distribution and size-specific detection of the OH stretch vibrations. *J. Chem. Phys.* 2006, **124**, 024302.
- 162 Hu YJ, Fu HB, Bernstein ER. Infrared plus vacuum ultraviolet spectroscopy of neutral and ionic methanol monomers and clusters: New experimental results. *J. Chem. Phys.* 2006, **125**, 154306.
- 163 Larsen RW, Zielke P, Suhm MA. Hydrogen-bonded OH stretching modes of methanol clusters: a combined IR and Raman isotopomer study. *J. Chem. Phys.* 2007, **126**, 194307.
- 164 Han HL, Camacho C, Witek HA, Lee YP. Infrared absorption of methanol clusters (CH<sub>3</sub>OH)<sub>n</sub> with *n* = 2–6 recorded with a time-of-flight mass spectrometer using infrared depletion and vacuum-ultraviolet ionization. *J. Chem. Phys.* 2011, **134**, 144309.
- 165 Coussan S, Loutellier A, Perchard JP, Racine S, Peremans A, Tadjeddine A, Zheng WQ. Infrared laser induced isomerization of methanol polymers trapped in nitrogen matrix. I. Trimers. *J. Chem. Phys.* 1997, **107**, 6526–6540.
- 166 Coussan S, Bouteiller Y, Loutellier A, Perchard JP, Racine S, Peremans A, Zheng WQ, Tadjeddine A. Infrared photoisomerization of the methanol dimer trapped in argon matrix; monochromatic irradiation experiments and DFT calculations. *Chem. Phys.* 1997, **219**, 221–234.

- 167 Coussan S, Loutellier A, Perchard JP, Racine S, Peremans A, Tadjeddine A, Zheng WQ, IR-induced interconversions between five conformers of methanol dimer trapped in nitrogen matrix. *Chem. Phys.* 1997, **223**, 279–292.
- 168 Perchard JP, Mielke Z. Anharmonicity and hydrogen bonding I. A near-infrared study of methanol trapped in nitrogen and argon matrices. *Chem. Phys.* 2001, **264**, 221–234.
- 169 Hagemester FC, Gruenloh CJ, Zwier TS. Density functional theory Calculations of the structures, binding energies, and infrared spectra of methanol clusters. *J. Phys. Chem. A.* 1998, **102**, 82– 94.
- 170 David J, Guerra D, Restrepo A. Structural characterization of the (methanol)<sub>4</sub> potential energy surface. *J. Phys. Chem. A*, 2009, **113**, 10167–10173.
- 171 Nishimura Y, Lee YP, Irle S, Witek HA. Critical interpretation of CH– and OH– stretching regions for infrared spectra of methanol clusters (CH<sub>3</sub>OH)<sub>n</sub> (*n* = 2–5) using selfconsistent- charge density functional tight-binding molecular dynamics simulations. *J. Chem. Phys.* 2014, **141**, 094303.
- 172 Kazachenko S, Bulusu S, Thakkar AJ. Methanol clusters (CH<sub>3</sub>OH)<sub>n</sub>: putative global minimum-energy structures from model potentials and dispersion-corrected density functional theory. *J. Chem. Phys.* 2013, **138**, 224303.
- 173 Behrens M, Fröchtenicht R, Hartmann M, Siebers JG, Buck U, Hagemester FC. Vibrational spectroscopy of methanol and acetonitrile clusters in cold helium droplets. *J. Chem. Phys.* 1999, **111**, 2436–2443.
- 174 Bates DM, Tschumper GS. CCSD(T) Complete basis set limit relative energies for low-lying water hexamer structures. *J. Phys. Chem. A.* 2009, **113**, 3555–3559.
- 175 Temelso B, Archer KA, Shields GC. Benchmark structures and binding energies of small water clusters with anharmonicity corrections. *J. Phys. Chem. A*, 2011, **115**, 12034–12046.

- 176 Callegari C, Ernst WE. Helium Droplets as Nanocryostats for Molecular Spectroscopy from the Vacuum Ultraviolet to the Microwave Regime. *In Handbook of High-resolution Spectroscopy*, Wiley, 2011
- 177 Frisch MJ, Trucks GW, Schlegel HB, Scuseria GE, Robb MA, Cheeseman JR, Scalmani G, Barone V, Mennucci B, Petersson GA. Gaussian 09, Revision E.01; Gaussian, Inc. Wallingford, CT. 2009.
- 178 Fileti EE, Canuto S. Calculated infrared spectra of hydrogen bonded methanol-water, water-methanol, and methanol-methanol complexes. *Int. J. Quantum Chem.* 2005, **104**, 808–815.
- 179 Huisken F, Stemmler M. On the structure of the methanol–water dimer. *Chem. Phys. Lett.* 1991, **180**, 332–338.
- 180 Bakkas N, Bouteiller Y, Loutellier A, Perchard JP, Racine S. The water–methanol complexes. I. A matrix isolation study and an ab initio calculation on the 1-1 species. *Chem. Phys.* 1993, **99**, 3335–42.
- 181 Bakkas N, Bouteiller Y, Loutellier A, Perchard JP, Racine S. The water-methanol complexes. Matrix induced structural conversion of the 1-1 species. *Chem. Phys. Lett.* 1995, **232**, 90–8.
- 182 González L, Mó O, Yáñez M. High level ab initio and density functional theory studies on methanol–water dimers and cyclic methanol (water)<sub>2</sub> trimer. *J. Chem. Phys.* 1998, **109**, 139–150.
- 183 Rablen PR, Lockman JW, Jorgensen WL. Ab Initio Study of Hydrogen-Bonded Complexes of Small Organic Molecules with Water. *J. Phys. Chem. A.* 1998, **102**, 3782.
- 184 Iosue JL, Benoit DM, Clary DC. Diffusion Monte Carlo simulations of methanol-water clusters. *Chem. Phys. Lett.* 1999, **301**, 275–280.
- 185 Tvan Erp TS, Meijer EJ. Hydration of methanol in water. A DFT-based molecular dynamics study. *Chem. Phys. Lett.* 2001, **333**, 290.

- 186 Moskowitz JW, Bačić Z, Sarsa A, Schmidt KE. Relative stabilities of the two isomers of the methanol-water dimer: The effects of the internal rotations of the hydroxyl and methyl groups of methanol. *J. Chem. Phys.* 2001, **114**, 10294–10299.
- 187 Yamamoto N, Nishino Y, Miyoshi E. Classical trajectory calculations of intramolecular vibrational energy redistribution. I. Methanol-water complex. *J. Chem. Phys.* 2004, **121**, 2058–2066.
- 188 Mejía SM, Espinal JF, Mondragón F. Cooperative effects on the structure and stability of (ethanol)<sub>3</sub>-water, (methanol)<sub>3</sub>-water heterotetramers and (ethanol)<sub>4</sub>, (methanol)<sub>4</sub> tetramers. *J. Mol. Struct. (THEOCHEM)*. 2009, **901**, 186-93.
- 189 Mandal A, Prakash M, Kumar RM, Parthasarathi R, Subramanian V. Ab initio and DFT studies on methanol-water clusters. *J. Phys. Chem. A*. 2010, **114**, 2250–2258.
- 190 Nedić M, Wassermann TN, Larsen RW, Suhm MA. A combined Raman and infrared jet study of mixed methanol-water and ethanol-water clusters. *Phys. Chem. Chem. Phys.* 2011, **13**, 14050–14063
- 191 Mejía SM, Flórez E, Mondragón F. Mondragon F. An orbital and electron density analysis of weak interactions in ethanol-water, methanol-water, ethanol and methanol small clusters. *J. Chem. Phys.* 2012, **136**, 144306.
- 192 Hernandez FJ, Brice JT, Leavitt CM, Pino GA, Douberly GE. Infrared spectroscopy of OH···CH<sub>3</sub>OH: Hydrogen bonded intermediate along the hydrogen abstraction reaction path. *J. Phys. Chem. A*. 2015, **119**, 8125–8132.
- 193 Mejía SM, Espinal JF, Mills MJ, Mondragón F. The role of OH···O and CH···O hydrogen bonds and H···H interactions in ethanol/ methanol–water heterohexamers. *J. Mol. Model.* 2016, **22**, 181–190.
- 194 Czakó G, Bowman JM. Dynamics of the reaction of methane with chlorine atom on an accurate potential energy surface. *Science*. 2011, **334**, 343-6.
- 195 Murray C, Orr-Ewing AJ. The dynamics of chlorine-atom reactions with polyatomic organic molecules. *Int. Rev. Phys. Chem.* 2004, **23**, 435-82.

- 196 Atkinson R, Baulch DL, Cox RA, Crowley JN, Hampson RF, Hynes RG, Jenkin ME, Rossi MJ, Troe J, Subcommittee IUPAC. Evaluated kinetic and photochemical data for atmospheric chemistry: Volume II—gas phase reactions of organic species. *Atmospheric Chem. Phys.* 2006, **6**, 3625-4055.
- 197 George C, Behnke W, Zetzsch C. Radicals in the atmosphere: a changing world!. *ChemPhysChem.* 2010, **11**, 3059-62.
- 198 Küpper J, Merritt JM, Miller RE. Free radicals in superfluid liquid helium nanodroplets: A pyrolysis source for the production of propargyl radical. *J. Chem. Phys.* 2002, **117**, 647-52.
- 199 Kohn DW, Clauberg H, Chen P. Flash pyrolysis nozzle for generation of radicals in a supersonic jet expansion. *Rev. Sci. Instrum.* 1992, **63**, 4003-5.
- 200 Zhang X, Friderichsen AV, Nandi S, Ellison GB, David DE, McKinnon JT, Lindeman TG, Dayton DC, Nimlos MR. Intense, hyperthermal source of organic radicals for matrix-isolation spectroscopy. *Rev. Sci. Instrum.* 2003, **74**, 3077-86.
- 201 Cameron MR, Kable SH. A new design for a simple and effective pyrolysis nozzle in a supersonic free jet. *Rev. Sci. Instrum.* 1996, **67**, 283-7.
- 202 Frisch M, Trucks GW, Schlegel H, Scuseria GE, Robb MA, Cheeseman JR, Montgomery Jr JA, Vreven TK, Kudin KN, Burant JC, Millam JM. Gaussian 03, revision C. 02; Gaussian, Inc. Wallingford, CT. 2004, **26**.
- 203 Ferreira da Silva F, Waldburger P, Jaksch S, Mauracher A, Denifl S, Echt O, Märk TD, Scheier P. On the size of ions solvated in helium clusters. *Chem. Eur. J.* 2009, **15**, 7101-8.
- 204 Frank HS, Evans MW. Free volume and entropy in condensed systems III. Entropy in binary liquid mixtures; partial molal entropy in dilute solutions; structure and thermodynamics in aqueous electrolytes. *Chem. Phys.* 1945, **13**, 507-32.